

---

Electronic Thesis and Dissertation Repository

---

12-10-2014 12:00 AM

# On the Application of Mechanical Vibration in Robotics-Assisted Soft Tissue Intervention

Iman Khalaji

*The University of Western Ontario*

Supervisor

Dr Rajni V. Patel

*The University of Western Ontario* Joint Supervisor

Dr Michael D. Naish

*The University of Western Ontario*

Graduate Program in Mechanical and Materials Engineering

A thesis submitted in partial fulfillment of the requirements for the degree in Doctor of Philosophy

© Iman Khalaji 2014

Follow this and additional works at: <https://ir.lib.uwo.ca/etd>



Part of the [Biomechanical Engineering Commons](#), [Biomedical Devices and Instrumentation Commons](#), and the [Electro-Mechanical Systems Commons](#)

---

## Recommended Citation

Khalaji, Iman, "On the Application of Mechanical Vibration in Robotics-Assisted Soft Tissue Intervention" (2014). *Electronic Thesis and Dissertation Repository*. 2558.

<https://ir.lib.uwo.ca/etd/2558>

This Dissertation/Thesis is brought to you for free and open access by Scholarship@Western. It has been accepted for inclusion in Electronic Thesis and Dissertation Repository by an authorized administrator of Scholarship@Western. For more information, please contact [wlsadmin@uwo.ca](mailto:wlsadmin@uwo.ca).

# On the Application of Mechanical Vibration in Robotics-Assisted Soft Tissue Intervention

(Thesis format: Integrated-Article)

by

Iman Khalaji

Graduate Program in Engineering Science  
Department of Mechanical and Materials Engineering

A thesis submitted in partial fulfillment  
of the requirements for the degree of  
Doctor of Philosophy

The School of Graduate and Postdoctoral Studies  
The University of Western Ontario  
London, Ontario, Canada

© Iman Khalaji 2014

# Abstract

Mechanical vibration as a way of transmitting energy has been an interesting subject to study. While cyclic oscillation is usually associated with fatigue effect, and hence a detrimental factor in failure of structures and machineries, by controlled transmission of vibration, energy can be transferred from the source to the target. In this thesis, the application of such mechanical vibration in a few surgical procedures is demonstrated.

Three challenges associated with lung cancer diagnosis and treatment are chosen for this purpose, namely, ***Motion Compensation***, tumor targeting in lung ***Needle Insertion*** and ***Soft Tissue Dissection***:

1. A robotic solution is proposed for compensating for the undesirable oscillatory motion of soft tissue (caused by heart beat and respiration) during needle insertion in the lung. An impedance control strategy based on a mechanical vibratory system is implemented to minimize the tissue deformation during needle insertion. A prototype was built to evaluate the proposed approach using: 1) two Mitsubishi PA10-7C robots, one for manipulating the macro part and the other for mimicking the tissue motion, 2) one motorized linear stage to handle the micro part, and 3) a Phantom Omni haptic device for remote manipulation. Experimental results are given to demonstrate the performance of the motion compensation system.
2. A vibration-assisted needle insertion technique has been proposed in order to reduce needle–tissue friction. The LuGre friction model is employed as a basis for the study and the model is extended and analyzed to include the impact of high-frequency vibration on translational friction. Experiments are conducted to evaluate the role of insertion speed as well as vibration frequency on frictional effects. In the experiments conducted, an 18 GA brachytherapy needle was vibrated and inserted into an *ex-vivo* soft tissue sample using a pair of amplified piezoelectric actuators. Analysis demonstrates that the translational friction can be reduced by introducing a vibratory low-amplitude motion onto a regular insertion profile, which is usually performed at a constant rate.

3. A robotics-assisted articulating ultrasonic surgical scalpel for minimally invasive soft tissue cutting and coagulation is designed and developed. For this purpose, the optimal design of a Langevin transducer with stepped horn profile is presented for internal-body applications. The modeling, optimization and design of the ultrasonic scalpel are performed through equivalent circuit theory and verified by finite element analysis. Moreover, a novel surgical wrist, compatible with the da Vinci<sup>®</sup> surgical system, with decoupled two degrees-of-freedom (DOFs) is developed that eliminates the strain of pulling cables and electrical wires. The developed instrument is then driven using the dVRK (da Vinci<sup>®</sup> research kit) and the Classic da Vinci<sup>®</sup> surgical system.

**Keywords:** Lung cancer, Mechanical vibration, Robotics-assisted minimally invasive surgery, Motion compensation, Impedance control, Needle insertion, Ultrasonically activated scalpel, Non-uniform Rational B-spline (NURBS), Optimization, Finite element analysis



## Statement of Co-Authorship

The thesis presented herein has been written by Iman Khalaji under the supervision of Dr. Rajni V. Patel and Dr. Michael D. Naish. Some of the content of this thesis has been published in refereed conference proceedings, or is under review for publication.

A version of the material presented in Chapter 2 has been published in

- S. Farokh Atashzar, Iman Khalaji, Mahya Shahbazi, Ali Talasaz, Rajni V. Patel, and Michael D. Naish, “Robot-assisted lung motion compensation during needle insertion,” in *Proceedings of IEEE International Conference on Robotics and Automation (ICRA)*, 2013, pp. 1682–1687.
  - S.F. Atashzar, I. Khalaji and M. Shahbazi - contributed equally in developing the experimental setup, designing the controller, conducting the experiments, analyzing the results, and writing the manuscript.
  - Dr. A. Talasaz - originally developed the dual arm master-slave teleoperation testbed, consisting of two Mitsubishi PA10-7C robots as the slave system that is remotely controlled through two 7-DOF Haptic Wands, and reviewed the manuscript.

A version of the material presented in Chapter 3 has been published in

- Iman Khalaji, Mostafa Hadavand, Ali Asadian, Rajni V. Patel, and Michael D. Naish, “Analysis of needle-tissue friction during vibration-assisted needle insertion,” in *Proceedings of IEEE/RSJ International Conference on Intelligent Robots and Systems (IROS)*, 2013, pp. 4099–4104.
  - I. Khalaji - proposed the approach, developed the mathematical model, designed and implemented the electro-mechanical part of the experimental setup, conducted the experiments and analyzed the results, wrote the manuscript.
  - M. Hadavand - designed the CAD models of the initial experimental setup (including voice-coil actuator holder, soft tissue holder, force sensor holder), contributed in conducting the experiments, and in generating figures for the manuscript.
  - Dr. A. Asadian - reviewed the manuscript, and contributed in analyzing the results.

Part of the materials presented in Chapters 4 and 6 is currently under peer review in

- Iman Khalaji, Michael D. Naish and Rajni V. Patel, “Articulating Minimally Invasive Ultrasonic Tool for Robotics-Assisted Surgery,” submitted to *IEEE International Conference on Robotics and Automation (ICRA)*, 2015.

A version of the material presented in Chapter 5 has been published in

- Iman Khalaji, Rajni V. Patel, and Michael D. Naish, “Systematic design of an ultrasonic horn profile for high displacement amplification,” in *Proceedings of 4th IEEE RAS & EMBS International Conference on Biomedical Robotics and Biomechatronics (BioRob)*, 2012, pp. 913–918.

*To those who never give up their hopes and dreams,  
in spite of tremendous hardships.*

# Acknowledgements

Apart from my own efforts, the successful completion of this dissertation was a result of the contribution, encouragement and guidance of many others. I would like to express my profound gratitude to all those who helped me during my Ph.D. studies.

Above all, I would like to express my sincere appreciation and gratitude to my advisors, Professor Rajni Patel and Professor Michael Naish. Prof. Patel: you have been a tremendous mentor for me. I would like to thank you for encouraging my research and for allowing me to grow as a research engineer. Your advice on both research as well as on my career has been priceless. Prof. Naish: I am very grateful for your consistent support and encouragement. You taught me how to be meticulous and diligent about even minute details of the work.

I would also like to thank my advisory committee members, Dr. Shaun Salisbury and Dr. Sam Asokanthan. Also special thanks to Dr. George Knopf, Dr. Ken McIsaac and Dr. Ridha Ben-Mrad for serving on my thesis examining committee.

I would especially like to thank my friends and colleagues at CSTAR, Dr. Ali Talsaz, Dr. Mahta Khoshnam, Dr. Ali Asadian, Mostafa Hadavand, Farokh Atashzar and Mahya Shahbazi for helping me during my Ph.D. studies. The help of Chris Ward and Abelardo Escoto is also greatly appreciated.

I cannot thank enough my family for their moral support. Mom and dad: I truly appreciate your help during these past years.

Last, but by no means the least, I would like to thank my beautiful wife. Nazanin: without your love, sacrifice and support I would never have been able to accomplish this.

# Table of Contents

<b>Abstract</b>	<b>ii</b>
<b>Statement of Co-Authorship</b>	<b>iv</b>
<b>Dedication</b>	<b>vi</b>
<b>Acknowledgements</b>	<b>vii</b>
<b>Table of Contents</b>	<b>viii</b>
<b>List of Tables</b>	<b>xi</b>
<b>List of Figures</b>	<b>xii</b>
<b>Nomenclature</b>	<b>xiv</b>
<b>1 Introduction</b>	<b>1</b>
1.1 Synopsis	1
1.1.1 Lung Cancer Diagnosis	1
1.1.2 Lung Cancer Treatment	2
1.1.3 Minimally Invasive Image-Guided Tumor Resection	6
1.2 Lung Cancer: From Diagnosis to Treatment	7
1.2.1 Motion Compensation	7
1.2.2 Tumor Targeting in Lung Needle Biopsy and Brachytherapy	7
1.2.3 MIS Sublobar Dissection Instrument	8
1.3 Thesis Outline and Organization	9
<b>2 Motion Compensation for Needle Insertion</b>	<b>16</b>
2.1 Introduction	16
2.2 Method	18
2.2.1 Mechanical Model	19
2.2.2 Impedance Control Design	22
2.3 Prototype Design	25
2.4 Experimental Results	27
2.4.1 Experiment I	27
2.4.2 Experiment II	27
2.5 Conclusions and Future Work	33

<b>3</b>	<b>Vibration-Assisted Needle Insertion . . . . .</b>	<b>38</b>
3.1	Introduction . . . . .	38
3.2	Related Work . . . . .	39
3.3	Mathematical Analysis of Needle–Tissue Friction Using Vibration . .	40
3.3.1	Needle Insertion at Constant Velocity . . . . .	42
3.3.2	Vibration-Assisted Needle Insertion . . . . .	43
3.4	Instrumentation and Experimental Evaluation . . . . .	48
3.4.1	Experimental Setup . . . . .	48
3.4.2	Experiment Design . . . . .	49
3.4.3	Experimental Results . . . . .	51
3.5	Conclusions and Future Work . . . . .	54
<b>4</b>	<b>Systematic Optimal Design of a Langevin Piezoelectric Actuator</b>	<b>57</b>
4.1	Introduction . . . . .	57
4.2	Structure of a Langevin Piezoelectric Transducer . . . . .	59
4.3	Equivalent Circuit Network Modelling . . . . .	60
4.4	Optimization of the Langevin Piezoelectric Transducer . . . . .	68
4.4.1	Problem statement . . . . .	69
4.5	Finite Element Analysis . . . . .	73
4.6	Results and Discussion . . . . .	74
4.6.1	Pareto front . . . . .	74
4.6.2	Case study . . . . .	75
4.7	Conclusions . . . . .	81
<b>5</b>	<b>Systematic Optimal Design of an Ultrasonic Horn Profile . . . . .</b>	<b>87</b>
5.1	Introduction . . . . .	87
5.2	Introduction to NURBS . . . . .	89
5.3	Horn Design . . . . .	90
5.3.1	Longitudinal Wave Propagation . . . . .	90
5.3.2	NURBS-based Horn Profile . . . . .	92
5.3.3	Longitudinal Wave Equation Revisited . . . . .	93
5.3.4	Solving the Normalized Wave Equation . . . . .	94
5.3.5	Optimization Scheme . . . . .	95
5.4	Analyses . . . . .	98
5.4.1	Optimization Results . . . . .	98
5.4.2	Finite Element Verification . . . . .	101
5.5	Conclusions . . . . .	104
<b>6</b>	<b>Articulating Minimally Invasive Ultrasonic Tool for Robotics-Assisted Surgery . . . . .</b>	<b>107</b>
6.1	Introduction . . . . .	107
6.2	Related Work . . . . .	108
6.2.1	Ultrasonically Activated Scalpel . . . . .	108

6.2.2	Articulating Robotics-Assisted Surgical Tool . . . . .	109
6.3	Materials and Methods . . . . .	109
6.3.1	Ultrasonically Activated Scalpel . . . . .	109
6.3.2	Articulating Robotics-Assisted Surgical Tool . . . . .	116
6.4	Results and Discussion . . . . .	117
6.4.1	Ultrasonic Scalpel . . . . .	117
6.4.2	Articulating Ultrasonic Scalpel . . . . .	122
6.5	Conclusions and Future Work . . . . .	124
<b>7</b>	<b>Concluding Remarks and Future Work . . . . .</b>	<b>136</b>
7.1	Remarks . . . . .	136
7.1.1	Motion Compensation . . . . .	136
7.1.2	Vibration-Assisted Needle Insertion . . . . .	137
7.1.3	Ultrasonically Activated Scalpel for Internal Body Applications	138
7.2	Future Research . . . . .	139
7.2.1	Motion Compensation . . . . .	139
7.2.2	Vibration-Assisted Needle Insertion . . . . .	140
7.2.3	Ultrasonically Activated Scalpel for Internal Body Applications	142
<b>A</b>	. . . . .	<b>146</b>
<b>B</b>	. . . . .	<b>148</b>
	<b>Curriculum Vitae . . . . .</b>	<b>153</b>

# List of Tables

1.1	Comparison of lung preserving surgery techniques [3] . . . . .	4
1.2	Comparison of lung preserving surgery techniques [3] (continued) . .	5
4.1	Material properties of the various sections of the piezoelectric actuator	76
4.2	Primary and secondary design parameter constraints . . . . .	77
4.3	Mode shapes and their associated frequencies by finite element and equivalent circuit methods . . . . .	80
5.1	Comparison of the amplification factor, $M$ , and resonance frequency, $f$ , of various spline-based horn profiles, obtained from the proposed approach and finite element method . . . . .	102
6.1	Material properties of the various sections of the piezoelectric actuator.	119
6.2	Design parameter constraints. . . . .	121
6.3	Mode shapes and their associated frequencies by finite element and equivalent circuit methods. . . . .	122
6.4	DH parameters of the new developed tool. . . . .	123
6.5	Coupling matrix of the new developed tool. . . . .	123



# List of Figures

2.1	General view of the Macro–Micro architecture . . . . .	19
2.2	The overall system architecture . . . . .	20
2.3	2 DOF vibratory system . . . . .	21
2.4	Schematic dual electrical circuit of the 2-DOF vibratory system . . .	23
2.5	Experimental setup and corresponding CAD models . . . . .	26
2.6	Motion compensation for axial movement . . . . .	28
2.7	Motion compensation for various orientations . . . . .	28
2.8	Comparison of the output of the identified system with the measured tissue deformation . . . . .	29
2.9	Bode plot of the identified soft tissue . . . . .	30
2.10	Bode plot of the designed a(s) . . . . .	30
2.11	The performance of the local impedance controller . . . . .	31
2.12	The system performance in terms of tracking and applied force . . . .	32
2.13	Comparison between the experimental and the theoretical performance measures . . . . .	34
3.1	Microscopic representation of irregular contact surfaces and elastic bristles. . . . .	41
3.2	Schematic demonstration of the proposed needle insertion setup. . . .	43
3.3	Mathematical dependency of the normalized Coulomb friction force on the velocity ratio during vibration-assisted needle insertion. . . . .	48
3.4	Vibration-assisted needle insertion setup. . . . .	50
3.5	Measured force values during needle insertion at various frequencies (insertion velocity = 5 mm/sec, vibration amplitude = 0.030 mm p–p). .	52
3.6	Measured force values during needle insertion at various frequencies (insertion velocity = 5 mm/sec, vibration amplitude = 0.030 mm p–p). .	52
3.7	Measured force values during needle insertion at various frequencies (insertion velocity = 10 mm/sec, vibration amplitude = 0.030 mm p–p). .	53
3.8	Measured force values during needle insertion at various frequencies (insertion velocity = 10 mm/sec, vibration amplitude = 0.030 mm p–p). .	53
3.9	Force magnitude versus velocity ratio of the vibrating needle. . . . .	54
4.1	Langevin piezoelectric transducer . . . . .	61
4.2	Schematic of a piezoelectric transducer and its corresponding equiva- lent circuit . . . . .	62

4.3	Pareto optimal solution in the objective space . . . . .	78
4.4	Performance measures of the optimal designed actuator . . . . .	79
4.5	Performance criteria of the optimal designed actuator . . . . .	81
4.6	FE analysis of the optimal design actuator . . . . .	82
5.1	A normalized NURBS-based horn profile in the design space. . . . .	97
5.2	An optimized rational Bezier horn profile along with displacement distribution, strain and $X$ and $R$ curves. . . . .	100
5.3	Comparison of the optimal curves obtained using the proposed method. 103	
6.1	Schematic illustration of a Langevin transducer. . . . .	110
6.2	Equivalent circuit of a Langevin piezoelectric transducer. . . . .	111
6.3	CAD model of the 1-DOF articulating wrist. . . . .	117
6.4	CAD model of the ultrasonic scalpel, its sheath cover and the gripping jaw. . . . .	125
6.5	Pareto front curve obtained through Genetic algorithm, overlayed on around 300,000 solutions which are obtained by exhaustive search at the objective space. . . . .	126
6.6	Performance measures of the designed optimal actuator obtained by equivalent circuit. . . . .	127
6.7	Performance criteria of the optimal designed actuator obtained by FEA. 127	
6.8	FE analysis of the optimally designed actuator . . . . .	128
6.9	Measured impedance of the ultrasonic scalpel. . . . .	129
6.10	The developed articulating ultrasonic scalpel. . . . .	129
6.11	Kinematics of the developed instrument. . . . .	130
6.12	Workspace of the developed wrist. . . . .	131
6.13	Disk numbering of a da Vinci <sup>®</sup> tool. . . . .	132
7.1	Prototypes of TakkTile sensors made as single units (bare sensors), or in an array unit (filled with rubber). . . . .	141
7.2	Piezoelectric actuator unit with micron-sensitive vibration sensor. . .	142

# Nomenclature

<b>2-D</b>	<i>Two Dimensional</i>
<b>3-D</b>	<i>Three Dimensional</i>
<b>AJCC</b>	<i>American Joint Committee on Cancer</i>
<b>CAD</b>	<i>Computer Aided Design</i>
<b>CT</b>	<i>Computed Tomography</i>
<b>DOF</b>	<i>Degrees of Freedom</i>
<b>dVRK</b>	<i>da Vinci<sup>®</sup> Research Kit</i>
<b>ECG</b>	<i>Electrocardiogram</i>
<b>FEM</b>	<i>Finite Element Analysis</i>
<b>FRF</b>	<i>Frequency Response Function</i>
<b>HD</b>	<i>High Dose</i>
<b>KCL</b>	<i>Kirchhoff's Current Law</i>
<b>KVL</b>	<i>Kirchhoff's Voltage Law</i>
<b>LD</b>	<i>Low Dose</i>
<b>MIS</b>	<i>Minimally Invasive Surgery</i>
<b>MRI</b>	<i>Magnetic Resonance Imaging</i>
<b>NSCLC</b>	<i>Non-Small Cell Lung Cancer</i>
<b>NSGA</b>	<i>Non-dominated Sorting Genetic Algorithm</i>
<b>NURBS</b>	<i>Non-Uniform Rational B-Splines</i>
<b>ODE</b>	<i>Ordinary Differential Equation</i>
<b>PET</b>	<i>Positron Emission Tomography</i>
<b>RAMIS</b>	<i>Robotics-Assisted Minimally Invasive Surgery</i>
<b>RCM</b>	<i>Remote Centre of Motion</i>
<b>SCLC</b>	<i>Small Cell Lung Cancer</i>
<b>SQP</b>	<i>Sequential Quadratic Programming</i>
<b>UICC</b>	<i>Union for International Cancer Control</i>

*Nomenclature*

---

**US**

*Ultrasound*

**VATS**

*Video-Assisted Thoracoscopic Surgery*

# Chapter 1

## Introduction

### 1.1 Synopsis

Lung cancer is the leading cause of cancer deaths in both men and women worldwide. About 1.59 million deaths occur annually around the world, as of 2012 [1]. Small cell lung cancer (SCLC) and non-small cell lung cancer (NSCLC) are the primary cancer types, with NSCLC accounting for about 80% of all lung carcinomas. Treatment options are determined by the type of cancer cell, the stage (degree of spread), and overall health performance of the patient, and include surgery, radiation therapy, chemotherapy and targeted therapies [2]. As a rule of thumb, NSCLC is often treated with surgery, whereas SCLC usually responds better to chemotherapy and radiotherapy. For localized cancers, however, surgery followed by chemotherapy and/or radiation therapy is usually the treatment of choice.

#### 1.1.1 Lung Cancer Diagnosis

Imaging tests, such as 2-D X-ray followed by 3-D Computed Tomography (CT) scan for better visualization, are common procedures for detecting suspicious nodules within lung tissue and nearby organs. Depending on the location of the suspicious area, tissue samples (biopsy) will then be taken through bronchoscopy, mediastinoscopy or percutaneous needle biopsy. The samples are examined histologically to confirm cancerous cells and to rule out other conditions.

Once diagnosed, the extent of the cancer has to be determined to identify treatment options. This may include additional imaging tests such as CT scans, magnetic resonance imaging (MRI), positron emission tomography (PET) and bone scans. NSCLC staging describes the degree of spread of cancer cells from their original

source and is usually specified in the TNM system\*, where stage IA and IV are the best and the worst prognosis stages of NSCLC, respectively. Small cell lung cancer, on the other hand, is usually described as being limited (to one lung) or extensive (beyond one lung).

### 1.1.2 Lung Cancer Treatment

Treatment options for NSCLC are determined by the stage of cancer and include surgery (for less invasive NSCLC), radiation therapy, chemotherapy and targeted therapies.

**Chemotherapy:** In chemotherapy, specific types of drugs are given intravenously or taken orally to destroy cancer cells, over a period of several weeks to months. Immune system malfunctioning, fatigue, hair loss, bleeding, gastrointestinal distress, damage to other organs (heart, liver, kidney, inner ear, brain) are a number of side effects associated with chemotherapy.

**Radiation therapy:** Radiation therapy involves using ionizing radiation to damage the DNA of cancerous cells, causing them to die or reproduce more slowly. Depending on the position of the radiation source, there are three types of radiation therapy, namely, external radiation therapy (e.g., X-Knife<sup>TM</sup>, CyberKnife<sup>®</sup>, Clinac<sup>®</sup> and Gamma Knife<sup>®</sup>), internal radiation therapy (low-dose (LD) and high-dose (HD) brachytherapy<sup>†</sup>) and systematic radiation therapy (given by infusion or oral ingestion). Fibrosis<sup>‡</sup>, fatigue, hair loss, heart disease, gastrointestinal distress, cognitive decline, and cancer recurrence are among side effects of such treatment.

**Surgical resection:** Lung cancer surgery involves removing or ablating part of a lung that is cancerous. The procedure is particularly feasible in patients with early stage lung cancer, since not much of the lung function will be left if it is done for

---

\* Tumor-node-metastasis, a cancer classification system developed by the American Joint Committee on Cancer (AJCC) and the Union for International Cancer Control (UICC).

† Placing sealed radioactive sources precisely in the area under treatment.

‡ Less elastic tissue under radiation.

advanced stages of lung cancer. By degree of invasiveness, surgical resection may be performed openly or minimally invasively. Minimally invasive lung surgery involves making small incision(s) in the chest or back of the patient and between the ribs to insert several slender miniaturized instruments within the chest cavity to perform the surgery. By contrast, an open surgical procedure requires a large incision to access the area of interest. In comparison, minimally invasive surgery (MIS) causes less pain and trauma, speeds up recovery time and reduces post-operative complications, and it is usually preferable over open surgery. Both methods, however, may cause several side effects such as bleeding, infection, internal organ injury, blood vessel injury, vein or lung blood clotting, breathing complications and in some cases death. Tables 1.1 and 1.2 list various lung preserving surgery techniques that are being performed nowadays.

Lobectomy, the surgical excision of a lobe of the lung, has been the standard resection for early stage lung cancer based on a single randomized trial [4] that showed a higher locoregional recurrence rate associated with sublobar (wedge or segmentectomy) resection<sup>§</sup>. However, poor cardiac/pulmonary function is the major cause of surgical ineligibility in about 14% [5] to 25.5% [6] of early stage lung cancer patients. Even eligible patients who have undergone lobectomy may not be qualified for a second curative surgery should a second lung cancer develop, due to impaired lung function. Ineligible patients must, therefore, undergo chemotherapy and/or radiation therapy that tend to have higher side effects and lower survival rates [5]. Newer imaging modalities and a better understanding of the relationship between imaging features and the invasiveness of lung tumours may allow patients to be selected for lung conserving (sublobar) resection with equivalent outcomes to lobectomy. In a single-institution retrospective review [7], it has been shown that sublobar resection can be safely done for elderly patients (aged > 75 years) with a limited life expectancy and pulmonary reserve. In addition, segmentectomy should be considered in patients with peripheral early NSCLC [8]. A multicentre, randomized study of lobectomy ver-

---

<sup>§</sup> A triangle-shaped slice of tissue is removed during wedge resection. In segmentectomy, however, a surgeon removes a larger portion of the lung lobe than a wedge resection, but does not remove the whole lobe.

Table 1.1: Comparison of lung preserving surgery techniques [3]

Surgery technique	Who?	How?	Advantages	Disadvantages
Wedge resection	Early stage NSCLC (Stages IA-B, IIA)	Removing a triangle-shaped slice of tissue; stapling/stitching the residual	Gold standard for small nodules; easy for VATS	Removes a large amount of healthy lung tissue; not suitable for non-peripheral tumours
Cautery resection	Multifocal lesions, inoperable patients (segmentectomy, lobectomy)	Inflated lung; using fine-tipped cautery forceps, very small bites of tissue are coagulated and incised with scissors	Precise; sealed blood vessels and bronchi	Not ideal for VATS due to inflated lung; smoke, sticking of charred tissue to the electrodes, bleeding before coagulation
Laser resection	Multifocal lesions, inoperable patients (poor residual lung function)	80 KW/cm of 1318 nm laser; up to 100 metastases per lung and tumours of up to 8 cm diameter can be resected	Sparing lung tissue; minimal damage to adjacent tissue	Tedious and time consuming; initial financial investment, staff education and training in security and handling; high performance evacuation system
LigaSure <sup>TM</sup> system	Used for mid-size vessels and bronchi sealing	Electrothermal bipolar device, for nonanatomic staplerless pulmonary resection (vessels < 7 mm, bronchi < 4 mm)	Similar to stapler (time, bleeding) with less difficulty in MIS manipulation	Longer operative time for deeply located lesions; unsafe for excising lesions near the hilum or the great vessels
Ultrasonic scalpel	General purpose device for hemostasis and bronchi sealing	High-power low-frequency ultrasonic energy coagulates and cuts soft tissue by denaturing protein	Minimal thermal damage and smoke; applicable near vulnerable structures	Current ultrasonic scalpels are long and bulky; not flexible enough for tissue manipulation



Table 1.2: Comparison of lung preserving surgery techniques [3] (continued)

Surgery technique	Who?	How?	Advantages	Disadvantages
Saline-enhanced thermal sealing	Applicable in both open and minimally invasive procedures	Continuous flow of electroconductive saline to tissue using a monopolar floating ball device or a bipolar sealing forceps; thermal cut/hemostasis	Less thermal injury than electrocautery; small coagulative necrosis depth	More time consuming than electrocautery and laser procedures; removing more functional lung tissue than necessary (needs experience)
Thermoablation	Radiofrequency	Inoperable patients (poor pulmonary function); tumours of up to 3.5 cm	Radiofrequency ablation (400-500 kHz); percutaneous insertion of electrodes into the lesion under imaging guidance (US, CT or MRI)	Do not require general anesthesia; low risk and well tolerated
	Microwave	Inoperable patients (concurrent contraindications); local control	Microwave frequency $\geq 900$ MHz; percutaneous or open surgery under CT imaging guidance; oscillation of water molecules leads to thermocoagulation	No grounding pad burns; better heating zone than radiofrequency
	Cryoablation	Inoperable patients; local control	10-8-10 minutes of freeze-thaw-freeze cycles using an argon-based Cryo-ablation system (rigid bronchoscope or percutaneously)	Preserving collagenous in frozen tissues; better CT visualization
				Limited to local treatment

sus sublobar resection for small ( $< 2$  cm) peripheral NSCLC is currently ongoing [9]. It is expected to yield important insights regarding an optimal approach to resection surgery.

### 1.1.3 Minimally Invasive Image-Guided Tumor Resection

Preserving lung function and reducing the trauma of open thoracotomy<sup>¶</sup> can be achieved through MIS. The procedure typically involves remote manipulation of several long slender tools (laparoscopic devices) through a number of small incisions (10 mm wide) in the patient's chest and indirect visualization of the surgical field by a miniature camera or an endoscope.

Imaging (especially CT, magnetic resonance imaging (MRI), and positron emission tomography (PET)) plays an important role in determining the shape and location of lung tumours preoperatively, and hence the pretreatment clinical staging. Based on multimodal preoperative imaging, a thoracic surgeon needs to ensure that all malignant cells are excised thoroughly during surgery. In open surgery, the surgeon usually relies on direct palpation of the deflated lung to confirm tumour location and to find others that were not detected during preoperative imaging. Direct palpation usually gives a qualitative assessment of nodule stiffness since tumours are typically an order of magnitude stiffer than normal soft tissue. During robot-assisted or video-assisted MIS, however, the tumour often moves due to lung collapse, the inflated thoracic cavity and cardiac and respiratory motion. The loss of direct touch, due to the use of laparoscopic tools through small incisions, complicates tumour localization and excision procedures. To address this issue, image-guided techniques using intraoperative imaging/tracking systems are becoming available in operating rooms. In addition, tactile/kinaesthetic/ultrasonic sensors [10–12] located on laparoscopic tools as well as stereoscopic miniature cameras, are expected to further improve tumour localization in the near future.

---

<sup>¶</sup>Thoracotomy is the process of making a cut into the chest wall.

## 1.2 Lung Cancer: From Diagnosis to Treatment

There are a number of challenges associated with lung cancer diagnosis and treatment that form the structure and objectives of this thesis.

### 1.2.1 Motion Compensation

Percutaneous procedures are regularly used for minimally invasive diagnosis and treatment of lung cancer; however, tissue motion during the procedure often presents a significant challenge and can reduce the accuracy of these procedures [13,14]. The motion of the lung itself is a modulated movement that includes low-frequency respiration and higher-frequency heart beats [15,16]. While image-guided systems can compensate for lung motion, they often expose the patient and clinician to undesirable radiation [14,16]. As an alternative, image-guided robotics-assisted lung needle insertion has been studied for cancer diagnosis and treatment by several researchers [13,14,17]. These systems can reduce radiation exposure to clinicians; however, low frame rate of CT scanning together with the significant computational cost of image processing present significant challenges to the use of CT imaging for real-time tissue motion compensation. Another approach to compensate for modulated motion while performing a percutaneous procedure (such as lung needle biopsy or LD/HD brachytherapy) is to measure contact forces and adjust the tool position accordingly.

### 1.2.2 Tumor Targeting in Lung Needle Biopsy and Brachytherapy

The use of flexible needles in percutaneous interventions such as biopsy, drug delivery, brachytherapy, neurosurgery and tumour ablation has attracted many researchers. In particular, when target points are not directly accessible inside soft tissue, this type of intervention is appealing. Needle tip misplacement can, however, degrade the effectiveness of the therapy or diagnosis. In this context, robotics-assisted needle intervention has been proposed as a solution to enhance targeting accuracy [18]. Nonetheless, targeting inaccuracies still occur due to effects such as (1) target move-

ment as a result of soft tissue deformation, (2) needle bending due to the complex nature of needle–tissue interaction, and (3) inhomogeneity and anisotropy of real organic tissue [19].

In order to increase targeting accuracy, the complex interaction between the needle and soft tissue has been under investigation by many researchers. Okamura et al. [20] were the first to define needle insertion as a three-phase procedure, namely pre-puncture, post-puncture and retraction or needle withdrawal. Hence, it is reasonable to assume that by controlling or at least minimizing interaction effects, soft tissue deformation can be significantly reduced, which in turn would result in better targeting accuracy for needle-based interventional procedures. Biopsy procedures, in general, and lung needle biopsy/brachytherapy, in particular, will be enhanced by developing such technique.

### 1.2.3 MIS Sublobar Dissection Instrument

The current standard procedure for MIS wedge resection involves the use of an endoscopic stapler that cuts an unnecessarily large chunk of lung mass around a suspicious area and staples the cut surface to stop bleeding and air leakage. However, the expansion of the lung after using stapler devices is restricted by the stapling lines, which are folded on the edge of the lung parenchyma [21].

Alternatively, a lung mass can be carved out with electrocautery<sup>||</sup> and the lung parenchyma sutured. This is, however, more challenging than wedge resection with staples due to the generated smoke, suction and the complexity of endoscopic suturing. The application of an ultrasonically activated scalpel<sup>\*\*</sup> for cutting lung parenchyma has been shown to have an equivalent outcome to stapling [22–24], especially for blood vessels and bronchioli under 0.1 cm in diameter [24]. However, the postoperative

---

<sup>||</sup> An electrocautery device cuts and/or coagulates biological soft tissue by means of a high-frequency electric current which directly heats the tissue.

<sup>\*\*</sup> Ultrasonic scalpels can cut and/or coagulate biological soft tissues by means of high-power (10–1000 W/cm<sup>2</sup>) low-frequency (20–100 kHz) mechanical vibrations. A blade that vibrates at an ultrasonic frequency and delivers a small vibration amplitude (20–100  $\mu$ m P–P) cuts through soft tissue and denatures protein, and hence is able to stop any bleeding.

wound healing was observed to be delayed because of the thick coagulation necrosis (coagulum) generated by the harmonic scalpel [21]. Moreover, MIS ultrasonic scalpels tend to have a smaller workspace compared to MIS electrocautery devices, due to their rigid structure and lack of dexterity at the instrument tip.

Nonetheless, using any of these resection modalities for sublobar resection (segmentectomy and wedge resection) leads to the removal of an unnecessarily asymmetric and disproportionate amount of normal lung tissue. Hence, it is expected that by developing a robotics-assisted articulating ultrasonic scalpel, the lung tumour excision procedure will become more effective, while excellent hemostasis and a sealed cut surface will make the use of a stapler redundant. This approach may lead to a new treatment of lung cancer at early stages; hence, a larger group of patients may qualify for surgical treatment.

### 1.3 Thesis Outline and Organization

In this thesis, three main challenges of lung cancer diagnosis and treatment are addressed through four major developments. In Chapter 2, a mechatronic solution is proposed to compensate for undesirable modulated motion of soft tissue during needle insertion in the lung. This is followed by a novel needle insertion technique in Chapter 3, where a significant reduction in needle–tissue friction force is observed by modulating high-frequency low-amplitude vibration onto an inserting needle. In Chapter 4, a systematic design approach is proposed to design a miniaturized ultrasonic scalpel for internal body applications. The systematic design of an ultrasonic scalpel is extended to a more general case in Chapter 5, where the importance of choosing a proper geometric profile of the scalpel is demonstrated. In Chapter 6, a robotics-assisted articulating instrument is presented that adds dexterity to the miniaturized ultrasonic scalpel described in Chapters 4 and 5. All the proposed developments share a common feature in terms of physical oscillatory motion. For the motion compensation challenge, it will be demonstrated how low-frequency periodic mechanical oscillations can help to compensate for the body’s naturally occurring periodic respiratory motion during robotics-assisted lung needle insertion. The effect of inducing mid-range

frequency vibration on a medical needle will then be discussed in the context of needle insertion and tumour targeting. Lastly, it will be discussed how high-power ultrasonic vibration can be generated in an articulating surgical instrument to address the issue of soft tissue dissection with more dexterity and maneuverability.

The thesis is presented using the integrated article format and each of the Chapters 2–6 includes a complete description of the corresponding work as well as review of the related literature. Chapter 7 contains an overall conclusion for the work with suggestions for future research. An outline of the work in each part of the thesis is as follows:

- Chapter 2 starts with an introduction to the problem of lung modulated motion during percutaneous intervention, followed by a description of the Macro–Micro mechatronic solution for compensating tissue motion during robotics-assisted needle insertion. Experimental results show the efficacy of employing the proposed Macro–Micro platform in 1-D motion compensation of a moving soft tissue.
- Chapter 3 starts with an introduction to the use of flexible needles in robotics-assisted percutaneous interventions and discusses the challenges associated with achieving good targeting accuracy. A vibration-assisted needle insertion technique and its corresponding mathematical model for reducing frictional effects are introduced next. Several experimental results using piezoelectric actuators are discussed later on which confirm the feasibility of the proposed technique in reducing friction forces.
- The systematic optimal design of a miniaturized ultrasonic scalpel is described in Chapter 4, with an introduction on the structure of ultrasonically activated devices. Due to the large number of design variables, an equivalent circuit model is utilized to simplify the design problem and reformulate it as a constrained multi-objective optimization problem with only two independent variables. Finite element analysis is used afterwards to evaluate the performance of the optimal design. The results of modelling, optimization and finite element analysis are then given in the last section for a case study.
- Chapter 5 continues the design of a miniaturized ultrasonically activated scalpel

to further enhance the reliability of such device. First, a complimentary introduction is given on ultrasonic scalpels and the existing techniques that are being used for amplifying small vibration amplitude are discussed. The mathematical foundations of a spline-based mechanical vibration amplifier are discussed next, and the problem is solved for a case study.

- Chapter 6 starts with an introduction to robotics-assisted surgical instruments with articulating tip to provide additional dexterity during surgical procedures. The design of a robotics-assisted surgical wrist with an optimal ultrasonic scalpel is then proposed. The miniaturized ultrasonic scalpel design to be integrated within the articulating mechanism is revisited from Chapter 4. The developed articulating mechanism and the miniaturized ultrasonic knife at the tip of a daVinci<sup>®</sup> instrument is finally showcased.

## References

- [1] “Cancer fact sheet n-297 by World Health Organization,” <http://www.who.int/mediacentre/factsheets/fs297/en/>, February 2014.
- [2] A. C. Society, “Cancer facts and figures 2010,” 2010, Atlanta: American Cancer Society.
- [3] F. Venuta, A. Rolle, M. Anile, N. Martucci, B. Bis, and G. Rocco, “Techniques used in lung metastasectomy,” *Journal of Thoracic Oncology*, vol. 5, no. 6, pp. S145–S150, 2010.
- [4] R. Ginsberg and L. Rubinstein, “Randomized trial of lobectomy versus limited resection for T1 N0 non-small cell lung cancer. Lung Cancer Study Group.” *The Annals of Thoracic Surgery*, vol. 60, no. 3, pp. 615–623, Sep. 1995.
- [5] R. McGarry, G. Song, P. des Rosiers, and R. Timmerman, “Observation-only management of early stage, medically inoperable lung cancer,” *Chest*, vol. 121, no. 4, pp. 1155–1158, Apr. 2002.
- [6] S. Baser, V. Shannon, G. Eapen, C. Jimenez, A. Onn, L. Keus, E. Lin, and R. Morice, “Pulmonary dysfunction as a major cause of inoperability among patients with nonsmall-cell lung cancer,” *Clinical Lung Cancer*, vol. 7, no. 5, pp. 344–349, 2006.
- [7] A. Kilic, M. Schuchert, B. Pettiford, A. Pennathur, J. Landreneau, J. Landreneau, J. Luketich, and R. Landreneau, “Anatomic segmentectomy for stage I non-small cell lung cancer in the elderly,” *The Annals of Thoracic Surgery*, vol. 87, no. 6, pp. 1662–1668, Jun. 2009.



- [8] T. Chamogeorgakis, C. Ieromonachos, E. Georgiannakis, and D. Mallios, “Does lobectomy achieve better survival and recurrence rates than limited pulmonary resection for T1N0M0 non-small cell lung cancer patients?” *Interactive Cardio-Vascular and Thoracic Surgery*, vol. 8, no. 3, pp. 364–372, Mar. 2008.
- [9] N. C. Institute, “Phase III randomized study of lobectomy versus sublobar resection in patients with small peripheral stage IA non-small cell lung cancer,” <http://www.cancer.gov/clinicaltrials/CALGB-140503>, Retrieved July 2014.
- [10] M. Perri, A. Trejos, M. Naish, R. Patel, and R. Malthaner, “New tactile sensing system for minimally invasive surgical tumour localization,” *The International Journal of Medical Robotics and Computer Assisted Surgery*, vol. 6, no. 2, pp. 211–220, 2010.
- [11] M. Perri, A. Trejos, M. Naish, R. Patel, and R. Malthaner, “Initial Evaluation of a Tactile/Kinesthetic Force Feedback System for Minimally Invasive Tumor Localization,” *IEEE/ASME Transactions on Mechatronics*, vol. 15, no. 6, pp. 925–931, 2010.
- [12] V. Hornblower, E. Yu, A. Fenster, J. Battista, and R. Malthaner, “3D thoracoscopic ultrasound volume measurement validation in an ex vivo and in vivo porcine model of lung tumours,” *Physics in Medicine and Biology*, vol. 52, no. 1, pp. 91–106, Jan. 2007.
- [13] S. Xu, G. Fichtinger, R. H. Taylor, F. Banovac, and K. Cleary, “CT fluoroscopy-guided robotically-assisted lung biopsy,” in *Medical Imaging*. International Society for Optics and Photonics, 2006, pp. 61 411L–61 411L.
- [14] L. B. Kratchman, M. M. Rahman, J. R. Saunders, P. J. Swaney, and R. J. Webster III, “Toward robotic needle steering in lung biopsy: a tendon-actuated approach,” in *SPIE Medical Imaging*. International Society for Optics and Photonics, 2011, pp. 79 641I–79 641I.
- [15] L. Maier-Hein, A. Tekbas, A. Seitel, A. Franz, B. Radeleff, F. Pianka, S. Müller, S. Satz, R. Tetzlaff, I. Wolf *et al.*, “Computer-assisted needle insertion for ab-

- dominal interventions,” in *World Congress on Medical Physics and Biomedical Engineering, September 7-12, 2009, Munich, Germany*. Springer, 2009, pp. 159–162.
- [16] P. J. Keall, G. S. Mageras, J. M. Balter, R. S. Emery, K. M. Forster, S. B. Jiang, J. M. Kapatoes, D. A. Low, M. J. Murphy, B. R. Murray *et al.*, “The management of respiratory motion in radiation oncology report of AAPM Task Group 76a,” *Medical physics*, vol. 33, no. 10, pp. 3874–3900, 2006.
- [17] E. Yu, C. Lewis, A. L. Trejos, R. V. Patel, and R. A. Malthaner, “Lung cancer brachytherapy: robotics-assisted minimally invasive approach,” *Current Respiratory Medicine Reviews*, vol. 7, no. 5, pp. 340–353, 2011.
- [18] N. Abolhassani, R. Patel, and M. Moallem, “Needle insertion into soft tissue: A survey,” *Medical Engineering & Physics*, vol. 29, no. 4, pp. 413–431, 2007.
- [19] A. Asadian, M. R. Kermani, and R. V. Patel, “A novel force modeling scheme for needle insertion using multiple kalman filters,” *IEEE Transactions on Instrumentation and Measurement*, vol. 61, no. 2, pp. 429–438, 2012.
- [20] A. M. Okamura, C. Simone, and M. D. O’Leary, “Force modeling for needle insertion into soft tissue,” *IEEE Transactions on Biomedical Engineering*, vol. 51, no. 10, pp. 1707–1716, 2004.
- [21] K. Takagi, Y. Hata, S. Sasamoto, K. Tamaki, K. Fukumori, H. Otsuka, C. Hasegawa, and K. Shibuya, “Late onset postoperative pulmonary fistula following a pulmonary segmentectomy using electrocautery or a harmonic scalpel,” *Annals of Thoracic and Cardiovascular Surgery*, vol. 16, no. 1, pp. 21–25, Aug. 2010.
- [22] T. Molnar, Z. Szanto, T. Laszlo, L. Lukacs, and O. Horvath, “Cutting lung parenchyma using the harmonic scalpel—an animal experiment,” *European Journal of Cardio-Thoracic Surgery*, vol. 26, no. 6, pp. 1192–1195, Dec. 2004.

- 
- [23] S. Yamada, K. Yoshino, and H. Inoue, “New-model ultrasonically activated shears for hemostatic sectioning during video-assisted thoracic surgery,” *General Thoracic and Cardiovascular Surgery*, vol. 55, no. 12, pp. 518–520, Dec. 2007.
- [24] U. Eichfeld, A. Tannapfel, M. Steinert, and T. Friedrich, “Evaluation of ultrason in lung metastatic surgery,” *The Annals of Thoracic Surgery*, vol. 70, no. 4, pp. 1181–1184, Oct. 2000.

# Chapter 2

## Motion Compensation for Needle Insertion

### 2.1 Introduction

Percutaneous procedures are regularly used for minimally invasive diagnosis and treatment of lung cancer; however, tissue motion during the procedure often presents a significant challenge and can reduce the accuracy of these procedures [1, 2]. The motion of the lung itself is a modulated movement that includes low-frequency respiration and higher-frequency heart beats [3, 4]. Image-guided robotics-assisted lung needle insertion has been studied for cancer diagnosis and treatment by several researchers [1, 2, 5]. While image-guided systems can compensate for lung motion, they often expose the patient and clinician to undesirable radiation [2, 4].

In [1], CT fluoroscopy imaging is used to detect lesion motion in nearly real-time. A robotic arm is then used to orient and guide a biopsy needle to a tumor. However, during needle insertion the patient is required to hold his/her breath to ensure accurate targeting. Kratchman *et al.* [2] designed a tendon-driven biopsy needle steering system to account for trajectory error and tumor motion during lung biopsy. Their preliminary experiment was performed in free-space using feedback from a digital camera.

In the literature, some work has been reported on real-time image-based motion estimation [6, 7] and image-guided robotic motion compensation [8]; however, the

---

This chapter contains material published in S. Farokh Atashzar, Iman Khalaji, Mahya Shahbazi, Ali Talasaz, Rajni V. Patel, and Michael D. Naish, “Robot-assisted lung motion compensation during needle insertion,” in *IEEE International Conference on Robotics and Automation (ICRA)*, Karlsruhe, Germany, 2013, pp. 1682-1687.

latency introduced by image processing is a considerable challenge. Predictive methods have been proposed to deal with this issue. The extended Kalman predictor [9] and augmented sensory measurements such as multi-modality image registration [10] and fusing image and electrocardiogram (ECG) data [11] are some examples of such predictive techniques. However, there are still practical obstacles for image-based motion compensation such as unacceptable tissue deformation, low frequency bandwidth, prediction error, and image-processing faults (caused by the low signal-to-noise ratio of ultrasound images, as well as blocked field of view, optical illumination and image Jacobian singularities in visual servoing) [6, 12].

In order to address the practical challenges associated with image-based synchronization, force-based motion compensation has been studied in [13–15]. In [13], a predictive force controller has been proposed for surgical applications. In [14], a 6 degrees-of-freedom (DOF) force sensor is mounted outside of the patient’s body at the base of the tool to compensate for 3-D tissue motion. In [15], a hand-held device is designed to keep the contact of a magnetic rod and beating heart surface stable in 1-D using the interactional force and ECG signals. Unfortunately, the control techniques in [14] and [15] cannot be used for lung needle insertion, since any additional interaction force required for needle insertion will be cancelled out as undesirable disturbances. Moreover, any interaction forces between the surgical tool and the patient’s body will be problematic. It should also be noted that the main challenges of force-based synchronization schemes are questionable stability and low performance that cause undesirable jerky and potentially unsafe motions [12, 16]. In order to address this issue, a combined force and pose control technique is proposed in [12] and [16] for beating-heart annuloplasty, where data from ultrasound images are fused with miniaturized uniaxial force sensor data. The authors show that feed-forward motion terms together with the force control terms can be a more appropriate alternative to smoothly cancel out 1-D motion between the hand-held device and heart tissue. It has been shown [9] that for annuloplasty procedures, 1-D compensation can cover the majority of the undesirable relative motion.

There are various technical problems associated with the use of image data in the control architecture of surgical robots. The problem is even more challenging for

lung tissue. First, CT imaging has an unacceptable frame rate for real-time robotic control systems. “Look-and-move” algorithms and multi-modality image fusion are usually sought for lung needle insertion to minimize X-ray exposure and overcome the low-sample rate of CT scanning [1, 2, 10]. However, potential challenges associated with the low update rate of “look-and-move” algorithms, together with the significant computational cost of image processing are the main concerns with using CT imaging for real-time tissue motion compensation. Ultrasound imaging has been proposed as an alternative for robotics-assisted needle insertion for lung brachytherapy [5], although it is difficult to use ultrasound as a stand-alone image modality for robot navigation, due to low signal-to-noise ratio. Moreover, air pockets within the inflated lung make ultrasound imaging almost impossible during percutaneous lung biopsy. Vision-based motion compensation is not applicable unless imaging markers are placed on the lung surface.

In this work, a macro–micro robotic solution is proposed to provide safe and smooth compensated motion for lung needle insertion (Fig. 2.1). The proposed framework utilizes an impedance controller to synchronize a biopsy needle with moving soft tissue in real time based on force interactions. This could minimize harmful X-ray radiation exposure to patients of current CT image-based synchronization approaches. It is expected that the proposed motion-compensated teleoperated needle insertion technique will enhance performance by providing a surgeon with the ability to guide a needle while keeping the needle motion smooth and synchronized with lung tissue. Furthermore, using a master–slave environment, the approach addresses the problem of the danger of X-ray exposure for the clinician.

## 2.2 Method

An overall diagram of the system architecture is given in Fig. 2.2. In this figure, the local impedance controller has the role of synchronizing the macro part with the moving soft tissue, while the micro part controller manipulates the micro part, which is attached on top of the macro part, using the received commands from the master side haptic device (physician). The entire interaction is modeled as a two-DOF

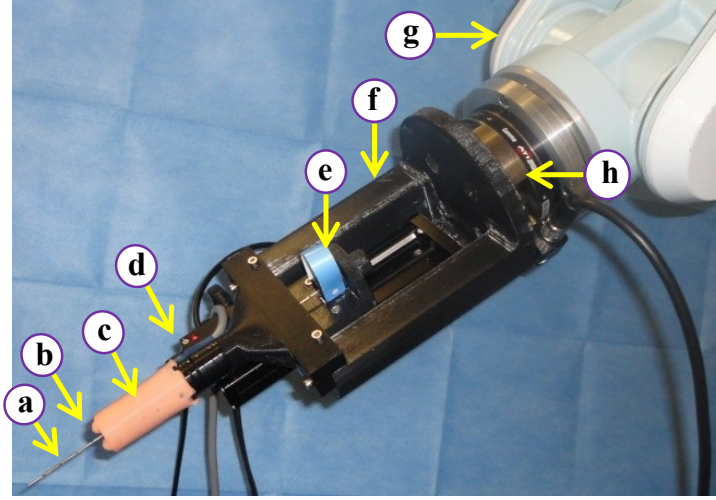


Figure 2.1: General view of the Macro-Micro architecture. (a) 18-gauge needle, (b) silicon skin and bumpers covering the pressure sensors, (c) macro shaft, (d) micro needle driver (a linear stage), (e) needle adapter to attach the needle to the micro driver, (f) macro part attachment, (g) macro driver (Mitsubishi PA-10 robot), (h) ATI Gamma force sensor (used for offline calibration of the pressure sensors).

vibratory system that includes three components: base impedance of the oscillatory motion, soft tissue (lung) and designed macro robot impedance. The base impedance connects the lung to the reference frame of the patient's body and causes modulated oscillation of the lung. Lung tissue impedance is responsible for deformation of the lung during motion tracking. Finally, the designed macro robot impedance between the base frame and the contact point ensures that the macro robot is tracking the motion of the lung tissue during needle insertion. Data from pressure sensors, mounted at the tip of the macro part, are used to provide input force to the designed macro robot impedance.

### 2.2.1 Mechanical Model

Lung oscillates due to modulation of respiration and heartbeat forces. Now, suppose that there is a system that barely touches a region of interest of the lung and tracks its movement while resulting in a small force between the lung and the tool. Ideally, the amplitude of the interaction force should be small enough to make the deformation of the lung minor and minimize tissue damage. Consequently, the ideal behavior is

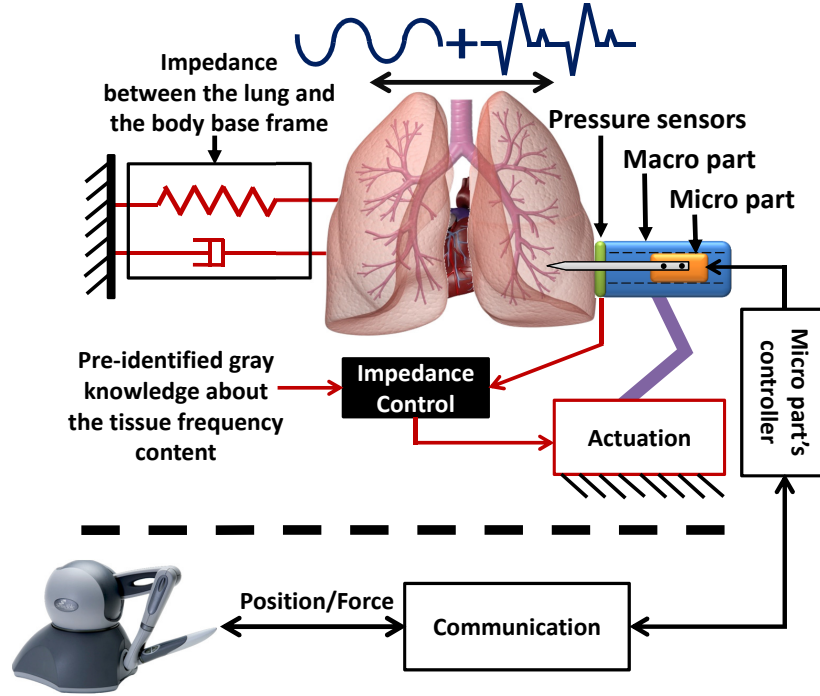


Figure 2.2: The overall system architecture.

equivalent to having a synchronized movement of tissue and robot, which minimizes the tissue deformation. Without loss of generality, the system described above can be simplified as a two-DOF vibratory system, as illustrated in Fig. 2.3. When the tool is not in contact with the lung, the lung is free to vibrate due to respiratory and heart motion. However, the motion is not position controlled since both the heart and diaphragm impedances are actuated by various muscle forces. In other words, once the synchronizing tool touches lung tissue, it will have an effect on the motion of the lungs and heart. This effect is not surprising, as active/passive heart stabilizers [17] minimize motion of a region by applying high counteracting forces through air suction.

In the current 2-DOF vibratory model, the oscillatory motion of lung tissue is assumed to be caused by a linear mass-spring-damper system, where the mass,  $M_1$ , represents all of the masses (including portions of lung tissue, heart and other connecting tissues) on which the tool has effect upon contact. The synchronizing tool is assumed to be controlled by a robot whose controller impedance is represented by



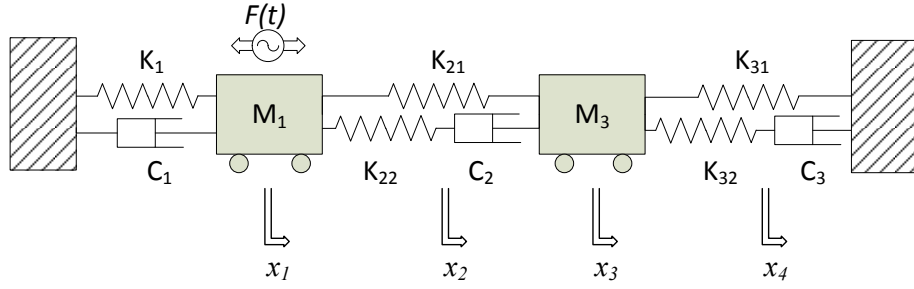


Figure 2.3: 2 DOF vibratory system.

$Z_3$  (including  $M_3$ ,  $K_{31}$ ,  $K_{32}$  and  $C_3$ , see Fig. 2.3). Lung soft tissue is modeled as a linear viscoelastic material (Kelvin model [18]) since the deformation induced on the tissue is small. Let us assume that an oscillating force is applied on the mass  $M_1$ . Moreover, we can assume that the impedance controller  $Z_3$  has been designed in such a way that the system forms a 2-DOF vibratory system. Since there is no actual spring that connects the soft tissue and the tool tip in tension, we can bias lung tissue deformation by a desired small force,  $F_{bias}$ . In other words,  $F_{bias}$  will always be subtracted from the absolute contact force and therefore, contact force will have both negative (compression) and positive (tension) values.

Considering the linear viscoelastic tissue model, the 2-DOF vibration equation can be readily derived as:

$$\begin{Bmatrix} X_1(s) \\ X_3(s) \end{Bmatrix} = [\mathbf{A}]^{-1} \begin{Bmatrix} F(s) \\ 0 \end{Bmatrix} \quad (2.1)$$

where

$$A(1,1) = M_1 s^2 + C_1 s + K_1 + K_{21} + K_{22} - \frac{K_{22}^2}{C_2 s + K_{22}}, \quad (2.2)$$

$$A(1,2) = A(2,1) = -\frac{K_{22} C_2 s}{C_2 s + K_{22}} - K_{21}, \quad (2.3)$$

$$A(2,2) = M_3 s^2 + C_2 s + K_{31} + K_{32} + K_{21} - \frac{K_{32}^2}{C_3 s + K_{32}} - \frac{C_2^2 s^2}{C_2 s + K_{22}}. \quad (2.4)$$

In the above equations,  $s$  is the Laplace variable and  $X_1(s)$ ,  $X_3(s)$  and  $F(s)$  are Laplace transformations of the soft tissue displacement, tool displacement and oscil-

latory force, respectively.  $M_1$ ,  $C_1$  and  $K_1$  are the mass, spring and damper characteristics of the oscillatory motion caused by heartbeat of the soft tissue. Similarly,  $K_{21}$ ,  $K_{22}$  and  $C_2$  are viscoelastic properties of the soft tissue. Similarly,  $K_{31}$ ,  $K_{32}$  and  $C_3$  are viscoelastic properties of the tool controller that must be determined. In order to have the tool follow soft tissue, both the phase and amplitude of the input–output closed-loop system transfer function  $X_3(s)/X_1(s)$  at the desired frequency range should be investigated:

$$\frac{X_3(s)}{X_1(s)} = -\frac{A(2,1)}{A(2,2)}. \quad (2.5)$$

As can be seen from (2.5), tracking performance does not depend on the impedance of the oscillatory motion source.

## 2.2.2 Impedance Control Design

As mentioned earlier, it was assumed that both soft tissue and the impedance controller have linear viscoelastic properties. In order to incorporate the system uncertainties into the control scheme design, it is desirable to use a more general model that can also cover other unmodeled phenomena. For this purpose, we assume that each component of the system has a distinct impedance. A schematic dual electrical circuit of the 2-DOF vibratory system is shown in Fig. 2.4, where  $Z_1(s)$ ,  $Z_2(s)$  and  $Z_3(s)$  represent impedances of base oscillatory motion, soft tissue and the controller, respectively. Using the impedance analogy, force and velocity in the mechanical system are equivalent to voltage and current in the electrical circuit, respectively. Therefore, it can be shown that the circuit is a current divider and hence:

$$\frac{X_3(s)}{X_1(s)} = \frac{sX_3(s)}{sX_1(s)} = \frac{I_3(s)}{I_2(s) + I_3(s)} = \frac{Z_2(s)}{Z_2(s) + Z_3(s)}. \quad (2.6)$$

This equation supports the previous result that no matter what  $Z_1(s)$  is, the input/output behavior of the system,  $X_3(s)/X_1(s)$ , only depends on the soft tissue impedance,  $Z_2(s)$ , and the controller,  $Z_3(s)$ . However, it should be noted that stability of  $Z_1(s)$  is the necessary condition of the system internal stability. Considering

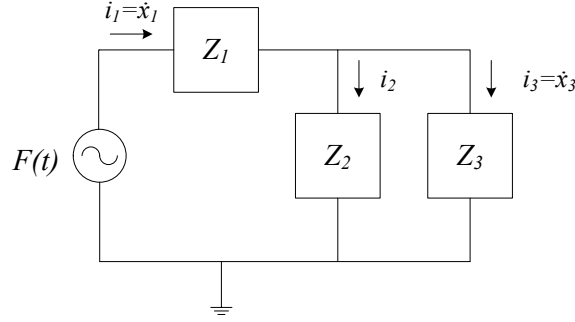


Figure 2.4: Schematic dual electrical circuit of the 2-DOF vibratory system.

(2.6), since  $Z_1(s)$ ,  $Z_2(s)$  and  $Z_3(s)$  are assumed as minimum phase proper stable subsystems, the stability of the whole system is guaranteed. It should be noted that the ultimate goal of the system is:

$$\frac{X_3(s)}{X_1(s)} = 1, \quad (2.7)$$

which means: (a) zero phase lag and (b) equivalent amplitude. Considering (2.7), the ultimate goal can be rephrased as zero tissue deflection for all frequencies, which is equal to perfect tracking of the tissue motion for all frequencies. In order to design the desired impedance  $Z_3(s)$  for the local robot controller, the following should be noted:

- We need to have high performance tracking within a specific frequency window, but we are not interested in having high frequency tracking. In the other words, we need to cancel out high frequency components of the motion including noise and jerks.
- It is not always possible to know the exact tissue impedance *a priori*, due to the unmodeled dynamics of the tissue behavior. In addition, dynamic behavior of a class of body organs rather than a specific case must be considered. Consequently, (2.6) should be rewritten as:

$$\frac{X_3(s)}{X_1(s)} = \frac{Z_2(s)(1 + \Delta_1(s)) + \Delta_2(s)}{Z_2(s)(1 + \Delta_1(s)) + \Delta_2(s) + Z_3(s)}, \quad (2.8)$$

where  $\Delta_1(s)$  represents the multiplicative uncertainty term and  $\Delta_2(s)$  repre-

sents the additive uncertainty of the identified model. Note that, both  $\Delta_1(s)$  and  $\Delta_2(s)$  include high frequency components.

- The stability of the system has to be guaranteed.

Based on the aforementioned points, we propose the desired impedance of the macro robot as:

$$Z_3(s) = \alpha(s)Z_2(s). \quad (2.9)$$

Considering (2.9), the closed loop input–output transfer function of the system can be calculated as:

$$\begin{aligned} \frac{X_3(s)}{X_1(s)} &= \frac{1 + \Delta_1(s) + \Delta_2(s)Z_2^{-1}(s)}{1 + \Delta_1(s) + \Delta_2(s)Z_2^{-1}(s) + \alpha(s)} \\ &= 1 - \frac{(1 + \alpha(s))^{-1} \alpha(s)}{1 + (1 + \alpha(s))^{-1} (\Delta_1(s) + \Delta_2(s)Z_2^{-1}(s))}. \end{aligned} \quad (2.10)$$

$\alpha(s)$  is a tuning factor and should be designed to optimize the performance while assuring stability. To choose a proper  $\alpha(s)$ , the followings facts should be considered:

***Fact I—(System Performance):***

It should be noted that in a specific case when  $|\alpha| \ll 1$  for all frequencies, the phase lag will be close to zero. In addition, the system gain will approach unity and the uncertainty does not have any effect on the system performance, which implies ideal tracking. However, considering  $|\alpha| \ll 1$  the bandwidth of the system will approach infinity, hence undesirable jerky motion will degrade the system performance. Accordingly, at high frequencies, a tradeoff between tracking accuracy and noise amplification should be performed. As a result, the designed  $\alpha(s)$  should provide small gain within the desired frequency range and high gain at high frequencies. Thus, the closed-loop transfer function should behave like a low-pass filter.

***Fact II—(System Stability):***

Besides system performance, the designed  $\alpha(s)$  should preserve system stability. According to (2.10) and considering that  $\alpha(s) + 1$  is a Hurwitz polynomial and using

the Nyquist stability theorem [19], the system stability condition is:

$$|1 + \alpha(s)| > \left| \Delta_1(s) + \Delta_2(s)Z_2^{-1}(s) \right|. \quad (2.11)$$

Note that,  $\Delta_1(s)$  and  $\Delta_2(s)Z_2^{-1}(s)$  have negligible amplitudes at low frequencies, but can provide considerable amplitudes at high frequencies. Consequently, in order to guarantee system stability,  $\alpha(s)$  should have high gain at high frequencies, which results in a low-pass filtering behavior for the closed-loop system. Therefore, when the identification is performed poorly, in order to ensure system stability, the bandwidth of the closed-loop system should be limited. This result is in line with Fact I.

**Remark I:**

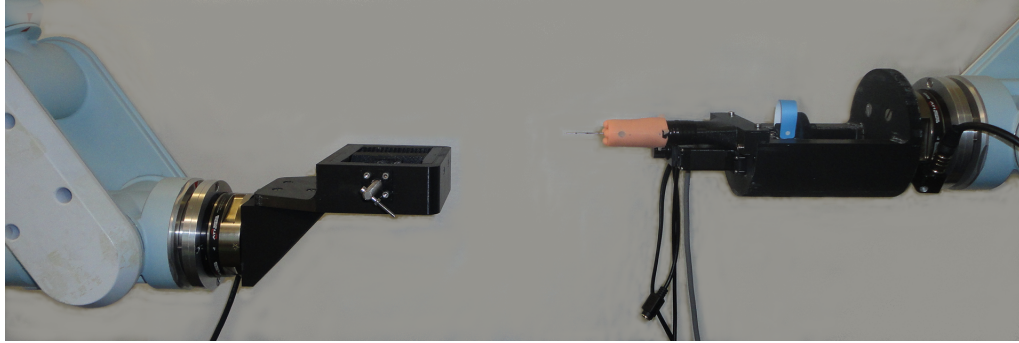
*Proper choice of  $\alpha(s)$  will result in low phase-lag within the desirable frequency window and a closed-loop gain near to unity while providing proper high-frequency filtering behavior in order to deal with the degrading effects of high-frequency noise and uncertainty. The high-frequency behavior of  $\alpha(s)$  should be chosen conservatively when the sensors are noisy and the identification is poor.*

After designing the desired impedance of the robot ( $Z_3$ ), it will be fed into the local controller [20].

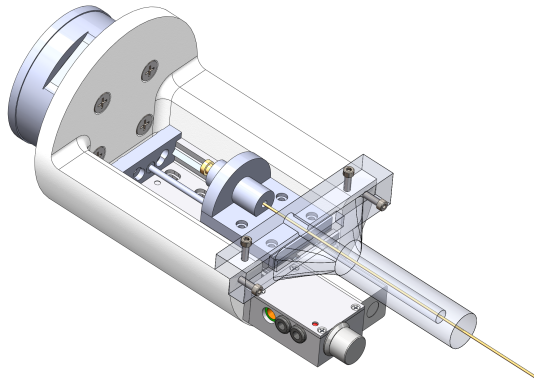
## 2.3 Prototype Design

In order to mimic needle insertion into a moving soft tissue, three components are needed: oscillatory motion of an animal tissue phantom, a macro robot for synchronization and a micro robot for needle insertion. The first two components are provided by two Mitsubishi PA-10 robots that are configured face-to-face, Fig. 2.5. The left robot arm is used to generate an arbitrary oscillatory motion in the soft tissue, while the robot on right synchronizes itself with the motion. An adjustable tissue holder is mounted on the left PA-10 robot with an ATI Gamma force sensor in between.

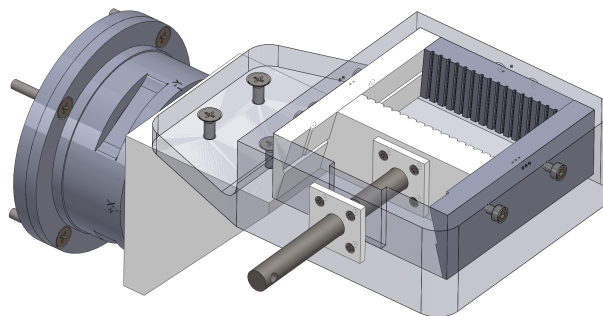
A T-LSM050B Miniature Motorized Linear Stage (Zaber Technologies Inc.) is used as the needle driver unit. The linear stage is mounted to the right PA-10 robot through an attachment. In order to mount a needle onto the linear stage, an



(a) Experimental setup



(b) CAD model of the macro robot attachment



(c) CAD model of the tissue holder

Figure 2.5: Experimental setup and corresponding CAD models.

adapter was manufactured through which 18 gauge brachytherapy needles can be manipulated. The tip portion of the needle passes through a cylindrical shaft that provides close-fitting support for the needle when it is being inserted into soft tissue. This minimizes needle deflection during insertion and enhances tumor targeting. On the tip of this cylindrical shaft, four FSR<sup>®</sup> 400 uniaxial pressure sensors (Interlink Electronics Inc.) are mounted in a circular 90° pattern around the needle support hole. Since these pressure sensors can be damaged by shear forces, a silicon skin-like sheath that incorporates four semi-hemispherical bumpers is used to both protect the sensors and to convert nonnormal contact forces in other directions into normal pressure.

## 2.4 Experimental Results

Using the components in Table I, several experiments were conducted to evaluate the system performance.

### 2.4.1 Experiment I

In this experiment, the operator was asked to apply varying forces in different directions to the pressure sensors. The resulting motion for two cases of loading are shown in Fig. 2.6 and Fig. 2.7. Fig. 2.6 illustrates the axial response of the system. Using the array of four pressure sensors, it is also possible to compensate for motion in the yaw and pitch directions, as shown in Fig. 2.7.

### 2.4.2 Experiment II

In this experiment, the local impedance controller synchronizes the whole system with the moving tissue. The operator's motion commands are sent through an Ethernet connection to the patient side to control the micro robot. Similarly, monitoring information from the procedure is transmitted back to the operator side. It is also possible to send the contact force data to the operator to relay a sense of palpation.

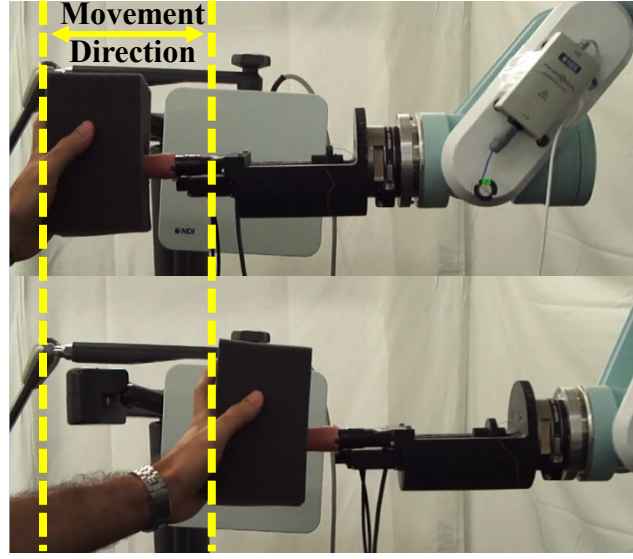


Figure 2.6: Motion compensation for axial movement.

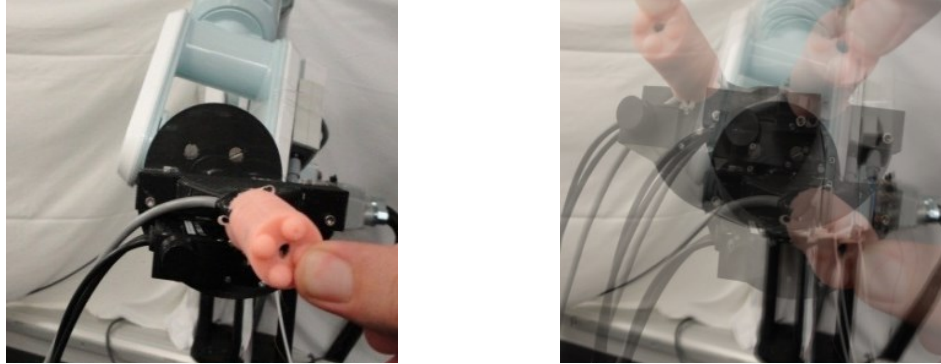


Figure 2.7: Motion compensation for various orientations.

Since the robot is synchronized with the tissue, the operator is able to insert the needle with ease.

#### 2.4.2.1 Step A: Identification

As mentioned in Section II.B, the tissue frequency content must be estimated for the impedance control synthesis. A simple identification procedure is employed when the tissue is kept stationary and the macro robot makes contact with the soft tissue. Using a position control scheme, the macro robot starts to vibrate harmonically, which results in small deformations of the tissue at low and high frequencies (0–20



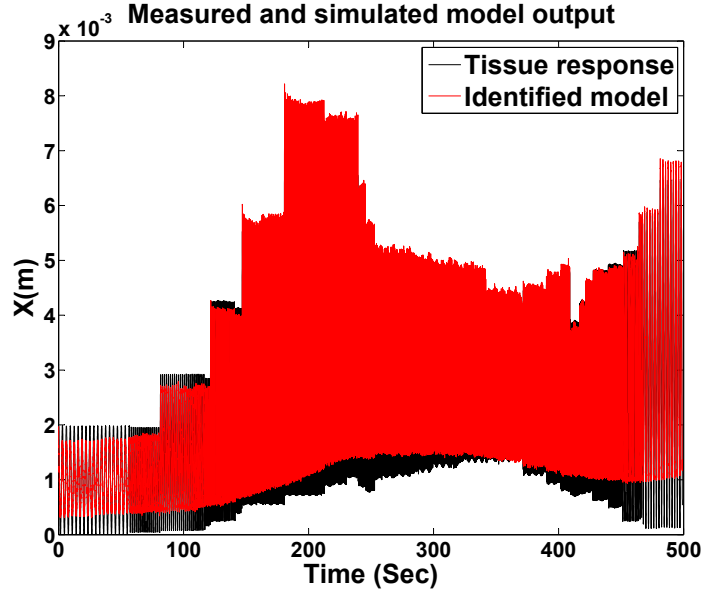


Figure 2.8: Comparison of the output of the identified system with the measured tissue deformation at variable frequencies.

Hz). The position and contact force are logged for offline identification. The output of the identified model is compared with tissue deformation in Fig. 2.8. Good agreement is observed using a linear viscoelastic model. The frequency content of the identified model is shown in Fig. 2.9.

#### 2.4.2.2 Step B: Local impedance controller

Based on the identified tissue impedance shown in Fig. 2.9 and designed  $\alpha(s)$  given in Fig. 2.10, the desired impedance of the controller can be obtained using (2.9) to minimize the phase lag. In the next step, the designed impedance is fed into the local controller. Fig. 2.11 evaluates the impedance controller performance, where the solid blue line corresponds to the robot position and the dashed red line corresponds to the desired impedance output during the compensation task. As can be seen from Fig. 2.11, the robot closely tracks the desired impedance.

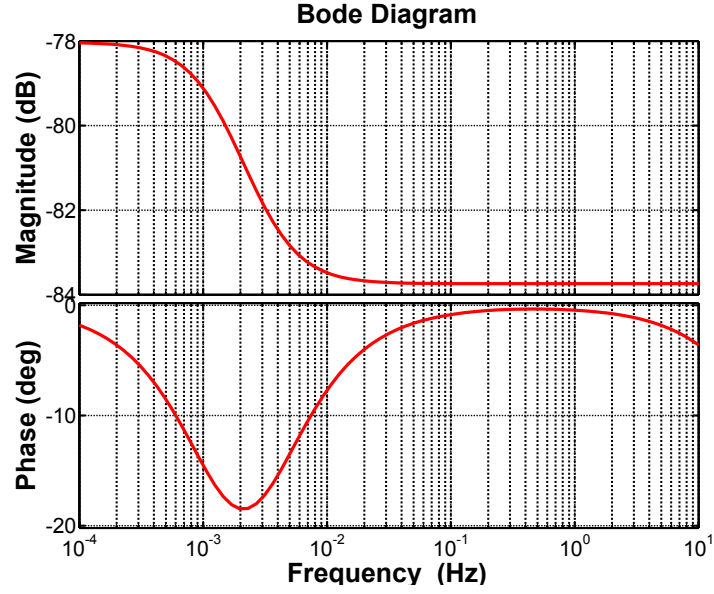
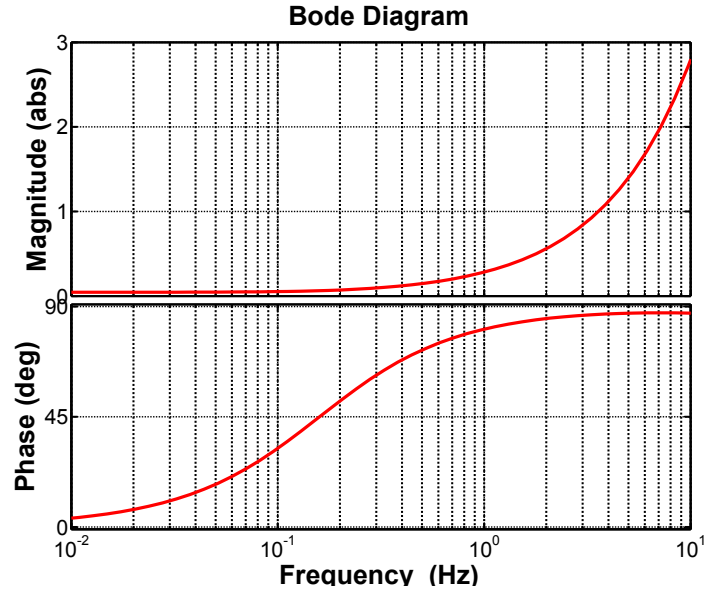


Figure 2.9: Bode plot of the identified soft tissue.

Figure 2.10: Bode plot of the designed  $\alpha(s)$ .

#### 2.4.2.3 Step C: Compensation performance

In order to analyze the main performance of the system, the motion of the needle and the contact point on the tissue holder is recorded in the same coordinate system using an NDI Aurora electromagnetic tracking system during two different phases (Phase

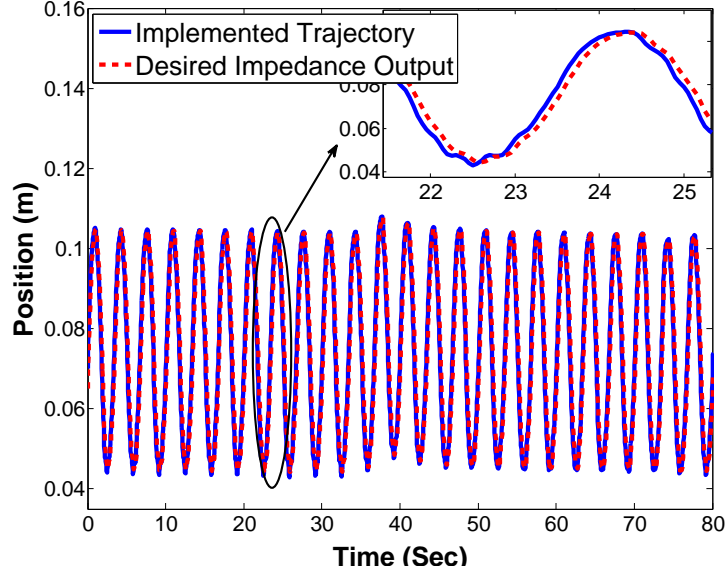


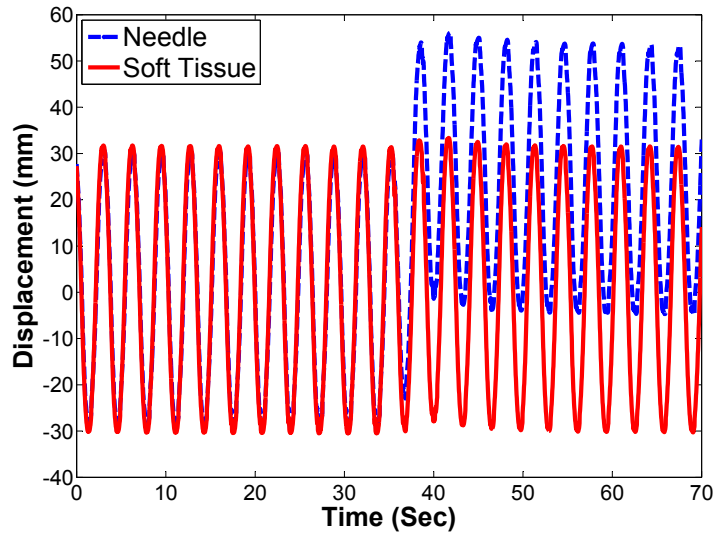
Figure 2.11: The performance of the local impedance controller.

I: synchronized contact, and Phase II: synchronized insertion). The performance output and the force exerted on the tissue holder are shown in Fig. 2.12. As can be seen when the needle was outside the tissue, the proposed impedance controller synchronizes the system with the tissue movement. After the start of needle insertion, a transient increase in force amplitude is observed and after that point, a simple shift can be seen in the position trajectory that is equal to the desired depth assigned by the operator.

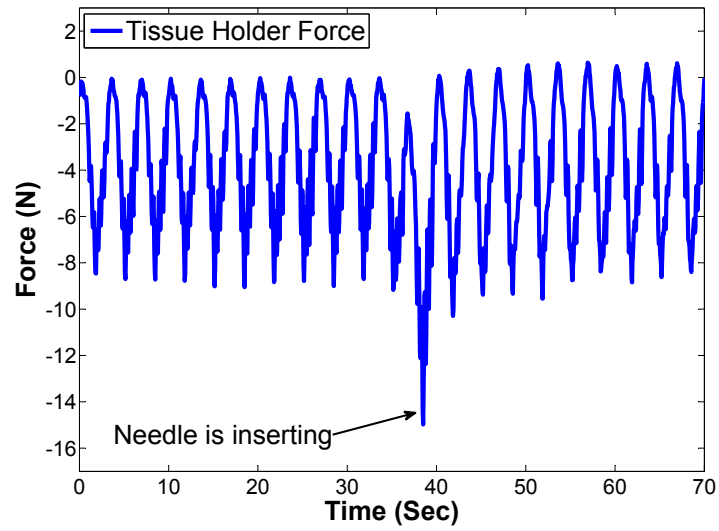
As can be seen in Fig. 2.12, during the first phase (0–37 s), the needle tracks the motion of the contact point. During the second phase, the operator moves the master device and as a result, the needle tracks a modulated motion while harmonizing with the tissue to keep the relative distance stable. Considering (2.10), the Theoretical Performance Measure (TPM) of the system can be derived as:

$$\begin{aligned}
 e(t) &= \mathcal{L}^{-1} \{X_1(s) - X_3(s)\} \\
 &= \mathcal{L}^{-1} \left\{ \frac{\alpha(s)}{1 + \alpha(s) + \Delta_1(s) + \Delta_2(s)Z_2^{-1}(s)} X_1(s) \right\}, \quad (2.12)
 \end{aligned}$$

where  $e(t)$  and  $\mathcal{L}^{-1}$  are the TPM in the time domain and the inverse Laplace operator,



(a)



(b)

Figure 2.12: The system performance, (a) needle position versus tissue position, (b) force applied on tissue holder.

respectively. Lower values of the TPM result in higher accuracy of the system. For negligible uncertainties  $\Delta_1(s)$  and  $\Delta_2(s)$ , the TPM becomes:

$$e(t) |_{\Delta_1, \Delta_2 \rightarrow 0} = \mathcal{L}^{-1} \left\{ \frac{\alpha(s)}{1 + \alpha(s)} X_1(s) \right\}, \quad (2.13)$$

In Fig. 2.13, both the experimental and the theoretical performance measures are shown. Comparing these two signals, an acceptable agreement can be observed between them ( $-0.0954$  mm of the mean difference value with a standard deviation of  $0.6735$  mm). Although both signals show about  $\pm 3.5$  mm error in tissue motion compensation, the error can be alleviated for clinical applications by considering that the theoretical performance measure of the system is a function of the designed  $\alpha(s)$  and the level of uncertainties, as can be seen from (2.12). In order to enhance the tracking performance, an optimal  $\alpha(s)$  should be designed to both satisfy the stability criterion, (2.11), and minimize the TPM, (2.13). The latter can be reduced by using:

- better pressure sensors with better signal-to-noise ratio, lower drift and higher repeatability,
- more accurate identification, and
- a higher order  $\alpha(s)$ .

From the results obtained, it can be said that the operator can target specific depths inside the tissue almost independently from tissue movement. The results indicate that due to the proposed impedance controller, the clinician would feel as if he/she is performing stable insertion into stationary tissue.

## 2.5 Conclusions and Future Work

A mechatronic solution was proposed in this paper for undesirable modulated motion of soft tissue during needle insertion in the lung. The proposed robotic solution, which is called “Macro–Micro insertion”, is designed to compensate for the tissue motion, based on the contact pressure and thereby increase targeting accuracy. The impedance control strategy was analyzed as a proper control scheme for tracking tissue motion. The mechanical model and control synthesis were developed in order

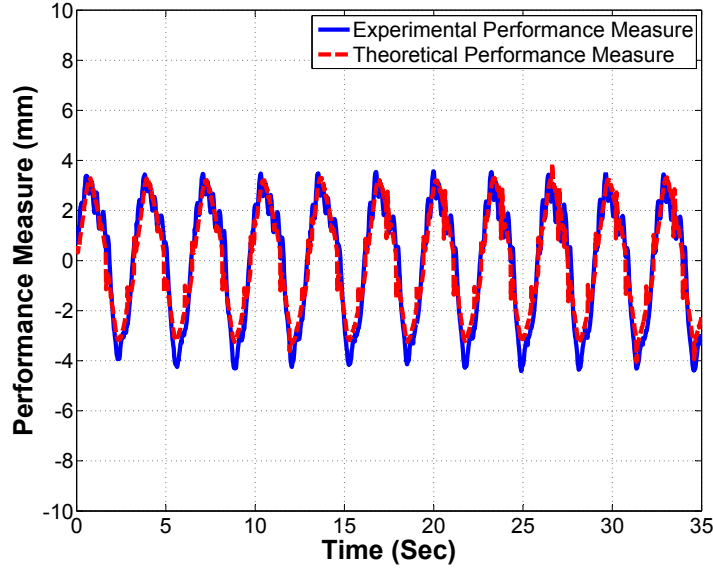


Figure 2.13: Comparison between the experimental and the theoretical performance measures.

to minimize the tissue deformation during needle insertion. The feasibility of the proposed approach was shown using an experimental setup consisting of two PA-10 Mitsubishi manipulators that were used for 1) manipulating the macro part based on the output of the impedance control strategy; and 2) mimicking the tissue motion behavior while holding the tissue. The needle driver was actuated using a linear stage and four resistive pressure sensors mounted at the tip of the macro robot measured the contact pressure. Our ongoing work focuses on miniaturization of the pressure sensors, 3-D motion compensation that takes into account the remote center of motion (RCM) constraint and the development of an appropriate port placement strategy.

## References

- [1] S. Xu, G. Fichtinger, R. H. Taylor, F. Banovac, and K. Cleary, “CT fluoroscopy-guided robotically-assisted lung biopsy,” in *Medical Imaging*. International Society for Optics and Photonics, 2006, pp. 61 411L–61 411L.
- [2] L. B. Kratchman, M. M. Rahman, J. R. Saunders, P. J. Swaney, and R. J. Webster III, “Toward robotic needle steering in lung biopsy: a tendon-actuated approach,” in *SPIE Medical Imaging*, International Society for Optics and Photonics, 2011, pp. 79 641I–79 641I.
- [3] L. Maier-Hein, A. Tekbas, A. Seitel, A. Franz, B. Radeleff, F. Pianka, S. Müller, S. Satz, R. Tetzlaff, I. Wolf *et al.*, “Computer-assisted needle insertion for abdominal interventions,” in *World Congress on Medical Physics and Biomedical Engineering, September 7-12, 2009, Munich, Germany*, Springer, 2009, pp. 159–162.
- [4] P. J. Keall, G. S. Mageras, J. M. Balter, R. S. Emery, K. M. Forster, S. B. Jiang, J. M. Kapatoes, D. A. Low, M. J. Murphy, B. R. Murray *et al.*, “The management of respiratory motion in radiation oncology report of aapm task group 76a),” *Medical Physics*, vol. 33, no. 10, pp. 3874–3900, 2006.
- [5] E. Yu, C. Lewis, A. L. Trejos, R. V. Patel, and R. A. Malthaner, “Lung cancer brachytherapy: robotics-assisted minimally invasive approach,” *Current Respiratory Medicine Reviews*, vol. 7, no. 5, pp. 340–353, 2011.
- [6] R. Richa, A. P. Bó, and P. Poignet, “Towards robust 3-D visual tracking for motion compensation in beating heart surgery,” *Medical Image Analysis*, vol. 15, no. 3, pp. 302–315, 2011.

- [7] R. Richa, P. Poignet, and C. Liu, “Three-dimensional motion tracking for beating heart surgery using a thin-plate spline deformable model,” *The International Journal of Robotics Research*, vol. 29, no. 2-3, pp. 218–230, 2010.
- [8] S. G. Yuen, S. B. Kesner, N. V. Vasilyev, P. J. Del Nido, and R. D. Howe, “3-D ultrasound-guided motion compensation system for beating heart mitral valve repair,” in *Medical Image Computing and Computer-Assisted Intervention (MICCAI)*, Springer, 2008, pp. 711–719.
- [9] S. G. Yuen, D. T. Kettler, P. M. Novotny, R. D. Plowes, and R. D. Howe, “Robotic motion compensation for beating heart intracardiac surgery,” *The International Journal of Robotics Research*, vol. 28, no. 10, pp. 1355–1372, 2009.
- [10] A. Sadeghi Naini, R. V. Patel, and A. Samani, “CT-enhanced ultrasound image of a totally deflated lung for image-guided minimally invasive tumor ablative procedures,” *IEEE Transactions on Biomedical Engineering*, vol. 57, no. 10, pp. 2627–2630, 2010.
- [11] O. Bebek and M. C. Cavusoglu, “Intelligent control algorithms for robotic-assisted beating heart surgery,” *IEEE Transactions on Robotics*, vol. 23, no. 3, pp. 468–480, 2007.
- [12] S. G. Yuen, M. C. Yip, N. V. Vasilyev, D. P. Perrin, J. Pedro, and R. D. Howe, “Robotic force stabilization for beating heart intracardiac surgery,” in *Medical Image Computing and Computer-Assisted Intervention (MICCAI)*, Springer, 2009, pp. 26–33.
- [13] M. Dominici, P. Poignet, R. Cortesão, E. Dombre, and O. Tempier, “Compensation for 3-D physiological motion in robotic-assisted surgery using a predictive force controller: experimental results,” in *IEEE/RSJ International Conference on Intelligent Robots and Systems (IROS)*, IEEE, 2009, pp. 2634–2639.
- [14] B. Cagneau, N. Zemiti, D. Bellot, and G. Morel, “Physiological motion compensation in robotized surgery using force feedback control,” in *IEEE International Conference on Robotics and Automation (ICRA)*, IEEE, 2007, pp. 1881–1886.



- [15] J. M. Florez, D. Bellot, and G. Morel, “LWPR-model based predictive force control for serial comanipulation in beating heart surgery,” in *IEEE/ASME International Conference on Advanced Intelligent Mechatronics (AIM)*, IEEE, 2011, pp. 320–326.
- [16] S. G. Yuen, D. P. Perrin, N. V. Vasilyev, P. J. del Nido, and R. D. Howe, “Force tracking with feed-forward motion estimation for beating heart surgery,” *IEEE Transactions on Robotics*, vol. 26, no. 5, pp. 888–896, 2010.
- [17] W. Bachta, P. Renaud, E. Laroche, A. Forgione, and J. Gangloff, “Active stabilization for robotized beating heart surgery,” *IEEE Transactions on Robotics*, vol. 27, no. 4, pp. 757–768, 2011.
- [18] Y. Fung, *Biomechanics: mechanical properties of living tissues*, Springer-Verlag, New York, 1993.
- [19] K. Hashtrudi-Zaad and S. E. Salcudean, “Transparency in time-delayed systems and the effect of local force feedback for transparent teleoperation,” *IEEE Transactions on Robotics and Automation*, vol. 18, no. 1, pp. 108–114, 2002.
- [20] A. Talasaz, “Haptics-enabled teleoperation for robotics-assisted minimally invasive surgery,” Ph.D. dissertation, University of Western Ontario, 2012.

## Chapter 3

# Vibration-Assisted Needle Insertion

### 3.1 Introduction

The use of flexible needles in percutaneous interventions such as biopsy, drug delivery, brachytherapy, neurosurgery and tumor ablation has attracted many researchers. Particularly when target points are not directly accessible inside soft tissue, this type of intervention is more appealing. Needle tip misplacement can, however, degrade the effectiveness of the therapy or diagnosis. In this context, robotics-assisted needle intervention has been proposed as a solution to enhance targeting accuracy [1]. Nonetheless, targeting inaccuracies still occur due to effects such as (1) target movement as a result of soft tissue deformation, (2) needle bending due to the complex nature of needle–tissue interaction, and (3) inhomogeneity and anisotropy of real organic tissue [2].

In order to increase targeting accuracy, the complex interaction between the needle and soft tissue has to be fully investigated. Okamura et al. [3] were the first to define needle insertion as a three-phase procedure, namely pre-puncture, post-puncture and retraction or needle withdrawal. While viscoelastic behavior dominates the pre-puncture phase, the combined effects of cutting force, friction and tissue relaxation govern the post-puncture step. As an analytical study in this area, Mahvash and Dupont [4] proposed a fast needle insertion technique as a means of decreasing pre-puncture force and needle deflection, thereby improving positioning accuracy. They

---

This chapter contains material published in Iman Khalaji, Mostafa Hadavand, Ali Asadian, Rajni V. Patel, and Michael D. Naish, “Analysis of needle-tissue friction during vibration-assisted needle insertion,” in *Proceedings of IEEE/RSJ International Conference on Intelligent Robots and Systems (IROS)*, 2013, pp. 4099–4104.

considered the role of insertion rate and linked it to the interaction forces. Nevertheless, the safety of such a “needle shooting” procedure for living tissue particularly at close proximity to vital organs such as the heart and lungs is questionable.

As a major force component in needle–tissue interaction, translational friction deserves further study. It is believed that by controlling or at least minimizing frictional effects, soft tissue deformation can be significantly reduced, which in turn would result in better targeting accuracy for needle-based interventional procedures. This idea is the main motivation for the current study.

## 3.2 Related Work

Velocity modulation during needle insertion is an approach that has been proposed in research papers in order to guide a flexible needle or minimize tissue deformation [5]. In the context of control, Minhas et al. [6] developed a duty-cycled spinning technique to adjust the needle trajectory and steer it into soft tissue. From force analysis perspective, high-frequency translational oscillation and rotational drilling were reported to reduce needle–tissue interaction forces as well as tissue deformation [7, 8]. Likewise, reduced tissue indentation and frictional forces were reported in [9] when using a low frequency rotational motion. Nonetheless, needle spinning may induce tissue damage due to any minor defect in needle straightness, off-centric rotation or macro-structural defects at the needle tip as a result of imperfect machining. In order to address this issue, post-revolving the needle was shown to have the same benefit and to reduce targeting error [10].

Shin-ei et al. [11] were the first to report a reduction in needle insertion force by inducing mechanical vibration into a hypodermic needle. Using multilayer piezoelectric elements, the needle, which was forced to vibrate laterally in the frequency range up to 10 kHz, was inserted into swine muscle tissue. A maximum reduction of 69% in interaction force was reported in their work [11]. However, it is unclear what vibration amplitude and insertion velocity were used to conduct the experiments. Muralidharan [12] also investigated the effect of longitudinal vibration in terms of its amplitude and frequency on the penetration force (in both soft tissue and tissue sur-

rogate) using a permanent magnet shaker. The reported results support a reduction in the penetration force of 2 to 3 times when using a higher vibration amplitude and frequency. However, no statistical interaction analysis was provided in this study.

Inspired by motions during a mosquito bite, it is believed that vibration-assisted needle insertion minimizes pain [12]. If true, this technique can potentially enhance needle-based interventions such as bone biopsy [13] by lowering interaction forces and increasing accuracy. In the current study, a mathematical analysis is performed to justify why in general during vibration-assisted needle insertion, the friction force is reduced. The presented model, which exploits the LuGre friction model [14], establishes an explicit relationship between the vibration parameters including motion amplitude and frequency and the force magnitude. Moreover, experiments performed on soft tissue samples serve to validate the model.

The rest of this paper is organized as follows. Section III explains the role of vibration on frictional effects using the LuGre model. Section IV describes the experimental evaluation while Section V presents conclusions and suggestions for future work.

### 3.3 Mathematical Analysis of Needle–Tissue Friction Using Vibration

Asadian et al. [15] developed a distributed version of the LuGre friction model [14] along the inserted portion of a needle to model friction effects during needle insertion. This physically-inspired model is based on the bending of spring-like bristle elements that exist at the microscopic level of moving surfaces. As a basis for the current analysis, the LuGre structure [15] is briefly reviewed here.

Considering  $z(\zeta, t)$  as the model's internal state or the deflection of the bristle elements located at the point  $\zeta$  at a certain time  $t$ , the distributed LuGre model can be written as [14, 15]:

$$\begin{cases} \frac{dz}{dt}(\zeta, t) = v - \frac{\sigma_0 |v|}{g(v)} z \\ F_{\text{friction}}(t) = \int_0^{L(t)} dF(\zeta, t) \end{cases} \quad (3.1)$$

$$g(v) = \mu_c + (\mu_s - \mu_c)e^{-\alpha|v|}, \quad (3.2)$$

where  $v$  is the velocity of each differential element and  $L(t)$  is the needle length that is being inserted into soft tissue at time  $t$ . Moreover,

$$dF(\zeta, t) = \left( \sigma_0 z(\zeta, t) + \sigma_1 \frac{\partial z}{\partial t}(\zeta, t) + \sigma_2 v \right) dF_n(\zeta, t), \quad (3.3)$$

is the differential friction force that is proportional to the differential normal force,  $dF_n(\zeta, t)$  applied to the element  $d\zeta$  at time  $t$ . In total, the friction force can be characterized by four static parameters, i.e.,  $\mu_c$ ,  $\mu_s$ ,  $\sigma_2$  and  $\alpha$ , as well as two dynamic parameters, namely  $\sigma_0$  and  $\sigma_1$ . As can be seen in Fig. 1,  $\sigma_0$  and  $\sigma_1$  can be understood as the stiffness and damping coefficients of the microscopic elastic bristles, whereas  $\sigma_2$ ,  $\mu_c$  and  $\mu_s$  are the viscous damping, normalized Coulomb and stiction friction coefficients [15].

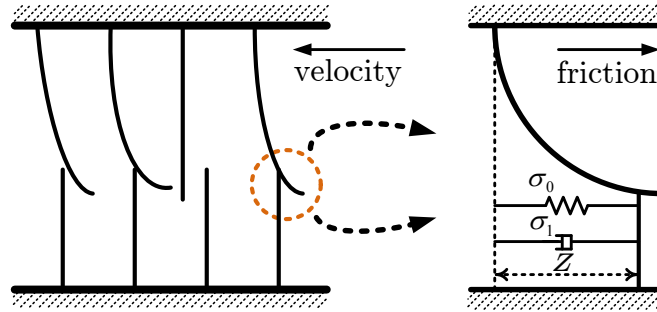


Figure 3.1: Microscopic representation of irregular contact surfaces and elastic bristles whose bending gives rise to the friction force (Reproduced from [15], © Copyright IEEE, 2011).

Assuming a uniform normal force distribution along the needle and a constant patch region of needle within soft tissue, i.e.,  $\frac{dL}{dt} = 0$ , (3.1) can be simplified to [15]:

$$\begin{cases} \dot{\tilde{z}} = v - \frac{\sigma_0|v|}{g(v)}\tilde{z} \\ F_{\text{friction}}(t) = F_n (\sigma_0\tilde{z} + \sigma_1\dot{\tilde{z}} + \sigma_2v) \end{cases}, \quad (3.4)$$

where  $\tilde{z}$  is the mean friction state. Note that in the above state-space representation, all static and dynamic parameters are functions of the interaction characteristics and

are independent of the insertion rate\*.

Assuming a zero initial condition, i.e.,  $\tilde{z}(0) = 0$ , the general solution of the ordinary differential equation described in (3.4) is of the form:

$$\tilde{z}(t) = \frac{g(v(t))}{\sigma_0} \text{sgn}(v(t)) \left( 1 - e^{-\sigma_0 \int_0^t \frac{|v(t)|}{g(v(t))} dt} \right). \quad (3.5)$$

### 3.3.1 Needle Insertion at Constant Velocity

Now consider a situation where a constant length of a needle has been inserted into a block of soft tissue, while its tip is outside the other side of the block. While the needle is being advanced toward soft tissue with a constant velocity, i.e.,  $v(t) = v_0$ , a constant length of the needle maintains contact with soft tissue. Therefore, (3.5) can be further simplified as:

$$\tilde{z}(t) = \frac{g(v_0)}{\sigma_0} \text{sgn}(v_0) \left( 1 - e^{-\frac{\sigma_0}{g(v_0)} |v_0| t} \right). \quad (3.6)$$

Inserting (3.6) into (3.4), the total friction force can be obtained as:

$$\begin{aligned} F_{\text{friction}}(t) = F_n \{ (\sigma_1 v_0 - g(v_0) \text{sgn}(v_0)) e^{-\frac{\sigma_0}{g(v_0)} |v_0| t} \\ + g(v_0) \text{sgn}(v_0) + \sigma_2 v_0 \}. \end{aligned} \quad (3.7)$$

Hence, the steady-state friction force for sufficiently large values of  $v_0$  is:

$$F_{\text{friction,ss}} = F_n \{ \mu_c + \sigma_2 v_0 \}. \quad (3.8)$$

Referring to (3.8), for sufficiently large values of time,  $t$ , viscosity and Coulomb friction are the only components that constitute the friction force. Moreover, increasing the insertion rate makes the total friction force bigger due to the viscous term. Roughly speaking, at very high velocities, viscosity totally dominates the Coulomb

---

\* In general,  $\sigma_2$  is a function of  $v$  and decreases as the velocity increases. However, in this section,  $\sigma_2$  is assumed to be constant.

friction term.

### 3.3.2 Vibration-Assisted Needle Insertion

Now, suppose that a needle is vibrated longitudinally while it is being inserted into soft tissue. Investigation of the effect of such velocity modulation on the friction force is described in this section. While a few researchers have reported a reduction in the friction force due to a modulated velocity [7], to the best of the authors' knowledge, no one has ever systematically studied the effect of vibration and velocity modulation on the friction force.

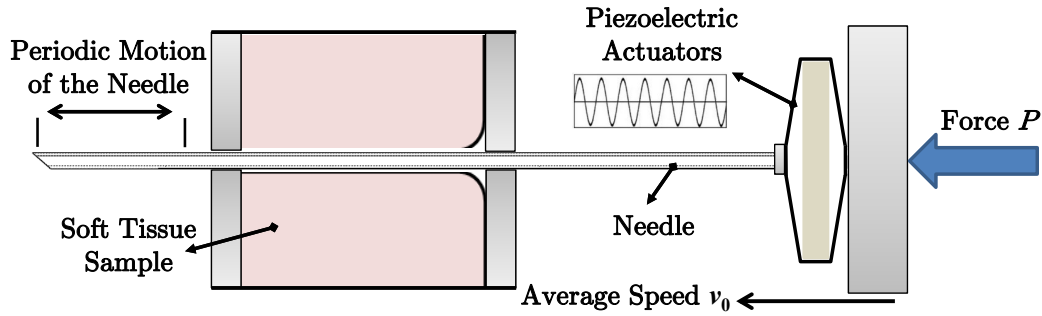


Figure 3.2: Schematic demonstration of the proposed needle insertion setup.

As illustrated in Fig. 3.2, suppose that a vibration generator has been attached to the distal end of a needle. The generator applies a longitudinal sinusoidal force to the needle structure. In order to perform an insertion procedure, the whole unit, including the needle and the vibration generator, is moved with an average speed  $v_0$ . Also, assume that the unit is subject to a static force  $P$ . Without loss of generality, consider the following functional form for the insertion velocity<sup>†</sup>:

$$v(t) = v_0 + a\omega \cos(\omega t), \quad (3.9)$$

---

<sup>†</sup> Since needle is a long hollow tube, its first few lateral natural frequencies are much smaller than the first longitudinal resonance frequency. It can be assumed that the vibration source will not excite the needle near its natural frequencies to avoid lateral resonance. Lateral resonance can also be avoided by imposing one or two lateral nodes along the vibrating needle.

where  $a$  and  $\omega$  are the amplitude and frequency of vibration. By substitution of (3.9) into (3.5), the mean friction state can be obtained as:

$$\tilde{z}(t) = \frac{g(v_0 + a\omega \cos(\omega t))}{\sigma_0} \text{sgn}(v_0 + a\omega \cos(\omega t)) \times \left( 1 - e^{-\sigma_0 \int_0^t \frac{|v_0 + a\omega \cos(\omega t)|}{g(v_0 + a\omega \cos(\omega t))} dt} \right). \quad (3.10)$$

Let us define  $u(t) = \int_0^t \frac{|v(t)|}{g(v(t))} dt$ . For sufficiently large values of time  $t$ ,  $u$  becomes very large since it is a nondecreasing function with respect to time, i.e.,  $u'(t) = \frac{|v(t)|}{g(v(t))} \geq 0$ . Therefore, the mean deflection state in (3.10) becomes:

$$\tilde{z}(t) = \frac{g(v_0 + a\omega \cos(\omega t))}{\sigma_0} \text{sgn}(v_0 + a\omega \cos(\omega t)). \quad (3.11)$$

Using (3.11) in (3.4), the instantaneous friction force can then be approximated as a function of  $v(t)$ . Due to the periodic nature of the insertion profile,  $F_{\text{friction}}(t)$  is, in fact, a periodic function with a period of  $T = 2\pi/\omega$ . Considering this fact, and using the theory of momentum [16], the constant force  $P$  can be expressed as:

$$P = \frac{1}{T} \int_{t_1}^{t_1+T} F_{\text{friction}}(t) dt. \quad (3.12)$$

Therefore, considering (3.12) and (3.4), we have

$$\begin{aligned} P &= \frac{1}{T} \int_{t_1}^{t_1+T} F_n (\sigma_0 \tilde{z} + \sigma_1 \dot{\tilde{z}} + \sigma_2 v) dt \\ &= \frac{F_n}{T} \left( \underbrace{\sigma_0 \int_{t_1}^{t_1+T} \tilde{z} dt}_{\text{I}} + \underbrace{\sigma_1 \int_{t_1}^{t_1+T} \dot{\tilde{z}} dt}_{\text{II}} + \underbrace{\sigma_2 \int_{t_1}^{t_1+T} v dt}_{\text{III}} \right), \end{aligned} \quad (3.13)$$



where  $\tilde{z}$  is obtained from (3.11).

The third integral (III) in (3.13) can be rewritten as:

$$\int_{t_1}^{t_1+T} v dt = \int_{t_1}^{t_1+T} (v_0 + a\omega \cos(\omega t)) dt = v_0 T. \quad (3.14)$$

In order to obtain the second integral (II) in (3.13), (3.11) is used to rewrite the integrand,  $\dot{\tilde{z}}$ :

$$\dot{\tilde{z}} = \frac{1}{\sigma_0} \frac{\partial g(v)}{\partial v} v'(t) \text{sgn}(v(t)) = \frac{-\alpha(\mu_s - \mu_c)}{\sigma_0} v'(t) e^{-\alpha|v(t)|}. \quad (3.15)$$

According to (3.15),  $\dot{\tilde{z}}$  is a continuous function over  $[t_1, t_1 + T]$ , thus:

$$\int_{t_1}^{t_1+T} \dot{\tilde{z}} dt = \tilde{z}(t_1 + T) - \tilde{z}(t_1) = 0. \quad (3.16)$$

Note that to derive (3.16), the periodicity of  $\tilde{z}$  with period  $T$  is taken into account.

Using (3.11), the first integral (I) in (3.13) can be simplified as:

$$\begin{aligned} \int_{t_1}^{t_1+T} \tilde{z} dt &= \int_{t_1}^{t_1+T} \frac{g(v(t))}{\sigma_0} \text{sgn}(v(t)) dt \\ &= \frac{\mu_c}{\sigma_0} \int_{t_1}^{t_1+T} \text{sgn}(v_0 + a\omega \cos(\omega t)) dt \\ &\quad + \frac{\mu_s - \mu_c}{\sigma_0} \int_{t_1}^{t_1+T} e^{-\alpha|v_0 + a\omega \cos(\omega t)|} \text{sgn}(v_0 + a\omega \cos \omega t) dt. \end{aligned} \quad (3.17)$$

In order to simplify (3.17), let us assume two special cases:

- If  $|v_0| > a\omega$ ,  $v(t) = v_0 + a\omega \cos(\omega t)$  will be a single-sign function (either positive

or negative) and therefore, (3.17) can be obtained as:

$$\int_{t_1}^{t_1+T} \tilde{z} dt = \frac{T}{\sigma_0} \{ \mu_c + (\mu_s - \mu_c) e^{-\alpha|v_0|} I_0(\alpha a \omega) \} \times \text{sgn}(v_0), \quad (3.18)$$

where  $I_0(x)$  is the modified Bessel function of the first kind and zero order at  $x$ . Note that,  $I_0(x) \geq 1$  for  $\forall x$ .

- If  $|v_0| < a\omega$ , after a few manipulations, (3.17) can be simplified as:

$$\begin{aligned} \int_{t_1}^{t_1+T} \tilde{z} dt &= \frac{\mu_c}{\sigma_0} \int_{t_1}^{t_1+T} \text{sgn}(v(t)) dt + \text{sgn}(v_0) \frac{\mu_s - \mu_c}{\sigma_0} \\ &\times \left( \int_{t_1}^{t_1+T} e^{\frac{-\alpha v(t)}{\text{sgn}(v_0)}} dt - 2 \int_{t_1+t_1^*}^{t_1+t_2^*} \cosh(\alpha v(t)) dt \right), \end{aligned} \quad (3.19)$$

where  $t_1^*$  and  $t_2^*$  denotes the moments when the insertion velocity,  $v(t)$ , changes its sign:

$$\begin{aligned} \tau_1 &= \omega t_1^* = \arccos\left(-\frac{v_0}{a\omega}\right) = \frac{\pi}{2} + \arcsin\left(\frac{v_0}{a\omega}\right) \\ \tau_2 &= \omega t_2^* = 2\pi - \tau_1. \end{aligned} \quad (3.20)$$

Considering (3.20), (3.19) can be further simplified as:

$$\begin{aligned} \int_{t_1}^{t_1+T} \tilde{z} dt &= \frac{T}{\sigma_0} \text{sgn}(v_0) \left\{ \frac{2\mu_c}{\pi} \arcsin\left(\frac{v_0}{a\omega}\right) + (\mu_s - \mu_c) \right. \\ &\times [e^{-\alpha|v_0|} I_0(\alpha a \omega) \\ &\left. - \frac{\pi}{\omega} \int_{t_1+t_1^*}^{t_1+t_2^*} \cosh(\alpha v_0 + \alpha a \omega \cos(\omega t)) dt \right\}. \end{aligned} \quad (3.21)$$

Finally, using (3.16), (3.14), (3.18) and (3.21), the total friction force  $P$  in (3.13) is specified as follows:

- For  $|v_0| > a\omega$ , the total force becomes:

$$P = \overbrace{F_n \{ \mu_c + (\mu_s - \mu_c) e^{-\alpha|v_0|} I_0(\alpha a \omega) \}}^{P_{\text{Coulomb}}} \times \text{sgn}(v_0) + F_n \sigma_2 v_0. \quad (3.22)$$

- When  $|v_0| < a\omega$ ,  $P$  can be obtained as:

$$P = F_n \text{sgn}(v_0) \left\{ \frac{2\mu_c}{\pi} \arcsin\left(\frac{v_0}{a\omega}\right) + (\mu_s - \mu_c) \times [e^{-\alpha|v_0|} I_0(\alpha a \omega) - \frac{\pi}{\omega} \int_{t_1+t_1^*}^{t_1+t_2^*} \cosh(\alpha v_0 + \alpha a \omega \cos(\omega t)) dt] \right\} + F_n \sigma_2 v_0. \quad (3.23)$$

Comparing (3.22) and (3.23) with (3.8), it is obvious that the viscous component of the total friction force, i.e.,  $F_n \sigma_2 v_0$ , remains intact, even in the presence of vibration. The Coulomb friction force, however, changes as a vibrating needle is inserted into tissue. The dependence of the normalized static force required for the Coulomb portion,  $P_{\text{Coulomb}}$ , on the ratio of speeds,  $\frac{v_0}{a\omega}$  is shown in Fig. 3.3. To obtain such a curve,  $\mu_s$  is assumed to be an order of magnitude larger than  $\mu_c$ . As seen in this graph, vibration reduces the static force required to counteract Coulomb friction when  $|v_0| < a\omega$ . For very small  $v_0$  values or very large vibration speeds, i.e.,  $a\omega \gg |v_0|$ , (3.23) gives:

$$P = F_n \left( \frac{2\mu_c}{\pi a \omega} + \sigma_2 \right) v_0. \quad (3.24)$$

Equation (3.24) shows how vibration-assisted insertion drives the behavior of the medium from Coulomb/viscous friction into a pure linear viscous friction with a much lower friction coefficient.

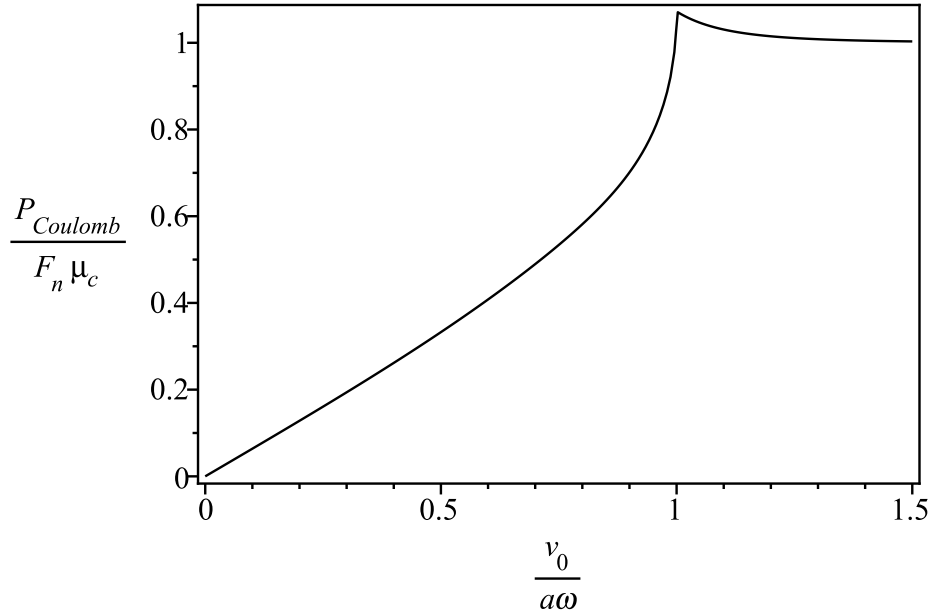


Figure 3.3: Mathematical dependency of the normalized Coulomb friction force on  $\frac{v_0}{a\omega}$  during vibration-assisted needle insertion.

## 3.4 Instrumentation and Experimental Evaluation

### 3.4.1 Experimental Setup

Experimental evaluation of the effect of vibration on needle–tissue friction was carried out using the setup shown in Fig. 3.4, where a vibrating needle is inserted into a soft tissue specimen using a linear motor at various speeds. The interaction forces between the needle and the tissue sample were then transferred to a desktop PC for further analysis.

The tissue sample holder was manufactured using a rapid prototyping machine and had removable side walls to facilitate needle insertion. The holder was attached to a Nano43 6-DOF force/torque sensor (ATI Industrial Automation) in order to measure the interaction forces. Two Amplified Piezoelectric Actuators (APA60SM<sup>®</sup>, Cedrat Technologies), which were aligned side-by-side on a heavy stainless steel disk base, were employed as the vibration source unit. A 7075-T6 aluminum bar was micro-machined to attach an 18 GA stainless steel brachytherapy needle (Cook Medical)

to the driving actuators (see Fig. 4). The actuator unit was subsequently mounted on top of a T-LSR300B motorized linear stage (Zaber Technologies) using another rapid-prototyped adapter. A dual-channel AFG 3022B arbitrary function generator (Tektronix) was then employed to generate sinusoidal signals whose amplitudes and frequencies were precisely controlled by the operator through a desktop computer. The generated signals were amplified using an LE 150/200-2 dual-channel analogue high-power amplifier (Piezomechanik GmbH), and were fed into the two piezoelectric actuators to drive the needle and its attachments at the desired amplitude and frequency.

### 3.4.2 Experiment Design

In order to assess the validity of the current analysis, an experiment was designed to measure the friction force while a constant length of the needle was inserted into a tissue sample. A stack of two-layer fresh chicken breast clamped on the holder was employed as the sample. In order to eliminate the effect of variable soft tissue thickness at various insertion locations, a preliminary insertion was made without vibration. The same hole was then used to investigate frictional effects during five consecutive insertions with various vibration frequencies. To collect each data set, the following insertion-retraction procedure was carried out:

1. The needle was inserted into soft tissue at a constant velocity,  $v_0$ , with no vibration.
2. Once the needle had penetrated right through the sample, it was stopped for 30 seconds while vibration at a certain frequency and amplitude was started in the actuator unit.
3. The vibrating needle was advanced 6 cm into the tissue at velocity  $v_0$ .
4. The vibrating needle was retracted 6 cm from the tissue at velocity  $v_0$ .
5. The vibrating needle was again advanced 6 cm at velocity  $v_0$ .
6. The vibrating needle was completely retracted from the tissue at velocity  $v_0$ .

Following this procedure, the role of tissue pre-puncture and cutting forces during needle insertion can be assumed to have been eliminated. Therefore, it is safe to

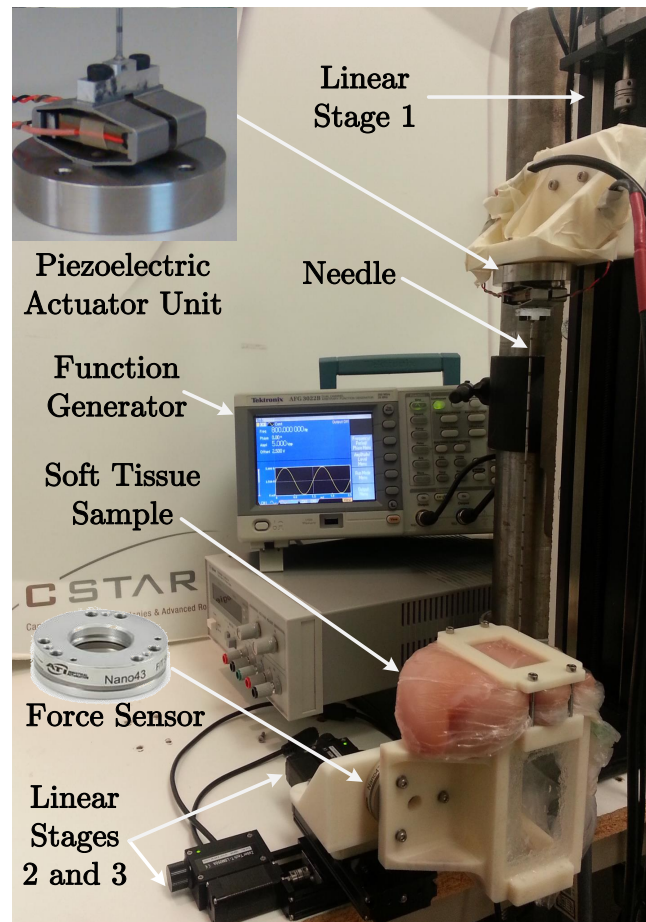


Figure 3.4: Two APA60SM piezoelectric actuators were mounted on a heavy stainless steel base. An 18 GA brachytherapy needle, glued to an aluminum link bar, was vibrated longitudinally using the actuators. Linear Stage 1 performs needle insertion, while the other two linear stages facilitate tissue motion for multiple needle insertions at various locations.

assume that friction and tissue relaxation were dominant in the resulting interaction forces.

### 3.4.3 Experimental Results

Twenty four sets of needle insertion experiments were performed on fresh chicken breast pieces using various vibration frequencies as well as insertion velocities. Tests were also performed with no vibration of the needle. Figs. 3.5–3.8 show the results of insertion at two different velocities, i.e.,  $v_0 = 5$  mm/sec and 10 mm/sec, into four adjacent insertion sites. The periodic insertion-retraction motion of the needle inside soft tissue can be observed as four distinct regions in the figures where the interaction forces remain almost constant until the direction of needle motion changes. As may be observed in the plots, the level of interaction force is higher for nonvibrating needle insertion, whereas it reduces as the frequency of vibration increases.

While no vibration sensor was used to measure the micron-scale vibration of the needle during the procedure, the driving voltage of the piezoelectric actuators was utilized as the determining factor to determine the vibration amplitude,  $a$ . In fact, it was assumed that both actuators produced similar vibration amplitude; hence, no nonlinear vibration mode was considered in actuating the needle. In an attempt to replicate Fig. 3.3 from the experimental results, the mean force values of the obtained results during insertion-retraction (Figs. 3.5–3.8), were calculated and paired with the corresponding values of  $\frac{v_0}{a\omega}$  for each needle insertion procedure. The results shown in Fig. 3.9 indicate a good agreement between the experiments and the theoretical approach. Slight scattering of the data in this figure could be due to the fact that the needle was inserted in various sites in tissue sample, where the needle length and soft tissue properties were not identical throughout the experiments. On the other hand, inhomogeneity, nonlinear viscoelasticity, and anisotropy of chicken breast may be another reason why our empirical observations plotted in Fig. 3.9 do not exactly follow the expected theoretical graph shown in Fig. 3.3.

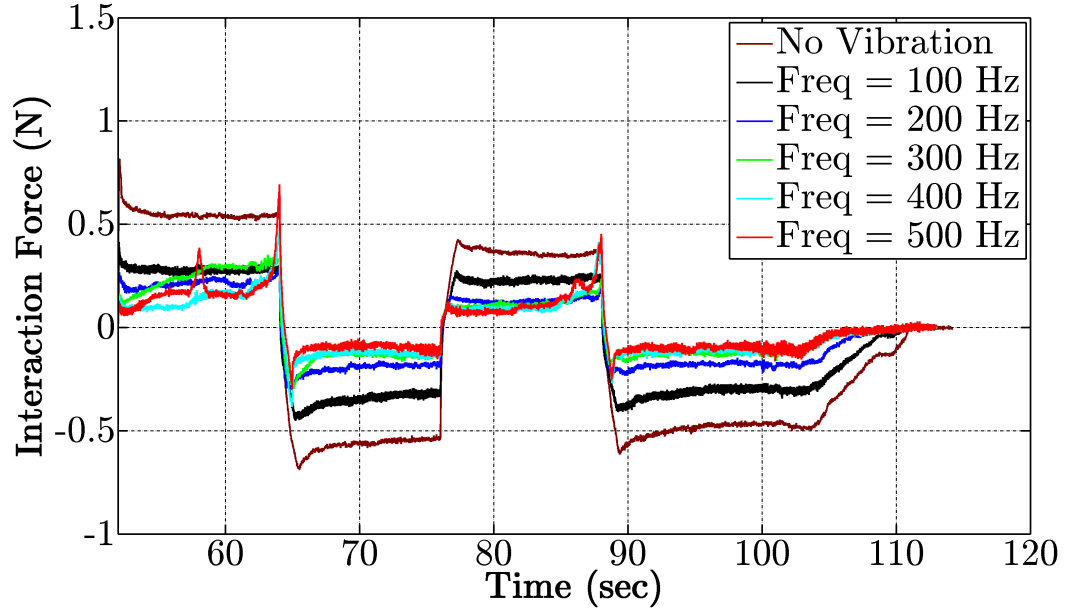


Figure 3.5: Measured force values during needle insertion at various frequencies (constant insertion velocity  $v_0 = 5$  mm/sec, vibration amplitude =  $30 \mu\text{m}$  p-p).

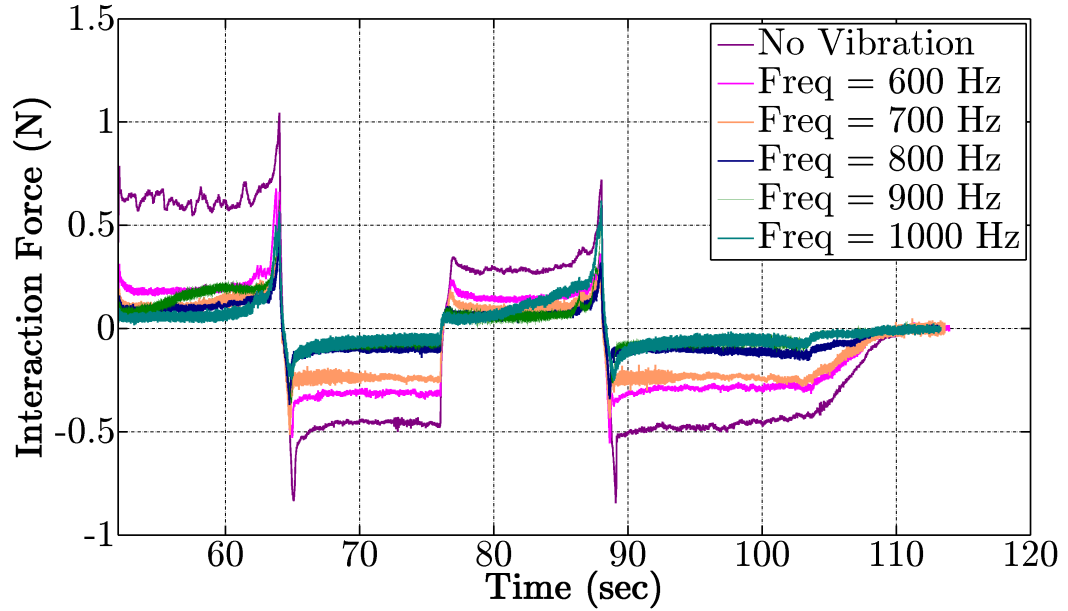


Figure 3.6: Measured force values during needle insertion at various frequencies (constant insertion velocity  $v_0 = 5$  mm/sec, vibration amplitude =  $30 \mu\text{m}$  p-p).



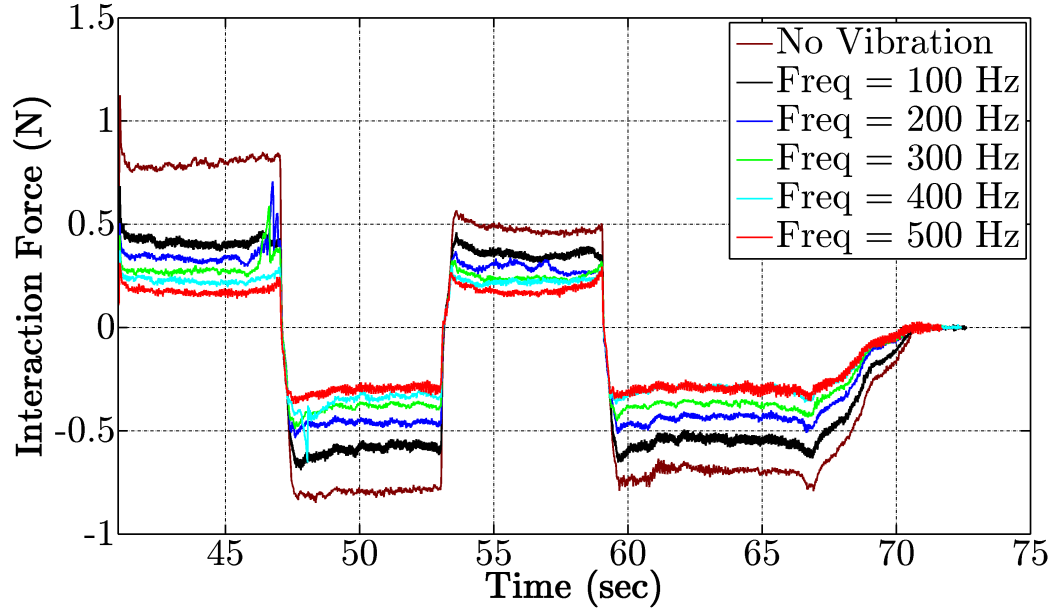


Figure 3.7: Measured force values during needle insertion at various frequencies (constant insertion velocity  $v_0 = 10$  mm/sec, vibration amplitude =  $30 \mu\text{m}$  p-p).

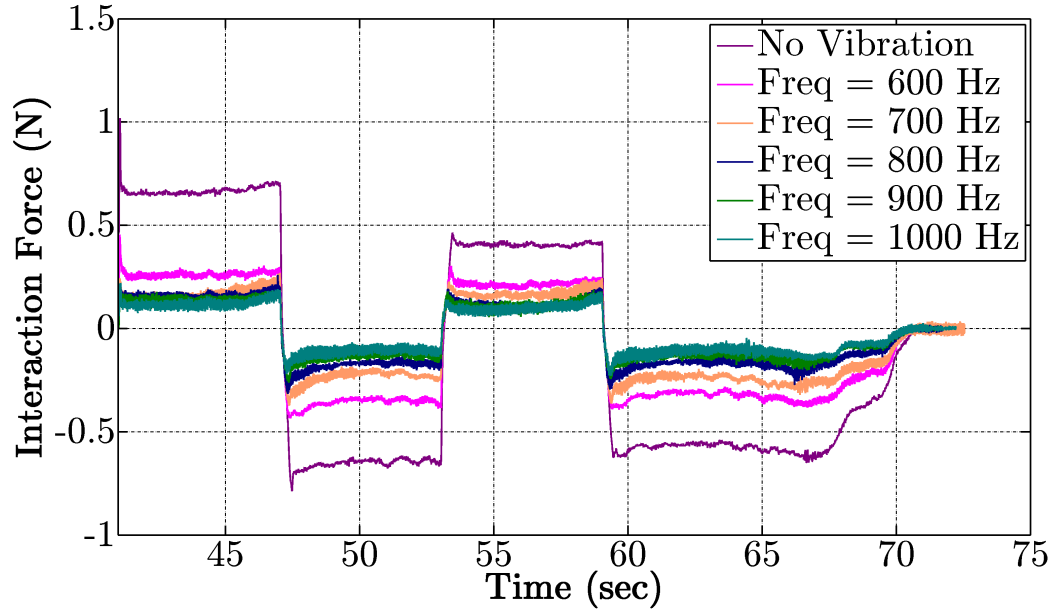


Figure 3.8: Measured force values during needle insertion at various frequencies (constant insertion velocity  $v_0 = 10$  mm/sec, vibration amplitude =  $30 \mu\text{m}$  p-p).

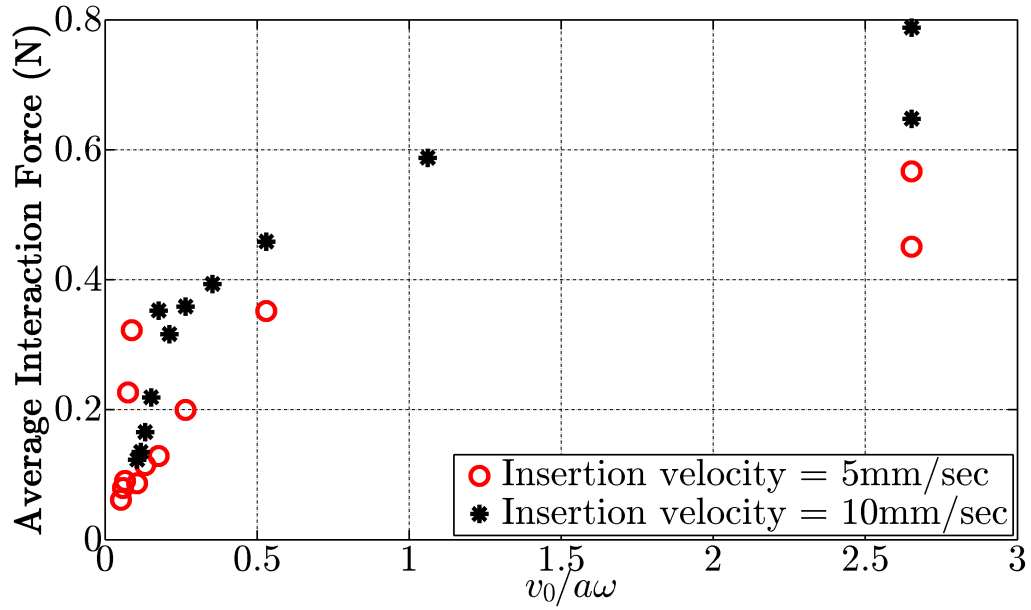


Figure 3.9: Force magnitude versus velocity ratio ( $\frac{v_0}{a\omega}$ ) of the vibrating needle.

### 3.5 Conclusions and Future Work

As is known, friction is a significant force component in needle–tissue interaction during percutaneous interventions. An analytical solution was presented to incorporate the impact of amplitude and frequency variation of a vibratory insertion profile on translational friction. The analysis was based on the LuGre friction model, which has been widely discussed in the literature. The experimental results illustrate that within a certain range of the amplitudes and frequencies, the theoretical model holds true. As observed, the total friction force drops as the frequency of the vibration increases relative to the insertion velocity. By minimizing frictional effects, soft tissue deformation is reduced. Thus, vibration-assisted needle insertion is expected to improve targeting accuracy. However, in order to generalize the proposed technique, it is required to examine a wider range of vibration frequencies and amplitudes.

Possible future extension includes investigating other types of *ex-vivo* soft tissue samples, e.g., liver, lung and bone. It is anticipated that the proposed technique will be particularly useful in bone biopsy where the dominant resistive force factor is Coulomb friction.

## References

- [1] N. Abolhassani, R. Patel, and M. Moallem, “Needle insertion into soft tissue: A survey,” *Medical Engineering & Physics*, vol. 29, no. 4, pp. 413–431, 2007.
- [2] A. Asadian, M. R. Kermani, and R. V. Patel, “A novel force modeling scheme for needle insertion using multiple kalman filters,” *IEEE Transactions on Instrumentation and Measurement*, vol. 61, no. 2, pp. 429–438, 2012.
- [3] A. M. Okamura, C. Simone, and M. D. O’Leary, “Force modeling for needle insertion into soft tissue,” *IEEE Transactions on Biomedical Engineering*, vol. 51, no. 10, pp. 1707–1716, 2004.
- [4] M. Mahvash and P. E. Dupont, “Fast needle insertion to minimize tissue deformation and damage,” in *IEEE International Conference on Robotics and Automation (ICRA)*, IEEE, 2009, pp. 3097–3102.
- [5] D. J. van Gerwen, J. Dankelman, and J. J. van den Dobbela, “Needle–tissue interaction forces—a survey of experimental data,” *Medical Engineering & Physics*, vol. 34, no. 6, pp. 665–680, 2012.
- [6] D. S. Minhas, J. A. Engh, M. M. Fenske, and C. N. Riviere, “Modeling of needle steering via duty-cycled spinning,” in *29th Annual International Conference of the IEEE Engineering in Medicine and Biology Society (IEEE-EMBS)*, IEEE, 2007, pp. 2756–2759.
- [7] T. Podder, D. Clark, D. Fuller, J. Sherman, W. Ng, L. Liao, D. Rubens, J. Strang, E. Messing, Y. Zhang *et al.*, “Effects of velocity modulation during surgical needle insertion,” in *27th Annual International Conference of the IEEE Engineering in Medicine and Biology Society (IEEE-EMBS)*, IEEE, 2005, pp. 5766–5770.

- [8] K. Yan, W. S. Ng, K. V. Ling, T.-I. Liu, Y. Yu, and T. Podder, “High frequency translational oscillation and rotational drilling of the needle in reducing target movement,” in *IEEE International Symposium on Computational Intelligence in Robotics and Automation (CIRA)*, IEEE, 2005, pp. 163–168.
- [9] N. Abolhassani, R. Patel, and M. Moallem, “Control of soft tissue deformation during robotic needle insertion,” *Minimally Invasive Therapy & Allied Technologies*, vol. 15, no. 3, pp. 165–176, 2006.
- [10] S. Badaan, D. Petrisor, C. Kim, P. Mozer, D. Mazilu, L. Gruionu, A. Patriciu, K. Cleary, and D. Stoianovici, “Does needle rotation improve lesion targeting?” *The International Journal of Medical Robotics and Computer Assisted Surgery*, vol. 7, no. 2, pp. 138–147, 2011.
- [11] T. Shin-ei, K. Yuyama, M. Ujihara, and K. Mabuchi, “Reduction of insertion force of medical devices into biological tissues by vibration,” *Japanese Journal of Medical Electronics and Biological Engineering*, vol. 39, no. 4, pp. 292–296, 2001.
- [12] K. Muralidharan, *Mechanics of soft tissue penetration by a vibrating needle*, ProQuest, 2007.
- [13] M. L. Mulvihill, D. E. Booth, and B. M. Park, “Medical tool for reduced penetration force,” Aug. 31 2011, US Patent App. 13/222,363.
- [14] C. Canudas-de Wit, P. Tsiotras, E. Velenis, M. Basset, and G. Gissinger, “Dynamic friction models for road/tire longitudinal interaction,” *Vehicle System Dynamics*, vol. 39, no. 3, pp. 189–226, 2003.
- [15] A. Asadian, R. V. Patel, and M. R. Kermani, “A distributed model for needle-tissue friction in percutaneous interventions,” in *IEEE International Conference on Robotics and Automation (ICRA)*, IEEE, 2011, pp. 1896–1901.
- [16] V. K. Astashev, K. Khusnutdinova, and V. Babitsky, *Ultrasonic processes and machines: dynamics, control and applications*, Springer, 2007.

# Chapter 4

## Systematic Optimal Design of a Langevin Piezoelectric Actuator

### 4.1 Introduction

High-power ( $10\text{--}1000\text{ W/cm}^2$ ) low-frequency ( $20\text{--}100\text{ kHz}$ ) ultrasound has a wide range of applications in both industrial and medical procedures. Generally, an ultrasonic transducer generates and transmits an oscillatory motion with a specific direction, frequency and intensity. The interaction of the vibratory tool with the workpiece or medium to be treated then causes the damage/deformation process to alter/shape the workpiece/medium. Drastic change of fragility, plasticity and viscosity of materials under ultrasonic-assisted machining, observed in numerous experiments, has made such technique very attractive for various applications, such as plastic deformation of metals, drawing of wires and pipes, machining of brittle materials, and cutting and welding of metals and plastics [1].

High-power ultrasound has also been used in various clinical applications such as dentistry, phaco-emulsification, bone cutting and maxillofacial surgery, neurosurgery, tissue dissection and tumor fragmentation as well as vascular plaque ablation [2]. While the mechanism of high-power ultrasonic tissue removal and damage differs for individual tissues, it is believed that a combination of the mechanical impact of direct shear, acoustic streaming and pressure wave components as well as cavitation is responsible for tissue fragmentation [2]. Thermal effect is also believed to be another

---

This chapter contains material submitted for publication in Iman Khalaji, Michael D. Naish and Rajni V. Patel, “Articulating Minimally Invasive Ultrasonic Tool for Robotics-Assisted Surgery,” submitted to *IEEE International Conference on Robotics and Automation (ICRA)*, 2015.

damage mechanism that can lead to necrosis and protein denaturation and thereby hemostasis.

Traditionally, an ultrasonically activated device consists of a vibration generator (often a Langevin piezoceramic) sandwiched between a back mass and a front-mass section. Since piezoceramic transducers can only generate a few microns of vibration amplitude (typically 0.1% of its length), the device is tuned to resonate at a certain ultrasonic frequency. Therefore, its overall length must be a half-wavelength or a multiple of the half-wavelength at the driving frequency. A vibration amplifier (horn) is also usually employed as part of the front mass to amplify the delivered vibration amplitude.

Designing a piezoelectric transducer is generally a complicated task, since overall performance of the system is dependent on many factors, such as geometrical dimension and material properties of various parts, number of piezoelectric elements, mode and frequency of driving the system, etc. Depending on the specific application, multiple objective functions can be defined which are usually contradictory. In [3], a constrained multi-objective optimization problem is formulated to optimize a Langevin transducer. Several multi-objective evolutionary algorithms are then applied to the optimization problem to find a set of pareto-optimal solutions. Nevertheless, large number of the design parameters makes the optimization rather a time-demanding and complex procedure. The obtained results are also bounded with the assumptions that have been made and are all case dependent. In other words, should a new set of constraints be applied, a whole new set of pareto-optimal solutions have to be sought.

While ultrasonically activated scalpels have demonstrated superior characteristics over electro-cautery devices in coagulation and cutting of soft tissue with more precision and speed, less cutting force, less smoke and reduced collateral damage, several drawbacks such as large size, less flexibility, high power consumption, and high transmission loss have rendered them unattractive for advanced internal body operations, particularly in Robotics-Assisted Minimally Invasive Surgery (RAMIS). Miniaturizing such devices for portable and internal body applications will, therefore, extend their functionality in more advanced surgical therapy, such as drug delivery

and localized treatment of disease through RAMIS.

In this work, the design of a piezoelectric transducer with stepped horn profile is presented. In order to minimize the size of the device, the design space has been limited to one half-wavelength in the overall length. Mason equivalent circuit network theory [4] is used to formulate the problem in its general form and determine the interaction between various design parameters. Using two objective functions, i.e., delivered vibration amplitude and the input power, pareto front curve is obtained and the most optimum solution is sought considering the design constraints. Finally, Finite Element Analysis (FEA) is employed to evaluate the performance of the designed transducer.

## 4.2 Structure of a Langevin Piezoelectric Transducer

As schematically illustrated in Fig. 4.1, a Langevin ultrasonic transducer can be broken down into three general sections, namely, high-acoustic-impedance back-mass section, piezoelectric section, and low-acoustic-impedance front mass section. Piezoelectric elements are sandwiched between the front and back sections to provide enough pre-compression on the piezoceramic elements and to avoid tensioning them during vibration excitation. Usually an even number of piezoelectric rings, electrically connected in parallel, are used with polling direction along the thickness or radial direction. The most common actuators, however, work at longitudinal vibration mode where larger vibration amplitude and higher power density can be delivered simultaneously. A sinusoidal constant voltage or current source is then used to drive the resulting actuator at a predetermined resonance frequency.

Proper choice of materials for each section is the next design criteria that must be taken into account. As shown in Eisner [5], materials with low internal damping and high values of maximum particle velocity are required to achieve high vibration amplitude and high power density at the output. The latter is given by

$$v_m = \phi S_m c, \quad (4.1)$$

where  $v_m$  is the particle velocity,  $\phi$  is a function of geometry,  $S_m$  is the maximum (fatigue) strain and  $c$  is the speed of longitudinal wave within the material [5]. Piezoelectric materials tend to have low values of  $S_m c$  of around 1 m/Sec [6], whereas certain titanium alloys (e.g., Ti-6Al-4V) and aluminum alloys (e.g., Aluminum 7075-T6) demonstrate  $S_m c$  values of around 32 m/Sec and 13 m/Sec, respectively [5]. As a function of geometry,  $\phi$  is also a figure of merit which indicates the feasibility of a certain geometry in amplifying the vibration velocity. Thus by using titanium or aluminum vibration amplifier (horn) as part of the front mass, one can achieve higher vibration amplitude using a piezoelectric transducer.

While miniaturizing the ultrasonic transducer may enhance their flexibility and efficiency, proper design of the horn profile is the bottleneck of such miniaturization. Various ultrasonic horn profiles have been investigated and developed by many researchers over the past 60 years. Analytical approaches have been extensively employed to analyze and design several generic profiles such as conical, exponential, catenoidal, cosine, stepped [1, 7, 8] and Gaussian profiles [5]. It has, however, been shown that the stepped horn gives the highest vibration amplitude amplification among all known types of horns having the same input–output cross sectional ratio, although it demonstrates the poorest  $\phi$  value, due to the large stress concentration at the step section.

In the next section, equivalent circuit network theory is utilized to formulate and analyze a piezoelectric transducer with stepped horn that resonates at its first longitudinal vibration mode.

### 4.3 Equivalent Circuit Network Modelling

Analytical solutions to the 1-dimensional wave equation in piezoelectric transducers are usually difficult to derive. Exploiting Transmission Line Theory, Mason [4] and Krimholtz *et al.* [9] proposed equivalent circuits to model the electrical as well as the mechanical properties of piezoelectric materials in a composite structure. In both models, each acoustic segment with arbitrary length and propagation parameters is represented by a two-port network impedance, thanks to the analogies to the Trans-



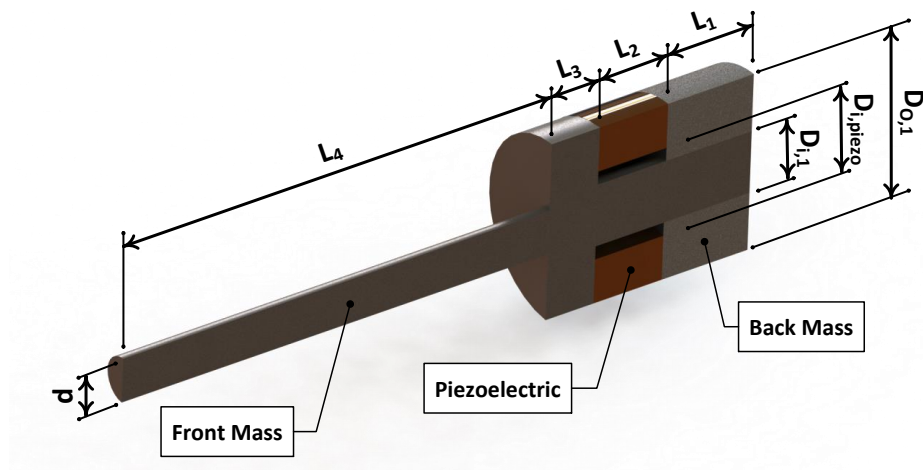


Figure 4.1: A schematic illustration of a Langevin piezoelectric transducer.

mission Line Theory. In Mason equivalent circuit [4], a piezoelectric plate, operating in the thickness mode, is modelled as a three-port network impedance, where two mechanical ports, corresponding to the front and back surface of the plate, are connected to a one electrical port through an ideal electromechanical transformer. The Krimholtz *et al.* [9] (KLM) equivalent circuit, on the other hand, models a piezoelectric transducer as a mechanical transmission line coupled at the middle to a lumped electrical network through an ideal transformer. Despite being a constant value in Mason model, the turns ratio of the ideal transformer in KLM model is a function of the exciting frequency [9, 10]. As pointed out by Sherit *et al.* [11], this causes the KLM model to have limited applicability when high impedance acoustic layers are used along with a piezoelectric layer. Therefore, a modified version of the KLM model is proposed in [11].

Fig. 4.2 shows the schematic of a half-wavelength piezoelectric transducer with a stepped horn and amplification ratio of  $k = \frac{S_{back}}{S_{front}} > 1$ , and its equivalent Mason circuit network model. The transducer can be divided into four sections in which sections 3 and 4 (horn) are titanium cylindrical rods, and sections 1 and 2 are composite sections made of titanium and steel, and titanium and piezoceramic materials, respectively. Since the mechanical impedance of the piezoelectric stack and steel back mass are roughly one order of magnitude higher than the mechanical impedance of the titanium segment in sections 1 and 2, it is safe to assume a constant strain at

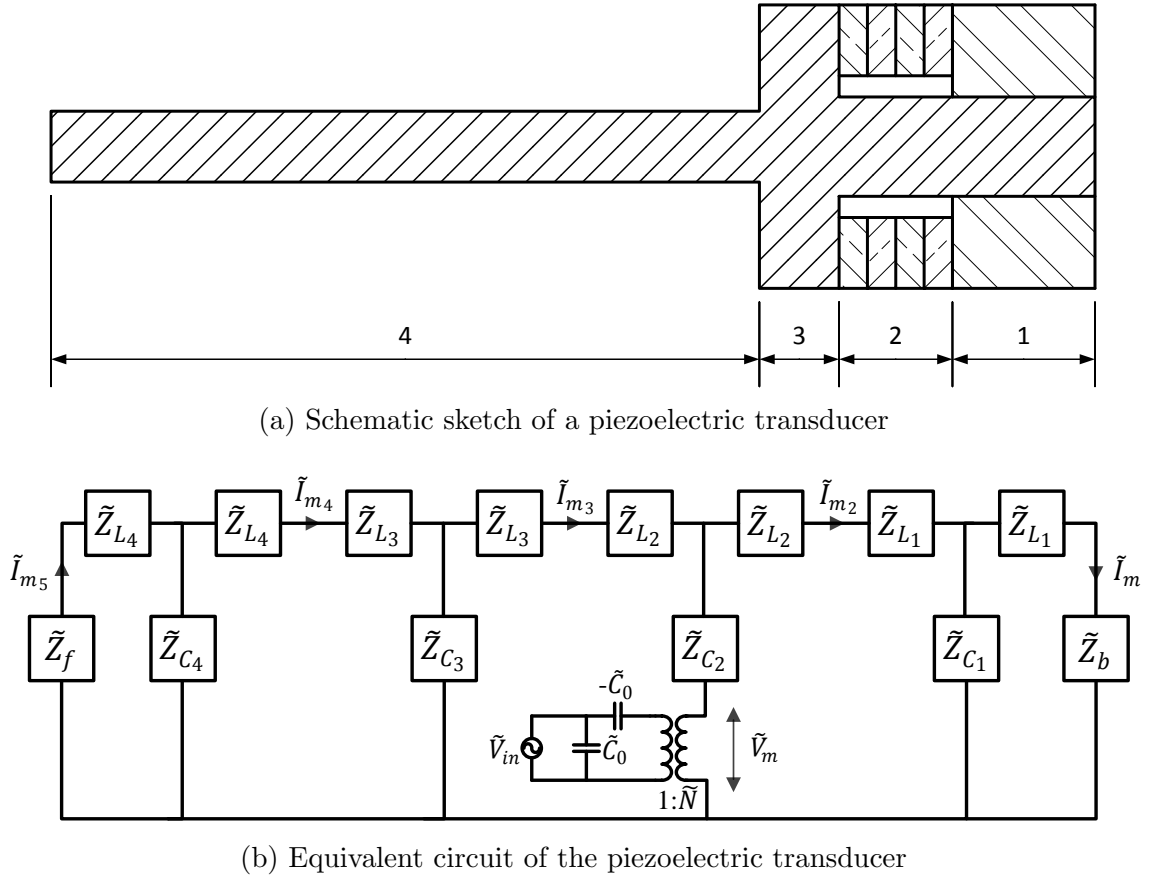


Figure 4.2: Schematic of a piezoelectric transducer and its corresponding equivalent circuit.

any cross section within sections 1 and 2. This means acoustic elements in Mason's equivalent circuit should be added in series for each section 1 and 2 [12].

As can be seen from Fig. 4.2, each passive section of the transducer is represented by a two-port network, whereas the piezoelectric segment consisting of  $n$  short segments ( $\xi_2 < \pi$  [13]) is represented using a 3-port network (2 mechanical ports, one electrical port), thanks to Mason's model.  $\tilde{Z}_f$  and  $\tilde{Z}_b$  in Fig. 4.2 are the complex impedance of the front and back loads being applied to the transducer during its operation. Depending on the application of the transducer, they can be obtained experimentally or through FEA and analytical methods [14]. The complex inductive

impedances in the mechanical ports are then given by:

$$\tilde{Z}_{L_1} = jZ_{0,1,S} \tan\left(\frac{\tilde{\xi}_{1,S}}{2}\right) + jZ_{0,1,Ti} \tan\left(\frac{\tilde{\xi}_{1,Ti}}{2}\right) \quad (4.2a)$$

$$\tilde{Z}_{L_2} = jZ_{0,2,Pi} \tan\left(\frac{\tilde{\xi}_{2,Pi}}{2}\right) + jZ_{0,2,Ti} \tan\left(\frac{\tilde{\xi}_{2,Ti}}{2}\right) \quad (4.2b)$$

$$\tilde{Z}_{L_3} = jZ_{0,3,Ti} \tan\left(\frac{\tilde{\xi}_{3,Ti}}{2}\right) \quad (4.2c)$$

$$\tilde{Z}_{L_4} = jZ_{0,4,Ti} \tan\left(\frac{\tilde{\xi}_{4,Ti}}{2}\right). \quad (4.2d)$$

Similarly, the complex capacitive impedances can be obtained as:

$$\tilde{Z}_{C_1} = \frac{-jZ_{0,1,S}}{\sin\left(\frac{\tilde{\xi}_{1,S}}{2}\right)} + \frac{-jZ_{0,1,Ti}}{\sin\left(\frac{\tilde{\xi}_{1,Ti}}{2}\right)} \quad (4.3a)$$

$$\tilde{Z}_{C_2} = \frac{-jZ_{0,2,Pi}}{\sin\left(\frac{\tilde{\xi}_{2,Pi}}{2}\right)} + \frac{-jZ_{0,2,Ti}}{\sin\left(\frac{\tilde{\xi}_{2,Ti}}{2}\right)} \quad (4.3b)$$

$$\tilde{Z}_{C_3} = \frac{-jZ_{0,3,Ti}}{\sin\left(\frac{\tilde{\xi}_{3,Ti}}{2}\right)} \quad (4.3c)$$

$$\tilde{Z}_{C_4} = \frac{-jZ_{0,4,Ti}}{\sin\left(\frac{\tilde{\xi}_{4,Ti}}{2}\right)}, \quad (4.3d)$$

where

$$Z_{0,1,S} = \rho_{S,C} S \beta S_{tr} \quad (4.4a)$$

$$Z_{0,1,Ti} = \rho_{Ti} c_{Ti} (1 - \beta) S_{tr} \quad (4.4b)$$

$$Z_{0,2,Pi} = \rho_{Pi} c_{Pi} \alpha S_{tr} \quad (4.4c)$$

$$Z_{0,2,Ti} = Z_{0,1,Ti} \quad (4.4d)$$

$$Z_{0,3,Ti} = \rho_{Ti} c_{Ti} S_{tr} \quad (4.4e)$$

$$Z_{0,4,Ti} = \frac{Z_{0,3,Ti}}{k}, \quad (4.4f)$$

are the characteristic impedances of various sections, in which  $\rho$ ,  $c$ ,  $S_{tr}$ , and  $k$  are density, longitudinal wave speed, transducer cross section and cross sectional ratio of the stepped horn, respectively. The subscripts S, Ti and Pi in (4.2)–(4.4) stand for Steel, Titanium and Piezoelectric sections, respectively. In addition, cross sectional ratios  $\alpha$  and  $\beta$  are defined as:

$$\alpha = \frac{\text{Piezoceramic ring stack cross section}}{\text{Transducer cross section}}$$

$$\beta = \frac{\text{Steel back mass cross section}}{\text{Transducer cross section}},$$

where  $\alpha \leq \beta$ . The complex values  $\tilde{\xi}$  in (4.2) and (4.3) are defined by:

$$\tilde{\xi}_{1,S} = \xi_1 \left( 1 - \frac{j}{2Q_{m_S}} \right) \quad (4.5a)$$

$$\tilde{\xi}_{1,Ti} = \xi_1 \left( 1 - \frac{j}{2Q_{m_{Ti}}} \right) \frac{c_S}{c_{Ti}} \quad (4.5b)$$

$$\tilde{\xi}_{2,Pi} = \xi_2 \left( 1 - \frac{j}{2Q_{m_{Pi}}} \right) \quad (4.5c)$$

$$\tilde{\xi}_{2,Ti} = \xi_2 \left( 1 - \frac{j}{2Q_{m_{Ti}}} \right) \frac{c_{Pi}}{c_{Ti}} \quad (4.5d)$$

$$\tilde{\xi}_{3,Ti} = \xi_3 \left( 1 - \frac{j}{2Q_{m_{Ti}}} \right) \quad (4.5e)$$

$$\tilde{\xi}_{4,Ti} = \xi_4 \left( 1 - \frac{j}{2Q_{m_{Ti}}} \right), \quad (4.5f)$$

where  $Q_{m_S}$ ,  $Q_{m_{Pi}}$  and  $Q_{m_{Ti}}$  are the mechanical quality factors corresponding to steel, piezoelectric and titanium materials, respectively.  $\xi_1$ ,  $\xi_2$ ,  $\xi_3$  and  $\xi_4$  are in fact the multiplication of the wave number and the length of each section and can be obtained

as:

$$\xi_1 = \frac{\omega L_1}{c_S} \quad (4.6a)$$

$$\xi_2 = \frac{\omega L_2}{c_{Pi}} \quad (4.6b)$$

$$\xi_3 = \frac{\omega L_3}{c_{Ti}} \quad (4.6c)$$

$$\xi_4 = \frac{\omega L_4}{c_{Ti}}, \quad (4.6d)$$

where  $L_1$  to  $L_4$  are the corresponding lengths of sections 1 to 4. Frequency of the driving voltage is also denoted by  $\omega$ .

$\tilde{C}_0$ , the equivalent capacitance, and  $\tilde{N}$ , the complex electromechanical conversion coefficient of the electrical port of the Mason's equivalent circuit can be obtained from:

$$\tilde{C}_0 = \frac{n_{0Pi}^2 \alpha S_{tr}}{L_2} \tilde{\epsilon}_{33}^S \quad (4.7)$$

$$\tilde{N} = \frac{n_{0Pi} \alpha S_{tr}}{L_2} \frac{\tilde{d}_{33}}{\tilde{s}_{33}^E}, \quad (4.8)$$

where  $n_{0Pi}$  is the number of piezoceramic rings,  $\tilde{\epsilon}_{33}^S$  is the clamped (zero strain) complex permittivity of the piezoelectric material in the thickness mode,  $\tilde{d}_{33}$  is the complex piezoelectric charge constant, and  $\tilde{s}_{33}^E$  is the short-circuit complex mechanical compliance of the piezoelectric material. The complex values  $\tilde{\epsilon}_{33}^S$ ,  $\tilde{d}_{33}$  and  $\tilde{s}_{33}^E$  can be calculated from:

$$\tilde{\epsilon}_{33}^S = \epsilon_{33}^S \left( 1 - \frac{j}{Q_{ePi}} \right) \quad (4.9a)$$

$$\tilde{s}_{33}^E = s_{33}^E \left( 1 - \frac{j}{Q_{mPi}} \right) \quad (4.9b)$$

$$\tilde{d}_{33} = d_{33} \left( 1 - \frac{j}{Q_{kPi}} \right), \quad (4.9c)$$

where  $Q_{ePi}$ ,  $Q_{mPi}$  and  $Q_{kPi}$  are the quality factors for the dielectric, elastic and electromechanical coupling constants, respectively [15]. They can be calculated from the

loss tangents associated with dielectric ( $\tan(\delta_e)$ ), elastic ( $\tan(\delta_m)$ ), and piezoelectric losses ( $\tan(\delta_k)$ ) as follows:

$$Q_{e\text{Pi}} = \frac{1}{\tan(\delta_e)} \quad (4.10a)$$

$$Q_{m\text{Pi}} = \frac{1}{\tan(\delta_m)} \quad (4.10b)$$

$$Q_{k\text{Pi}} = \frac{1}{\tan(\delta_k)}. \quad (4.10c)$$

Using basic network circuit theory, the total acoustic impedance of the back mass section and part of the piezoceramic section, located at the right side of  $\tilde{Z}_{C_2}$  in Fig. 4.2, can be obtained as:

$$\tilde{Z}_{\text{right}} = \tilde{Z}_{L_1} + \tilde{Z}_{L_2} + \frac{(\tilde{Z}_b + \tilde{Z}_{L_1})\tilde{Z}_{C_1}}{\tilde{Z}_b + \tilde{Z}_{L_1} + \tilde{Z}_{C_1}}. \quad (4.11)$$

Similarly, the total acoustic impedance of the left side of  $\tilde{Z}_{C_2}$  in Fig. 4.2 can be calculated as follows:

$$\tilde{Z}_{10} = \frac{(\tilde{Z}_f + \tilde{Z}_{L_4})\tilde{Z}_{C_4}}{\tilde{Z}_f + \tilde{Z}_{L_4} + \tilde{Z}_{C_4}} \quad (4.12)$$

$$\tilde{Z}_{\text{left}} = \tilde{Z}_{L_3} + \tilde{Z}_{L_2} + \frac{(\tilde{Z}_{L_3} + \tilde{Z}_{L_4} + \tilde{Z}_{L_{10}})\tilde{Z}_{C_3}}{\tilde{Z}_{L_3} + \tilde{Z}_{L_4} + \tilde{Z}_{L_{10}} + \tilde{Z}_{C_3}}. \quad (4.13)$$

The total acoustic impedance of the equivalent circuit can then be obtained as:

$$\tilde{Z}_m = \tilde{Z}_{C_2} + \frac{\tilde{Z}_{\text{left}}\tilde{Z}_{\text{right}}}{\tilde{Z}_{\text{left}} + \tilde{Z}_{\text{right}}}. \quad (4.14)$$

Obtaining the total mechanical impedance,  $\tilde{Z}_m$ , one can transform it into the electrical port of the equivalent circuit through the ideal transformer with  $1 : \tilde{N}$  turns ratio. Therefore, combining (4.7), (4.8) and (4.14), the total electrical impedance as seen from the electrical port is:

$$\tilde{Z}_{\text{tot}} = \tilde{Z}_{C_0} - \frac{\tilde{Z}_{C_0}^2 \tilde{N}^2}{\tilde{Z}_m}, \quad (4.15)$$

where  $\tilde{Z}_{C_0} = \frac{1}{j\omega\tilde{C}_0}$ , and  $\tilde{C}_0$  can be obtained from (4.7). Hence,  $\tilde{I}_{\text{in}}$ , the total current

passing through the piezoelectric elements, and  $\tilde{P}_{\text{in}}$ , the input power, are obtained from:

$$\tilde{I}_{\text{in}} = \frac{\tilde{V}_{\text{in}}}{\tilde{Z}_{\text{tot}}} \quad (4.16)$$

$$\tilde{P}_{\text{in}} = \tilde{I}_{\text{in}} \tilde{V}_{\text{in}} = \left| \tilde{I}_{\text{in}} \right| \left| \tilde{V}_{\text{in}} \right| \cos(\theta), \quad (4.17)$$

where  $\theta$  is the phase difference between the applied voltage,  $\tilde{V}_{\text{in}}$ , and the input current,  $\tilde{I}_{\text{in}}$ . Provided that the internal damping of the transducer is small, the total impedance of the system at resonance (anti-resonance) becomes resistive, i.e.,  $\text{Im}(\tilde{Z}_{\text{tot}}) = 0$  [10]. Therefore,  $\tilde{V}_{\text{in}}$  and  $\tilde{I}_{\text{in}}$  will be in-phase, i.e.  $\theta = 0$ . Hence,  $\tilde{P}_{\text{in}} = |\tilde{I}_{\text{in}}| |\tilde{V}_{\text{in}}|$  will become maximum around the resonance (anti-resonance) frequency bandwidth.

Using the Kirchhoff's voltage law (KVL) and current law (KCL), it is possible to derive the currents that pass through each branch of the equivalent circuit in Fig. 4.2. The resulting  $\tilde{I}_{m_1}$  to  $\tilde{I}_{m_5}$ , given in Appendix A, correspond to the velocity of various boundary sections between the regions, from the front of the transducer to the back [16]. Using the obtained  $\tilde{I}_{m_i}, i = 1, \dots, 5$ , the mode shapes can also be extracted readily.

One can also calculate the voltage differences associated with each boundary section between the regions using basic circuit theory. The resulting voltages demonstrate the transferred force from one section to the other, as a result of the excitation of piezoelectric elements at certain frequency.

Explicit mathematical expressions of the above equations cannot be included here, due to their complexity. Nonetheless, using a symbolic computation engine, such as Maple<sup>TM</sup> (Maplesoft, Waterloo, Canada), one can simplify the above equations and observe the interaction of the design variables on the transducer output performance. Assuming  $\tilde{g}(\alpha, \beta, \xi_1, \xi_2, \xi_3, \xi_4)$  and  $\tilde{f}(\alpha, \beta, \xi_1, \xi_2, \xi_3, \xi_4)$  as complex multi-variable functions, the abstract form of the transducer tip velocity, total impedance, input power and input current can be expressed respectively as:

$$\tilde{v}_5 = \tilde{I}_{m_5} = \tilde{g}(\alpha, \beta, \xi_1, \xi_2, \xi_3, \xi_4) \omega n_{0\text{Pi}} \tilde{V}_{\text{in}} \quad (4.18)$$

$$\tilde{Z}_{\text{tot}} = \tilde{f}(\alpha, \beta, \xi_1, \xi_2, \xi_3, \xi_4) \frac{1}{\omega^2 n_{0\text{Pi}}^2} \frac{1}{S_{\text{tr}}} \quad (4.19)$$

$$\tilde{P}_{\text{in}} = \frac{\tilde{V}_{\text{in}}^2}{\tilde{Z}_{\text{tot}}} = \frac{1}{\tilde{f}(\alpha, \beta, \xi_1, \xi_2, \xi_3, \xi_4)} \omega^2 n_{0\text{Pi}}^2 S_{\text{tr}} \tilde{V}_{\text{in}}^2 \quad (4.20)$$

$$\tilde{I}_{\text{in}} = \frac{1}{\tilde{f}(\alpha, \beta, \xi_1, \xi_2, \xi_3, \xi_4)} \omega^2 n_{0\text{Pi}}^2 S_{\text{tr}} \tilde{V}_{\text{in}}. \quad (4.21)$$

Note that by factoring out the exciting frequency,  $\omega$ , in (4.18), the vibration amplitude at the tip of the transducer can be easily derived as:

$$\tilde{u}_5 = \frac{\tilde{v}_5}{\omega} = \tilde{g}(\alpha, \beta, \xi_1, \xi_2, \xi_3, \xi_4) n_{0\text{Pi}} \tilde{V}_{\text{in}}. \quad (4.22)$$

Hence, it can be understood from the above equations that the delivered vibration amplitude of the piezoelectric transducer,  $\tilde{u}_5$ , is independent from its total cross section,  $S_{\text{tr}}$ , and the exciting frequency,  $\omega$ . Moreover, it can be observed that the functions  $\tilde{g}$  and  $\frac{1}{\tilde{f}}$  are strictly increasing with respect to  $\alpha$  ( $\frac{\partial \tilde{g}}{\partial \alpha} > 0$ ,  $\frac{\partial}{\partial \alpha} \frac{1}{\tilde{f}} > 0$ ,  $\forall 0 < \alpha \leq \beta < 1$ ). Therefore, higher values of  $\alpha$  will result in larger vibration velocity (amplitude) at the tip of the transducer and higher input power (current). In other words, by employing piezoelectric rings with higher cross section ratio, larger vibration displacement will be attained at the cost of higher input power (current).

## 4.4 Optimization of the Langevin Piezoelectric Transducer

The optimal design of a Langevin piezoelectric actuator is quite cumbersome, due to the large number of variables that affect several performance criteria of the transducer. Fu *et al.* [3,17] proposed a multi-objective optimization approach using genetic algorithms to find a set of pareto-optimal solutions. While the obtained results are quite promising, they lack the proper understanding of the interaction among the design variables. They are also case dependent, since most constraints applied on the design variables (such as working frequency, voltage, actuator cross section) make the design space quite limited.



#### 4.4.1 Problem statement

The optimization of a piezoelectric transducer with a stepped horn is formulated as a constrained multi-variable multi-objective optimization problem as stated below:

**Objective functions:** A number of performance criteria can be defined for a piezoelectric transducer, such as piezoelectric coupling factor, piezoelectric quality number, frequency spacing between neighbouring modes, amplification ratio response between the front mass and the back mass, the location of the nodal plane along the transducer, transducer length, input power and vibration amplitude. Similar to [3,17], the inverse of vibration amplitude at the tip of the transducer (4.22) and the required input power (4.20) to drive the system, are considered as objective functions to be minimized in this work.

**Design variables:**  $\xi_1, \xi_2, \xi_3$  and  $\xi_4$  are the primary design variables which determine the geometrical features of the transducer, provided that the working frequency is pre-determined (4.6). The driving voltage,  $\tilde{V}_{in}$ , the number of piezoceramic rings,  $n_{0Pi}$ , total cross section of the transducer,  $S_{tr}$ , the driving frequency,  $\omega$ , and cross sectional ratios,  $\alpha$  and  $\beta$ , are the secondary set of variables that directly affect the objective functions. As will be discussed later, the secondary design variables are predetermined due to structural, geometrical or power source constraints. Therefore, only the primary design variables, i.e.  $\{\xi_1, \xi_2, \xi_3, \xi_4\}$ , will be considered for the multi-objective optimization problem.

Contrary to [3], material choices for various sections, i.e., back mass, piezoelectric rings and front mass, are not considered as the design parameters in this work. In fact, material choices are preselected for each section. Should any new material be utilized for a section, another set of pareto-optimal solutions has to be sought. By comparing various pareto-optimal curves, the designer would be able to distinguish which material to choose at what level of input power and/or vibration amplitude.

**Design constraints:** Considering the practical design requirements, such as total length, size, fatigue limit of the selected materials, input power source etc., several constraints associated with the search region of the design variables are introduced, as below:

- As explained earlier, the vibration amplitude at the output is independent from total cross section of the transducer. Hence, it may seem logical to make a super-small transducer that requires only small amount of power. The resulting device will, however, be more suited for micro-surgery [18, 19] rather than macro-surgery, due to the low rigidity of the cutting blade. Thus, the required lateral stiffness of the front mass at its both ends combined with its fatigue limit, in addition to the desired amplification ratio of the stepped horn will determine the smallest allowable diameter of the transducer.
- Once the transducer outer diameter is determined, cross sectional ratios  $\alpha$  and  $\beta$  will be chosen based on the available piezoceramic ring size and the standard thread size for the back mass and the front mass connection.
- As can be seen from (4.20), (4.21) and (4.22), by keeping  $n_{0\text{Pi}}\tilde{V}_{\text{in}}$  constant, the tip vibration displacement and the input power remain constant, while the input current will change. Therefore, depending on the power source limitation, proper number of piezoceramic stacks should be selected, while the input voltage has to be adjusted to keep the consumed power constant. On the other hand, since  $\tilde{u}_5 \propto n_{0\text{Pi}}\tilde{V}_{\text{in}}$  and  $\tilde{P}_{\text{in}} \propto n_{0\text{Pi}}^2\tilde{V}_{\text{in}}^2$ , low values of  $n_{0\text{Pi}}\tilde{V}_{\text{in}}$  should be chosen by maximizing  $\tilde{g}(\alpha, \beta, \xi_1, \xi_2, \xi_3, \xi_4)$  to achieve the desired tip vibration amplitude and minimize the input power.
- Similarly, since  $\tilde{u}_5 \propto \omega$  and  $\tilde{P}_{\text{in}}, \tilde{I}_{\text{in}} \propto \omega^2$ , the smaller the resonance frequency, the smaller power (current) is required for driving the system. Smaller resonance frequency will, however, make the total length of the ultrasonic device rather longer and may make it unsuitable for internal body surgical application. Therefore, using specifications of traditional ultrasonic surgical scalpels (e.g., harmonic scalpel, Ethicon Endo-Surgery, Cincinnati, OH, USA), it may be more appropriate to target 45–55 kHz frequency range with maximum vibration amplitude of 80–100  $\mu\text{m}$  p-p [20–22].
- Considering section 4 of the front mass within the ultrasonic transducer as an impedance matching interface between the source of energy (high acoustic impedance piezoelectric elements) and the load (low acoustic impedance soft tissue), the maximum transmission of energy will be achieved with one-quarter

wavelength for section 4, i.e.  $\xi_4 = \frac{\pi}{2}$  [23]. In the case of operating the ultrasonic transducer in the air, i.e.  $\tilde{Z}_f = 0$ , this leads to a node at the interface of section 3 and section 4, i.e.,  $\tilde{v}_4 = \tilde{I}_{m_4} = 0$ , according to (A.2), and maximum load transfer between the two sections.

- It is required for the transducer to have the smallest possible length. Therefore, the actuator must resonate at its first longitudinal frequency and its total length must be a half wavelength of the driving frequency. Hence,

$$g_4(\xi_1, \xi_2, \xi_3) = \xi_1 + \xi_2 + \xi_3 - \frac{\pi}{2} \leq 0 \quad (4.23)$$

where a quarter wavelength is assumed for section 4. Additionally, each section must have a minimum length to make the final solution realizable. Therefore,

$$\begin{aligned} g_1(\xi_1, \xi_2, \xi_3) &= \xi_{1_{\min}} - \xi_1 \leq 0 \\ g_2(\xi_1, \xi_2, \xi_3) &= \xi_{2_{\min}} - \xi_2 \leq 0 \\ g_3(\xi_1, \xi_2, \xi_3) &= \xi_{3_{\min}} - \xi_3 \leq 0. \end{aligned} \quad (4.24)$$

- Assuming small structural damping of the transducer components, the total impedance of the system,  $\tilde{Z}_{\text{tot}}$ , becomes minimum (maximum) at resonance (anti-resonance), and therefore  $\text{Im}(\tilde{Z}_{\text{tot}}) = 0$ . This together with (4.19) leads to:

$$h_1(\xi_1, \xi_2, \xi_3) = \text{Im} \left( \tilde{f}(\alpha^*, \beta^*, \xi_1, \xi_2, \xi_3, \frac{\pi}{2}) \right) = 0 \quad (4.25)$$

where  $\alpha^*$ ,  $\beta^*$  and  $\frac{\pi}{2}$  are the previously described values selected for  $\alpha$ ,  $\beta$  and  $\xi_4$ .

**Optimization problem formulation:** The two-objective optimization problem can therefore be expressed as:

$$\begin{aligned} &\underset{\Xi}{\text{minimize}} && \mathbf{F}(\Xi) \\ &\text{subject to} && g_i(\Xi) \leq 0, \quad i = 1, \dots, 4 \\ &&& h_1(\Xi) = 0 \end{aligned} \quad (4.26)$$

where  $\Xi = [\xi_1, \xi_2, \xi_3]$  is the design variable vector,  $\mathbf{F}(\Xi) = [\frac{1}{|\tilde{u}_5|}, |\tilde{P}_{\text{in}}|]$  is the objective functions vector, and  $h_1(\Xi)$  and  $g_i(\Xi)$  are the constraint functions defined in (4.23)–(4.25).

Finding feasible solutions that satisfy both the inequality and equality constraint sets requires too many iterations. The equality constraint is, particularly, harder to satisfy, since for any pair of design variables, such as  $\xi_1$  and  $\xi_2$ , there is at most one, and only one  $\xi_3$  that satisfies (4.23)–(4.25). This can be easily proved by considering that the overall length of an ultrasonic transducer must be a half-wavelength or a multiple of the half-wavelength at the driving frequency. Therefore,

$$\forall \xi_1 > \xi_{1\min}, \forall \xi_2 > \xi_{2\min}, \forall k \in \mathbb{Z}_{\geq 0}, \quad \exists \xi_3^* \geq \xi_{3\min} : \quad h_1(\xi_1, \xi_2, \xi_3^* + k\pi) = 0, \quad (4.27)$$

where  $\mathbb{Z}_{\geq 0}$  is the set of non-negative integers, and  $\xi_3^*$  is the lowest possible solution for  $\xi_3$  that satisfies the equality constraint (4.25). Thus, if (4.23) holds true, i.e.  $\xi_1 + \xi_2 + \xi_3^* \leq \frac{\pi}{2}$ ,  $(\xi_1, \xi_2, \xi_3^*)$  is a feasible point for the optimization problem (4.26).

**Optimization implementation:** Solving the optimization problem can be performed through two scenarios. In the first scenario, pareto-optimal sets can be generated through both the traditional and evolutionary approaches. The traditional methods convert the multi-objective optimization problem into a single objective optimization problem and try to find the pareto-optimal solution sets. Pareto-based multi-objective evolutionary algorithms, on the other hand, are able to find multiple pareto-optimal solutions in a single run, thanks to their population-based approach.

In the second scenario, either the available power source, or the required vibration amplitude at the tip of the transducer is given. Therefore, the minimization problem will be downgraded to finding the proper values for the design parameters where the other objective function gets its lowest value.

In this work, the optimization problem is solved through the first scenario to demonstrate the pareto front curve. Assuming 80  $\mu\text{m}$  p-p of vibration amplitude, the problem is then solved through the second scenario to find a miniaturized ultrasonic transducer design with the lowest input power.

## 4.5 Finite Element Analysis

While equivalent circuit network modeling simplifies electro-mechanical structure of an ultrasonic transducer in the form of lumped-mass parameters, there are several fundamental assumptions that make the obtained results slightly different from reality. First and foremost, the assumption of plane acoustic wave propagation that is a key condition in 1-D wave equation is no longer valid at an abrupt cross-sectional change and its vicinity such as a stepped horn. Secondly, the effect of pre-compression applied on piezoelectric rings and nonlinear mechanical losses due to contact effect between various segments of a piezoelectric transducer cannot be correctly modeled using the equivalent circuit analogy. Finite element analysis, on the other hand, is well suited for detailed electro-mechanical analysis of piezoelectric transducers, although performing structural optimization of such transducers is usually quite tedious. Therefore, it is a common practice to design a piezoelectric transducer using equivalent circuits and evaluate the performance of the design (including resonance and anti-resonance frequencies, stress distribution, transducer tip displacement, required current and power, total impedance, etc.) through FE modeling.

In this work, ABAQUS FE software package (SIMULIA, Dassault Systmes, RI, USA) is used to asses the performance of the designed transducer. In order to extract all vibration modes and evaluate mode separation, a 3-D model of the piezoelectric transducer is created and meshed using 20-node quadratic brick, reduced integration elements. For the piezoelectric section, similar elements with additional charge degree-of-freedom are utilized to correctly simulate its electro-mechanical effect. The internal structural losses of the transducer are considered in this analysis by applying Rayleigh damping to each material, as set out by:

$$[C] = \alpha_{\text{damping}}[M] + \beta_{\text{damping}}[K],$$

where  $[C]$ ,  $[M]$  and  $[K]$  are the damping, mass and stiffness matrices in finite element formulation.  $\alpha_{\text{damping}}$  and  $\beta_{\text{damping}}$  are also the Rayleigh damping coefficients that represent viscous damping and stiffness damping, respectively. It has been shown that as the vibration frequency gets increased,  $\alpha_{\text{damping}}$  becomes negligible, while

$\beta_{\text{damping}}$ 's effect becomes more substantial [24,25], and can be obtained through:

$$\beta_{\text{damping}} = \frac{1}{\omega_r Q_m},$$

where  $Q_m$  is the mechanical quality factor of the vibrating material. The damping effect can also be applied as a global structural damping [25] where its value is estimated at the beginning of the analysis and then corrected after harmonic analysis of the fabricated transducer. General contact problem is then defined for the whole transducer during the subsequent steps. The pre-compression value of around 30 MPa [16] is first applied on piezoelectric rings through bolt load. This step usually stiffens the transducer by making proper contact between its various sections. It also slightly increases the resonance frequencies of the structure [16]. Pre-compression step is then followed by frequency analysis of the transducer to extract mode shapes and their corresponding resonance frequencies. Anti-resonance frequencies of the transducer at longitudinal mode shapes can also be extracted provided that appropriate voltage boundary conditions are imposed on the piezoelectric rings. Steady state dynamic analysis of the transducer is the final step of the analysis where sinusoidal voltage boundary condition is applied on piezoelectric rings at various frequencies. The response of the system to such excitation is then extracted in the form of displacement FRF (frequency response function), passing current through the piezoceramic rings, and impedance curve.

## 4.6 Results and Discussion

### 4.6.1 Pareto front

Using material properties in Table 4.1, as well as the constraints imposed on the primary and the secondary design variables in Table 4.2, the optimization problem (4.26) is formulated. Note that while satisfying (4.23) in order to keep the piezoelectric resonator at half-wavelength is a necessary condition, it is not sufficient. In fact, as it will be discussed later, the necessary and sufficient condition for a resonator

to be half-wavelength is a complex nonlinear function of the design parameters, in contrary to the linear inequality equation expressed in (4.23). Therefore, in solving the optimization problem, the inequality constrain (4.23) is relaxed, i.e.  $\xi_3 \leq 3\pi$ , to have not only half-wavelength resonators, but also a few other resonators with lengths longer than half-wavelength in the design space.

The optimization problem is then solved through a controlled elitist genetic algorithm (a variant of NSGA-II <sup>\*</sup>). Starting from population size of 300, an evenly distributed set of points on the Pareto front is obtained after about 150 generations. Fig. 4.3 demonstrates the obtained Pareto front curve in the objective space overlayed on around 700,000 data points generated by exhaustive search. As can be observed, the genetic algorithm has successfully captured the Pareto front associated with the design space for most part of the figure. For small power values and large tip displacement, however, the algorithm is trapped into local minima and could not correctly converge to the Pareto front. The problem may have been fixed, should new starting points have been used throughout the run.

Although the obtained Pareto front is obtained for specific secondary design parameters, i.e.,  $V_{in}$ ,  $n_{0Pi}$ ,  $S_{tr}$  and  $\omega$ , it can be adjusted according to (4.20) and (4.20), should new values are to be used for the parameters. On the other hand, if any new set of materials,  $\alpha$ ,  $\beta$ ,  $\xi_{1min}$ ,  $\xi_{2min}$  or  $\xi_{3min}$  is intended to be used, the optimization problem has to be solved again through the genetic algorithm to obtain a new Pareto front curve.

### 4.6.2 Case study

Using the obtained Pareto front, a miniaturized piezoelectric actuator with tip vibration amplitude of  $40 \mu m$  is designed. The required performance of such actuator is illustrated in Fig. 4.3 by a red dashed line. Fig. 4.4 shows the performance of the optimal designed actuator in terms of its tip vibration amplitude, total impedance, input power and input current. As can be observed, the actuator can deliver the required vibration amplitude at 50 kHz resonance frequency. The required power

---

<sup>\*</sup> Non-dominated sorting genetic algorithm [26]

Table 4.1: Material properties of the various sections of the piezoelectric actuator

Property	Units	Symbol	APC	Titanium	Steel	Copper
			841	Ti-6Al-4V	Alloy	Alloy
Relative dielectric constant	1	$K^T$	1375	—	—	—
Dielectric loss	%	$\tan(\delta)$	0.40	—	—	—
Curie point	$^{\circ}\text{C}$	$T_c$	320	—	—	—
Electromechanical coupling factor	%	$k_p$	0.6	—	—	—
		$k_{33}$	0.68	—	—	—
		$k_{31}$	0.33	—	—	—
		$k_{15}$	0.67	—	—	—
Piezoelectric charge constant	$10^{-12} \text{ m/V}$	$d_{33}$	300	—	—	—
		$-d_{31}$	109	—	—	—
		$d_{15}$	450	—	—	—
Piezoelectric voltage constant	$10^{-3} \text{ Vm/N}$	$g_{33}$	25.5	—	—	—
		$-g_{31}$	10.5	—	—	—
		$g_{15}$	35	—	—	—
		$Y_{11}^E$	7.6	11.04	17.918	11.50
Young's modulus	$10^{10} \text{ N/m}^2$	$Y_{33}^E$	6.3	11.04	17.918	11.50
Density	$10^3 \text{ Kg/m}^3$	$\rho$	7.6	4.418	7.723	8.90
Poisson's ratio	1	$\nu$	0.34	0.342	0.3	0.31
Mechanical quality factor	1	$Q_m$	1400	877.2	2325.6	3030.3

Metallic material properties are taken from [25]. Piezoelectric properties are adapted from the manufacturer product catalog.



Table 4.2: Primary and secondary design parameter constraints

	Design Parameter	Units	Chosen Value	Lower Bound	Upper Bound
Primary Design Parameters	$\xi_1$	1	—	$3 \times 10^{-3} \times \omega / c_S$	$\pi/2$
	$\xi_2$	1	—	$8 \times 10^{-4} \times \omega / c_{Pi}$	$\pi/2$
	$\xi_3$	1	—	$3 \times 10^{-3} \times \omega / c_{Ti}$	$3\pi$
	$\xi_4$	1	$\pi/2$	—	—
Secondary Design Parameters	$V_{in}$	V	5	—	—
	$n_{0Pi}$	1	4	—	—
	$S_{tr}$	mm <sup>2</sup>	$\frac{8^2 \times \pi}{4}$	—	—
	$\omega$	Hz	50,000	—	—
	$\alpha$	1	$\frac{8^2 - 3.5^2}{8^2}$	—	—
	$\beta$	1	$\frac{8^2 - 2.515^2}{8^2}$	—	—

source to drive such system is only 6.9 Watt, at slightly high current value of 690.3 mA and input voltage of 5 V. The anti-resonance frequency of such optimal design is 50793 Hz, which means that the piezoelectric actuator has the coupling factor of [17]:

$$k_{\text{eff}} = \left( \frac{f_a^2 - f_r^2}{f_a^2} \right)^{1/2} = \left( \frac{50793^2 - 50000^2}{50793^2} \right)^{1/2} = 0.1760,$$

where the anti-resonance frequency,  $f_a$ , and resonance frequency,  $f_r$ , are assumed to be equal to the parallel and series frequencies, respectively [17].

In order to evaluate the performance of the designed actuator, finite element model of the system is developed using ABAQUS FE software package (SIMULIA, Dassault Systmes, RI, USA). To make the 3-D model more realistic, 0.4 mm thick copper electrodes with material properties listed in Table 4.2 are inserted between each piezoelectric ring. In Table 4.3, the first several mode shapes and their corresponding resonance frequencies obtained from FE, are compared with the obtained results from equivalent circuit theory. Slight difference can be observed between the first and the second longitudinal resonance frequencies obtained from the two methods. It is also clear that there is a reasonable mode separation among various frequencies,

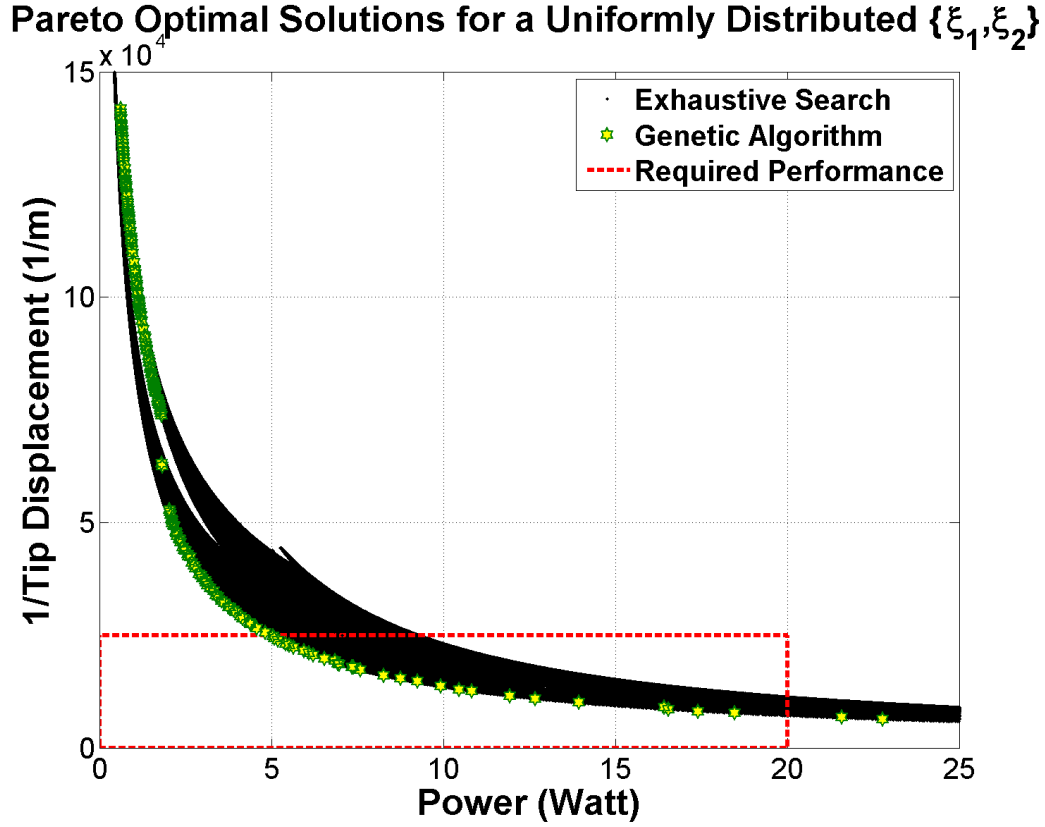


Figure 4.3: Pareto front obtained through Genetic algorithm, overlayed on around 700,000 solutions in the objective space obtained by exhaustive search.

particularly between the first longitudinal mode, and the second and the third lateral modes.

In order to better investigate the neighboring mode interactions, the frequency range between the second and the third lateral mode shapes are considered for the steady state dynamic analysis. Input voltage of 40 V is then swept within the chosen frequency range and the steady state response of the system is extracted. Fig. 4.5 shows the obtained vibration amplitude, total impedance, input power and input current of the transducer within the specified frequency range. By comparing Figs. 4.4 and 4.5 several points can be drawn:

- The first longitudinal natural frequency obtained from FE model is slightly smaller than the one predicted by equivalent circuit model. This could be due to employing copper electrodes in FE model, which in turn makes the total

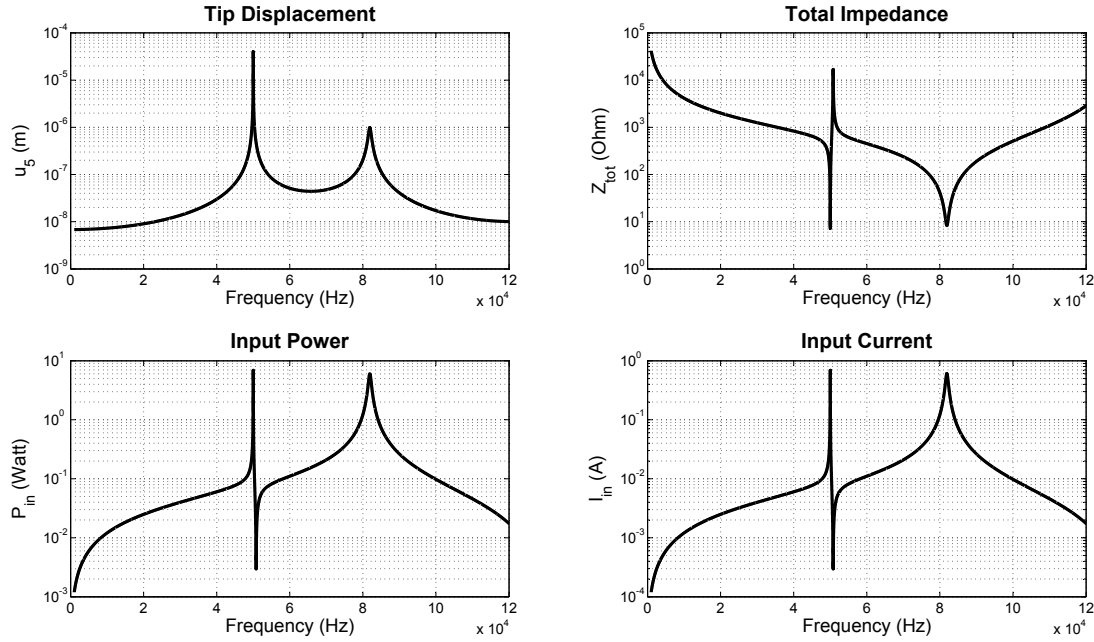


Figure 4.4: Performance measures of the optimal designed actuator.

length of the transducer longer and thus, its longitudinal resonance frequency smaller.

- Although 5 V of voltage input is considered for the equivalent circuit model, it would be insufficient to generate 40  $\mu\text{m}$  of tip vibration amplitude in FE model. This could be due to the fact that the FE model takes into account non-linear contact problem, as well as 3-D wave propagation within the actuator. Therefore, 40 V of voltage input is utilized to excite the transducer model in FE.
- While the overall total impedance of the actuator within the specified frequency range is predicted to be around 500–1500  $\Omega$  by the two methods, FE predicts smaller impedance difference between the resonance and anti-resonance states. Insufficient pre-stressing of the piezoelectric rings at the beginning of the FE analysis could be the reason why the transducer behaves less stiff and exhibits lower impedance difference between the two states.
- Different input voltage and total impedance of the two methods lead to dissimilar input current behavior at resonance, as it can be observed from Figs. 4.4 and 4.5. In the case of input power, however, the two methods predict almost

Table 4.3: Mode shapes and their associated frequencies by finite element and equivalent circuit methods

Mode Shape	Frequency (Hz)	
	by Finite Element Method	by Equivalent Circuit Method
1 <sup>st</sup> lateral	13931	—
1 <sup>st</sup> torsional	30177	—
2 <sup>nd</sup> lateral	36278	—
1 <sup>st</sup> longitudinal	resonance	50000
	anti-resonance	50793
3 <sup>rd</sup> lateral	62867	—
4 <sup>th</sup> lateral	70795	—
2 <sup>nd</sup> torsional	79205	—
3 <sup>rd</sup> torsional	90649	—
2 <sup>nd</sup> longitudinal	resonance	81915

the same amount of 7 Watt required power at resonance.

Overall, equivalent circuit model can be used to optimize the design of a piezoelectric actuator. Nevertheless, due to several assumptions that have been made in developing such model, the ultimate performance of the actuator has to be confirmed by means of finite element analysis. Moreover, the effect of adopting a certain horn profile (such as the stepped horn as analyzed in this work) on stress distribution within the transducer, can only be investigated through finite element analysis. Figure 4.6 shows such extensive analysis on the optimal designed actuator at both prestressing step and steady state dynamic analysis. As can be seen, while the stepped horn profile gives rise to the output vibration amplitude, high stress values are generated along the transducer due to the stress concentration effect of the stepped horn. Considering the fatigue strength of around 510 MPa for Ti-6Al-4V, the fatigue safety factor of the stepped horn will be 1.65. Further study is required to investigate employing other types of horn profile in a miniaturized piezoelectric actuator to achieve higher fatigue safety factor.

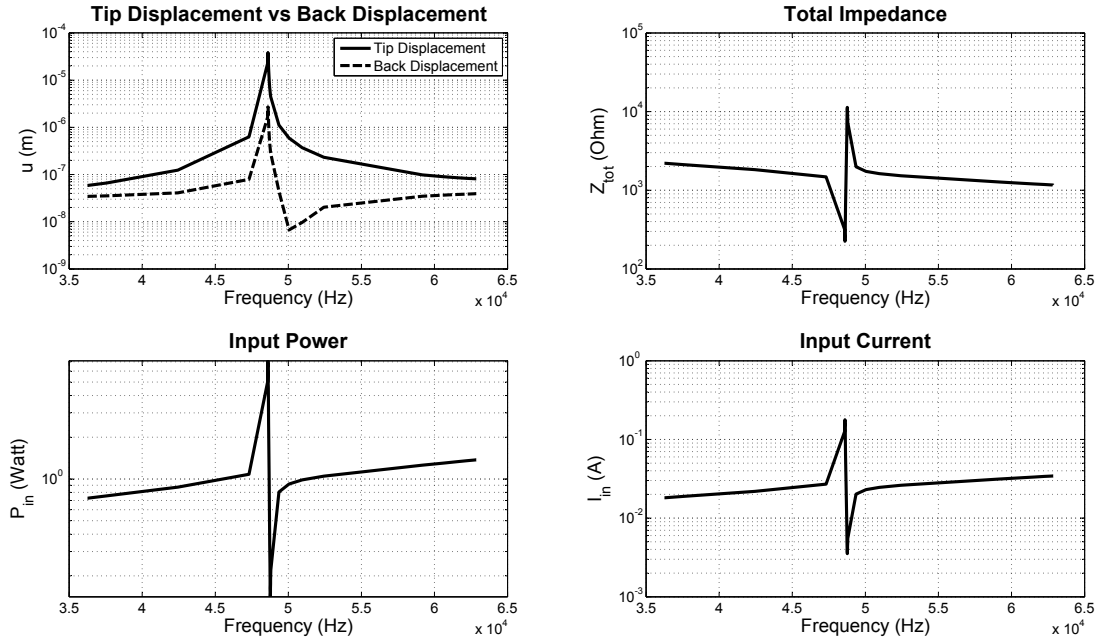


Figure 4.5: Performance criteria of the optimal designed actuator.

## 4.7 Conclusions

The systematic optimal design of a miniaturized ultrasonic scalpel with a stepped horn profile has been described in this work. Starting from the general structure of a Langevin piezoelectric actuator, an equivalent circuit model was employed to reformulate the problem in the non-dimensional space, thus reducing the number of design variables. A constrained multi-objective optimization problem was then established to design a miniaturized ultrasonic scalpel. Using a genetic algorithm, Pareto optimal solutions of such optimization problem were sought and the optimal design of one case study was demonstrated. Finite element analysis was then utilized to evaluate the performance of the optimal design. Good agreement was observed among the results obtained by the two methods. It was shown that using the Mason equivalent circuit model, optimization of Langevin piezoelectric actuators can be performed in non-dimensional space, i.e., any length, any working frequency, any transducer cross section or any number of piezoelectric rings can be selected within the obtained results. The performance of the optimal design, however, must be evaluated by means of finite element analysis, due to the inherent limitations of the equivalent circuit

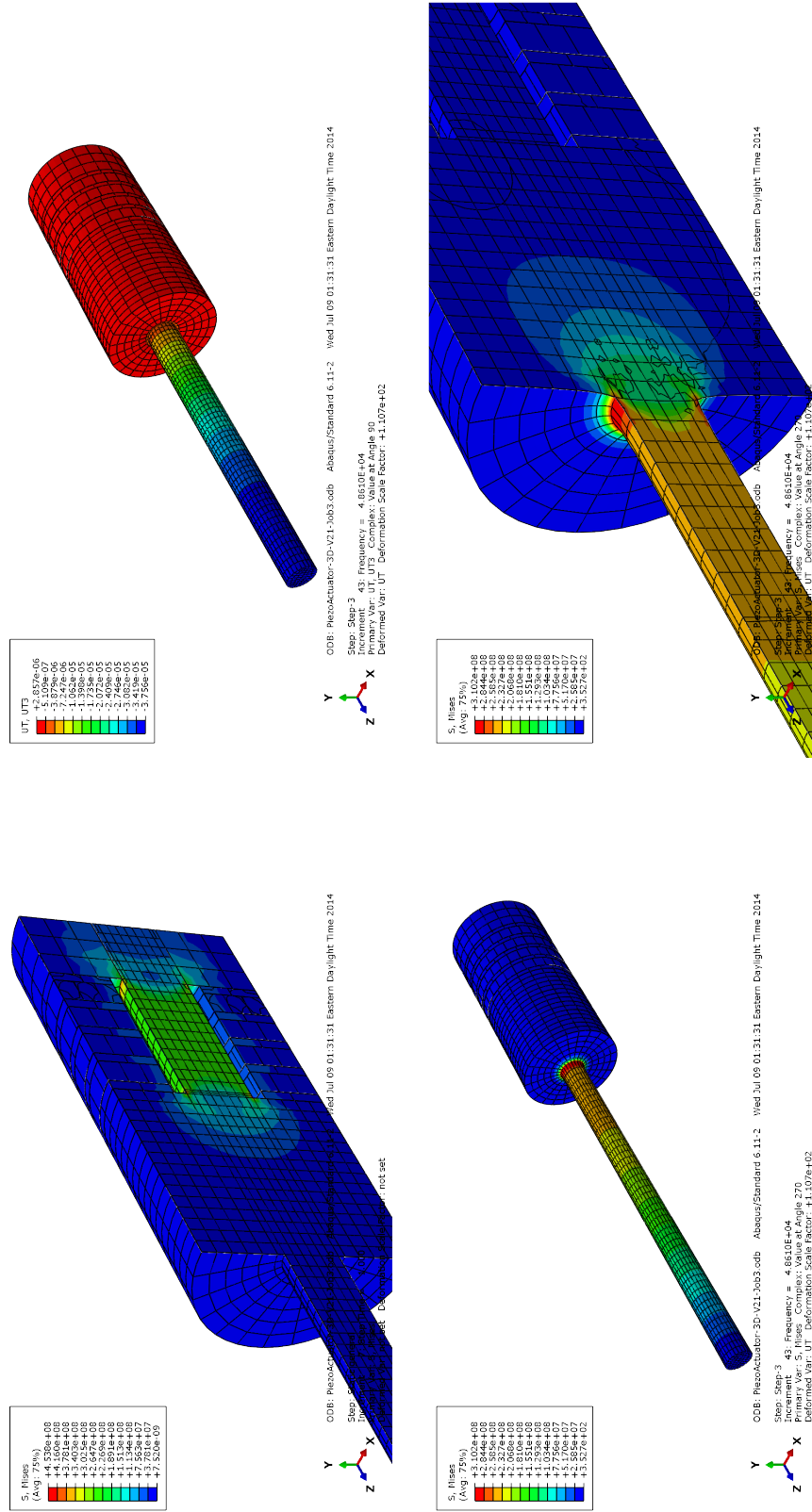


Figure 4.6: FE analysis of the optimal design actuator: (top-left) prestressing step, (top-right) vibration amplitude along the transducer at resonance, (bottom-left) von Mises stress distribution within the transducer at resonance, (bottom-right) a closer view of the stress concentration effect at the step section.

theory.

## References

- [1] V. K. Astashev, K. Khusnutdinova, and V. Babitsky, *Ultrasonic processes and machines: dynamics, control and applications*, Springer, 2007.
- [2] B. J. O'Daly, E. Morris, G. P. Gavin, J. M. O'Byrne, and G. B. McGuinness, "High-power low-frequency ultrasound: A review of tissue dissection and ablation in medicine and surgery," *Journal of Materials Processing Technology*, vol. 200, no. 1, pp. 38–58, 2008.
- [3] B. Fu, T. Hemsel, and J. Wallaschek, "Piezoelectric transducer design via multiobjective optimization," *Ultrasonics*, vol. 44, pp. e747–e752, 2006.
- [4] W. P. Mason, *Electromechanical transducers and wave filters*, D. Van Nostrand Co., 1948.
- [5] E. Eisner, "The design of resonant vibrators," *Physical Acoustics: Principles and Methods*, vol. 1, pp. 353–368, 1964.
- [6] T. Li, Y. Chen, and J. Ma, "Frequency dependence of piezoelectric vibration velocity," *Sensors and Actuators A: Physical*, vol. 138, no. 2, pp. 404–410, 2007.
- [7] L. Merkulov, "Design of ultrasonic concentrators," *Soviet Physics Acoustics*, vol. 3, pp. 246–255, 1957.
- [8] L. Merkulov and A. Kharitonov, "Theory and analysis of sectional concentrators," *Soviet Physics Acoustics*, vol. 5, pp. 183–190, 1959.
- [9] R. Krimholtz, D. A. Leedom, and G. L. Matthaei, "New equivalent circuits for elementary piezoelectric transducers," *Electronics Letters*, vol. 6, no. 13, pp. 398–399, 1970.



- [10] M. O'Donnell, L. Busse, and J. Miller, "1. piezoelectric transducers," in *Ultrasonics*, ser. Methods in Experimental Physics, P. D. Edmonds, Ed. Academic Press, 1981, vol. 19, pp. 29 – 65.
- [11] S. Sherrit, S. P. Leary, B. P. Dolgin, and Y. Bar-Cohen, "Comparison of the mason and klm equivalent circuits for piezoelectric resonators in the thickness mode," in *IEEE Ultrasonics Symposium*, vol. 2, IEEE, 1999, pp. 921–926.
- [12] S. Sherrit, B. P. Dolgin, Y. Bar-Cohen, D. Pal, J. Kroh, and T. Peterson, "Modeling of horns for sonic/ultrasonic applications," in *IEEE Ultrasonics Symposium*, vol. 1, IEEE, 1999, pp. 647–651.
- [13] G. E. Martin, "On the theory of segmented electromechanical systems," *The Journal of the Acoustical Society of America*, vol. 36, no. 7, pp. 1366–1370, 1964.
- [14] T. Li, Y. Chen, and J. Ma, "Development of a miniaturized piezoelectric ultrasonic transducer," *IEEE Transactions on Ultrasonics, Ferroelectrics and Frequency Control*, vol. 56, no. 3, pp. 649–659, 2009.
- [15] R. Holland, "Representation of dielectric, elastic, and piezoelectric losses by complex coefficients," *IEEE Transactions on Sonics and Ultrasonics*, vol. 14, no. 1, pp. 18–20, 1967.
- [16] H. D. Al-Budairi, "Design and analysis of ultrasonic horns operating in longitudinal and torsional vibration," Ph.D. dissertation, University of Glasgow, 2012.
- [17] B. Fu, "Piezoelectric actuator design via multiobjective optimization methods," Ph.D. dissertation, University of Paderborn, 2005.
- [18] Y. Shen, M. Nakajima, S. Kojima, M. Homma, Y. Ode, and T. Fukuda, "Characterization of oscillating nano knife for single cell cutting by nanorobotic manipulation system inside esem," in *IEEE International Conference on Robotics and Automation (ICRA)*, IEEE, 2011, pp. 4133–4138.

- [19] L. Chen, C. Ru, W. Rong, Y. Liu, and L. Sun, “Design, modeling and control of a piezoelectric ultrasonic microdissection technique for the molecular analysis of tissue,” *Smart Materials and Structures*, vol. 19, no. 2, p. 025003, 2010.
- [20] J. F. Amaral, “The experimental development of an ultrasonically activated scalpel for laparoscopic use,” *Surgical Laparoscopy Endoscopy & Percutaneous Techniques*, vol. 4, no. 2, pp. 92–99, 1994.
- [21] J. Amaral, “Ultrasound for cutting and coagulating tissue,” *Problems in General Surgery*, vol. 19, no. 2, pp. 47–59, 2002.
- [22] G. Ogura, R. Nakamura, Y. Muragaki, M. Hashizume, and H. Iseki, “Development of an articulating ultrasonically activated device for laparoscopic surgery,” *Surgical endoscopy*, vol. 23, no. 9, pp. 2138–2142, 2009.
- [23] P. D. Edmonds and F. Dunn, “0. introduction: Physical description of ultrasonic fields,” in *Ultrasonics*, ser. Methods in Experimental Physics, P. D. Edmonds, Ed. Academic Press, 1981, vol. 19, pp. 1 – 28.
- [24] G. Nader, E. C. N. Silva, and J. C. Adamowski, “Effective damping value of piezoelectric transducer determined by experimental techniques and numerical analysis,” in *ABCM Symposium Series in Mechatronics*, vol. 1, 2004, pp. 271–279.
- [25] H. Al-Budairi, M. Lucas, and P. Harkness, “A design approach for longitudinal–torsional ultrasonic transducers,” *Sensors and Actuators A: Physical*, vol. 198, pp. 99–106, 2013.
- [26] K. Deb, *Multi-objective optimization using evolutionary algorithms*. John Wiley & Sons, 2001, vol. 16.

# Chapter 5

## Systematic Optimal Design of an Ultrasonic Horn Profile

### 5.1 Introduction

High-power low frequency ultrasonic vibration has been shown to effectively cut and/or coagulate soft tissue. The required ultrasonic vibration amplitude for tissue fragmentation is, however, different for various tissue textures and ranges from 20  $\mu\text{m}$  in vascular occlusion therapy to about 300  $\mu\text{m}$  in neurosurgery and spinal surgery [1].

Traditionally, Langevin transducers consist of a vibration generator attached to a vibration amplifier (horn) and a blade, all tuned to resonate at a certain ultrasonic frequency. While miniaturizing the Langevin transducers may enhance their flexibility and efficiency, proper design of the horn profile is the bottleneck of such miniaturization. Various ultrasonic horn profiles have been investigated and developed by many researchers over the past 60 years. Analytical approaches have been extensively employed to analyze and design several generic profiles such as conical, exponential, catenoidal, cosine, stepped [2–4] and Gaussian [5], where 1 or 2 parameters are enough to control the shape of the profile (considering known length and end-surface diameters). Should the geometry of the horn profile become more complex, finding a closed-form solution would be unlikely.

---

This chapter contains material published in Iman Khalaji, Rajni V. Patel, and Michael D. Naish, “Systematic design of an ultrasonic horn profile for high displacement amplification,” in *Proceedings of 4th IEEE RAS & EMBS International Conference on Biomedical Robotics and Biomechatronics (BioRob)*, 2012, pp. 913–918.

Structural shape optimization using finite element analysis, on the other hand, has been shown to be more practical in constraint optimization of complex geometries. There is, however, always a trade-off between the number of design variables and complexity of the model. Therefore, it is inefficient to consider finite element nodes as the design variables, as this leads to a jagged and irregular boundary. Alternatively, low-order splines, i.e., nonuniform rational B-splines (NURBS), can be employed for shape parametrization in structural optimization [6]. This leads to fewer design variables and the optimization procedure can be directly linked to a computer aided design (CAD) system.

The recent advent of NURBS-based isogeometric analysis [7] has made it even more beneficial to perform structural optimization using NURBS-based shape parametrization, since both the geometry and the physical field are directly related to the control points. Moreover, easily controlled continuity ( $C^n$  continuity) and exact geometry representation, as well as a fewer number of NURBS-based elements (patches) make isogeometric shape optimization superior over traditional FE-based optimization [8,9]. There is, however, always a problem associated with structural optimization using either finite element or isogeometric analysis, as they are case dependent. In other words, when using finite element method, all of the governing differential equations are always solved in the physical domain and therefore the obtained results cannot be generalized to other similar cases.

Recently, Wang et al. [10] developed a cubic Bezier curve horn profile with high displacement amplitude. They employed a multi-objective genetic algorithm to maximize the displacement amplification of the profile at a particular ultrasonic working frequency. Although the resulting profile exhibits high displacement amplification (about 60% of an equivalent stepped horn) and low stress distribution along the horn, the design is semi-optimal with respect to two predetermined conflicting factors, i.e., the working frequency and the length. Moreover, should a new working frequency and/or dimension be required, a new optimization procedure must be performed, which may lead to a dissimilar geometry.

In this work, a new robust analytical-numerical technique is proposed to design spline-based horn profiles. Starting from the 1-D equation of the longitudinal wave

propagation in a bar, a normalized ordinary differential equation (ODE) based on spline basis functions will be obtained. Using a two-stage optimization scheme, the geometry of the profile will then be updated while the resulting ODE is numerically solved at each iteration. The obtained normalized optimum result can then be applied to any length or working frequency. Bezier, rational Bezier, B-spline and NURBS profiles are used to illustrate the capabilities of the approach. Finite element analyses are then carried out to evaluate the mechanical properties of the resulting designs.

## 5.2 Introduction to NURBS

This section provides a very brief introduction to NURBS geometry. It introduces some notation that will be used in deriving the governing ODE in the following sections. For more details, refer to [11].

A  $p$ th-degree NURBS curve is defined by

$$\mathbf{C}(\zeta) = \frac{\sum_{i=0}^n N_{i,p}(\zeta) w_i \mathbf{P}_i}{\sum_{i=0}^n N_{i,p}(\zeta) w_i} \quad 0 \leq \zeta \leq 1, \quad (5.1)$$

where  $\{\mathbf{P}_i\}$  are the control points,  $\{w_i\}$  are the positive weights, and  $\{N_{i,p}(\zeta)\}$  are the  $p$ th-degree B-spline basis functions defined on the nonuniform knot vector

$$\Xi = \{\underbrace{0, \dots, 0}_{p+1}, \zeta_{p+1}, \dots, \zeta_{m-p-1}, \underbrace{1, \dots, 1}_{p+1}\}. \quad (5.2)$$

The  $i$ -th B-spline basis function can be defined recursively:

$$N_{i,0}(\zeta) = \begin{cases} 1 & \text{if } \zeta_i \leq \zeta \leq \zeta_{i+1} \\ 0 & \text{otherwise} \end{cases}$$

$$N_{i,p}(\zeta) = \frac{\zeta - \zeta_i}{\zeta_{i+p} - \zeta_i} N_{i,p-1}(\zeta) + \frac{\zeta_{i+p+1} - \zeta}{\zeta_{i+p+1} - \zeta_{i+1}} N_{i+1,p-1}(\zeta).$$

Setting

$$B_{i,p}(\zeta) = \frac{N_{i,p}(\zeta)w_i}{\sum_{j=0}^n N_{j,p}(\zeta)w_j} \quad (5.3)$$

enables us to rewrite (5.1) as:

$$\mathbf{C}(\zeta) = \sum_{i=0}^n B_{i,p}(\zeta)\mathbf{P}_i. \quad (5.4)$$

$\{B_{i,p}(\zeta)\}$  are the rational basis functions on  $0 \leq \zeta \leq 1$ . A number of important properties of  $B_{i,p}(\zeta)$  that will be used in the following sections are [11]:

**P.1** Partition of unity:  $\sum_{i=0}^n B_{i,p}(\zeta) = 1$  for all  $\zeta \in [0, 1]$ ;

**P.2**  $\mathbf{C}(0) = \mathbf{P}_0$  and  $\mathbf{C}(1) = \mathbf{P}_n$ ;

**P.3** Strong convex hull property: if  $\zeta \in [u_i, u_{i+1})$ , then  $\mathbf{C}(\zeta)$  lies within the convex hull of the control points  $\mathbf{P}_{i-p}, \dots, \mathbf{P}_i$ ;

**P.4**  $\mathbf{C}(\zeta)$  is infinitely differentiable on the interior of the knot spans and is  $p - k$  times differentiable at a knot of multiplicity  $k$ ;

**P.5** For any  $a \neq 0$ , if  $w_i = a$  for all  $i$ , then  $B_{i,p}(\zeta) = N_{i,p}(\zeta)$ ;

**P.6** A NURBS curve with no interior knots is a rational Bezier curve. This, together with **P.5**, implies that B-splines and rational and nonrational Bezier curves are special cases of NURBS curves;

**P.7** Local approximation: if the control point  $\mathbf{P}_i$  is moved, or the weight  $w_i$  is changed, it affects only the portion of the curve on the interval  $\zeta \in [\zeta_i, \zeta_{i+p+1})$ .

## 5.3 Horn Design

### 5.3.1 Longitudinal Wave Propagation

Consider a bar with length  $l$  and cross-section  $S_x = S(x)$ . Let  $a(x, t)$  represent the displacement of the cross-section  $x$  from its position. Consider a harmonic force  $F(t) = F_0 e^{j\omega t}$  applied to the bar at  $x = 0$ . As a result, a harmonic vibration will be

generated along the bar:

$$a(x, t) = \tilde{u}_x e^{j\omega t} = u_x e^{j(\omega t + \phi_x)}. \quad (5.5)$$

Here,  $\tilde{u}_x = \tilde{u}(x)$  is the complex amplitude, and  $u_x$  and  $\phi_x$  are the amplitude and the phase, respectively. Considering an isotropic material with small internal damping, the complex modulus of elasticity can be described as:

$$\tilde{E} = E \left( 1 + j \frac{\psi}{2\pi} \right), \quad (5.6)$$

where  $E$  is the Young's modulus and  $\psi$  is the coefficient of absorption, which characterizes the internal friction of the material [4].

The equation of 1-dimensional longitudinal wave propagation within a tapered rod is:

$$\frac{\partial}{\partial x} \left[ \tilde{E} S_x \frac{\partial a(x, t)}{\partial x} \right] = \rho S_x \frac{\partial^2 a(x, t)}{\partial t^2}, \quad (5.7)$$

where  $\rho$  is the density of the material. Substituting (5.5) into (5.7) gives a time-invariant equation:

$$\tilde{E} \left[ \tilde{u}_x'' + \frac{S_x'}{S_x} \tilde{u}_x' \right] + \rho \omega^2 \tilde{u}_x = 0. \quad (5.8)$$

Note that in deriving (5.7), it is assumed that the vibrating system is linear and stationary. Now, consider an arrangement where one of the bar's ends is free (no strain) and the other end is subjected to a harmonic force  $F(t) = F_0 e^{j\omega t}$ . Therefore, the Neumann boundary conditions are:

$$\tilde{u}_x'|_{x=l} = 0, \tilde{E} S_0 \tilde{u}_x'|_{x=0} = -F_0. \quad (5.9)$$

Equation (5.8) together with (5.9) determines the governing differential equation of the vibration within a rod. The final solution to this two-point boundary value problem depends on the waveguide's form and is determined by the cross-sectional function  $S_x$ . The closed form solution to this problem is provided for several typical profiles in the literature [2–5].

### 5.3.2 NURBS-based Horn Profile

Now consider an axisymmetric NURBS-based horn profile whose geometry is described by (5.4). Knowing all of the control points  $\mathbf{P}_i$  and the weights  $w_i$ , it is desired to solve (5.8) for the complex amplitude  $\tilde{u}_x$ . Once the solution is known, an optimization scheme can be used to maximize the displacement amplification coefficient  $K = \frac{u_l}{u_0}$  and find the optimal values of  $\mathbf{P}_i$ ,  $w_i$ ,  $l$  and  $\omega$ .

We speculate that a NURBS profile satisfies most of the requirements for a smooth and high displacement amplification horn:

- In order to avoid stress concentrations in a vibrating bar, the ratio  $\frac{S'_x}{S_x}$  in (5.8) must exist and be bounded. Therefore,  $S_x$  should be at least  $C^1$  continuous. On the other hand, according to **P.4**, a NURBS curve is at least  $C^{p-k}$  continuous at a knot of multiplicity  $k$ . Therefore, as long as  $p > k + 1$ , there would be no stress concentrations within the bar\*.
- The strong convex hull property of a NURBS curve (**P.3**) confines the horn profile within the design space. In other words, the horn profile will always stay inside the design space as long as the control points lie within the same space.
- The local approximation property of a NURBS curve (**P.7**) helps in optimization of the profile, where adjusting the control point  $\mathbf{P}_i$  or the weight  $w_i$  only affects the curve locally.
- For a specified  $S_0$  and  $S_l$ , the first and the last control points will be fixed at  $\mathbf{P}_0$  and  $\mathbf{P}_l$ , respectively. This follows directly from **P.2**.

Under these assumptions, an explicit equation for  $S_x$  must be derived to be used in (5.8). This approach is, however, infeasible as it involves tedious mathematical analyses. Alternatively, (5.8) can be slightly altered to suit our speculation.

---

\* It will be shown later that in fact  $p \geq k + 2$ , since the NURBS curve must be at least  $C^2$  continuous to avoid singularities in the normalized wave equation in (5.14).



### 5.3.3 Longitudinal Wave Equation Revisited

Assuming a  $p$ th-degree NURBS curve as an axisymmetric horn profile, the  $x$  and  $r$ -components of the curve can be written using (5.4) as:

$$\begin{aligned} x(\zeta) &= \sum_{i=0}^n B_{i,p}(\zeta) x_i \\ r(\zeta) &= \sum_{i=0}^n B_{i,p}(\zeta) r_i, \end{aligned} \quad (5.10)$$

where

$$\mathbf{P}_i = \{x_i, r_i\}$$

is the  $i$ th control point. A normalized form of (5.10) can also be derived using property **P.1**:

$$\begin{aligned} X(\zeta) &= \frac{x(\zeta) - x_0}{x_n - x_0} = \sum_{i=0}^n B_{i,p}(\zeta) X_i \\ R(\zeta) &= \frac{r(\zeta) - r_n}{r_0 - r_n} = \sum_{i=0}^n B_{i,p}(\zeta) R_i, \end{aligned} \quad (5.11)$$

where

$$\mathbf{Q}_i = \begin{Bmatrix} X_i \\ R_i \end{Bmatrix} = \begin{Bmatrix} \frac{x_i - x_0}{x_n - x_0} \\ \frac{r_i - r_n}{r_0 - r_n} \end{Bmatrix} \quad (5.12)$$

is the  $i$ th normalized control point. Note that in deriving (5.11) it was assumed that the cross-sectional ratio  $\frac{S_0}{S_l} > 1$  is specified and therefore:

$$\begin{aligned} 0 &= X_0 \leq X_1, \dots, X_{n-1} \leq X_n = 1 \\ 1 &= R_0 \geq R_1, \dots, R_{n-1} \geq R_n = 0. \end{aligned}$$

Equation (5.8) can also be described in a nondimensional form by defining:

$$l = x_n - x_0 = \text{length of the rod} \quad (5.13a)$$

$$\tilde{U}(\zeta) = \frac{\tilde{u}(x(\zeta))}{l} \quad (5.13b)$$

$$b = \frac{r_n}{r_0 - r_n} \quad (5.13c)$$

$$\lambda = j\omega l \sqrt{\frac{\rho}{\tilde{E}}} = \frac{j\omega l}{c\sqrt{1 + j\psi/2\pi}}, \quad (5.13d)$$

where  $c$  is the wave speed within the waveguide. The normalized wave equation within the horn can then be derived as (Appendix B):

$$\tilde{U}_\zeta'' + \tilde{U}_\zeta' \left( \frac{2R'_\zeta}{R_\zeta + b} - \frac{X''_\zeta}{X'_\zeta} \right) - \lambda^2 (X'_\zeta)^2 \tilde{U}_\zeta = 0, \quad (5.14)$$

$$\tilde{U}'_\zeta|_{\zeta=1} = 0, \tilde{U}'_\zeta|_{\zeta=0} = -\frac{F_0}{\tilde{E}S_0} X'_\zeta|_{\zeta=0} = -\tilde{\varepsilon}_0 X'_\zeta|_{\zeta=0},$$

where  $R_\zeta = R(\zeta)$  and  $X_\zeta = X(\zeta)$  are the  $r$  and  $x$  components of the normalized NURBS curve in (5.11) and  $\tilde{\varepsilon}_0 = \tilde{\varepsilon}(0)$  is the complex strain caused by  $F_0$  at the input. It is worth mentioning that although (5.14) is derived for a NURBS-based profile, its use is not limited to such curves.

### 5.3.4 Solving the Normalized Wave Equation

Ultrasonic horns are usually made of low damping materials in order to minimize energy waste and maximize the power transferred between the blade and the specimen under action. It is, therefore, safe to assume that the absorption coefficient  $\psi$  is small ( $\psi \ll 1$ ). Expanding the expression in (5.6) using small power series and neglecting the higher order terms, (5.13d) becomes:

$$\lambda = \left( j + \frac{\psi}{4\pi} \right) \frac{\omega l}{c}. \quad (5.15)$$

Neither (5.8) nor (5.14) are analytically solvable in their general forms. Numer-

ical solutions can, however, be sought provided that all of the parameters are known. For a system close to resonance and under the assumption of small dissipation levels, the solution to (5.14) can be written in the form [4],

$$\tilde{U}(\zeta) = \varepsilon_0 [T(\zeta) + jW(\zeta)], \quad (5.16)$$

where  $\varepsilon_0$  is the input strain amplitude and  $T(\zeta)$  and  $W(\zeta)$  characterize the elastic and dissipative properties of the vibration system, respectively. At certain  $\lambda(\omega_n, l_n) = \lambda^*$ , the system will vibrate at its first longitudinal mode shape (two antinodes at both ends, one node in between), and hence,  $T^*(0)$  and  $T^*(1)$  will be maximized with opposite signs.

Putting (5.15) and (5.16) back into (5.14), a system of two coupled ordinary differential equations and four boundary conditions will be obtained. Numerical boundary value problem algorithm can then be used to solve this system of ODEs.

### 5.3.5 Optimization Scheme

Assuming a  $p$ th-degree NURBS curve with  $n$  control points, a knot vector is chosen as in (5.2). For simplicity and to make the optimization process more stable, knot values are not considered as design variables. The profile of the horn is optimized by allowing the normalized control points  $Q_i$  to move within the design space enclosed by the dashed square in Fig. 5.1. In the case of a rational Bezier or NURBS curve, the weights  $w_i$  will also be considered as design variables during the optimization process.

In order to avoid singularities in (5.14) and to make the resulting horn profile realistic, additional constraints must be considered during the optimization procedure:

$$X'(\zeta) > 0 \quad \forall \zeta \in [0, 1] \quad (5.17a)$$

$$R'(\zeta) < 0 \quad \forall \zeta \in [0, 1]. \quad (5.17b)$$

Equation (5.17b) ensures that no wavy profile will be generated during the

process.

As the horn profile evolves during the optimization process,  $\lambda$  must be changed to put the system back into resonance. For this reason, a two-stage optimization procedure must be iterated upon. In the first step, a multi-variable optimization scheme is used to find the optimum horn profile by adjusting the normalized control points  $\mathbf{Q}_i$  and weights  $w_i$ . In the second step, the corresponding  $\lambda^*$  is determined using a single variable optimization scheme and the optimization procedure restarts with this new value for  $\lambda^*$ . The optimization stops when no change is observed in  $\mathbf{Q}_i^*$ ,  $w_i^*$  and  $\lambda^*$ .

The only constant parameter that must be specified in (5.14) is  $b$ , which is directly related to the cross-sectional ratio of the input to the output:

$$\frac{S_0}{S_l} = \left(\frac{r_0}{r_l}\right)^2 = (1 + b)^2. \quad (5.18)$$

While  $b$  depends on the horn's geometric constraints,  $\psi$  and  $\varepsilon_0$  can be chosen arbitrarily, since the displacement amplification factor is independent of the material [4] and the actuator interaction. They must, however, be small enough to avoid violating the assumptions made earlier.

The following outlines the constraint optimization procedure employed in this work:

1. Initialization: considering predetermined values for  $b$ ,  $\psi$  and  $\varepsilon_0$ , choose some initial values for  $\mathbf{Q}_i^0$ ,  $w_i^0$  and  $\lambda^0$ . In order to accelerate the optimization process, the initial values must be feasible; i.e., the initial values should satisfy all of the constraints.
2. Set the current values of the parameters:

$$\begin{aligned} \mathbf{Q}_i^{\text{cur}} &= \mathbf{Q}_i^0 \\ w_i^{\text{cur}} &= w_i^0 \\ \lambda^{\text{cur}} &= \lambda^0. \end{aligned}$$

3. First stage constraint multi-variable optimization: (5.14) is solved at each

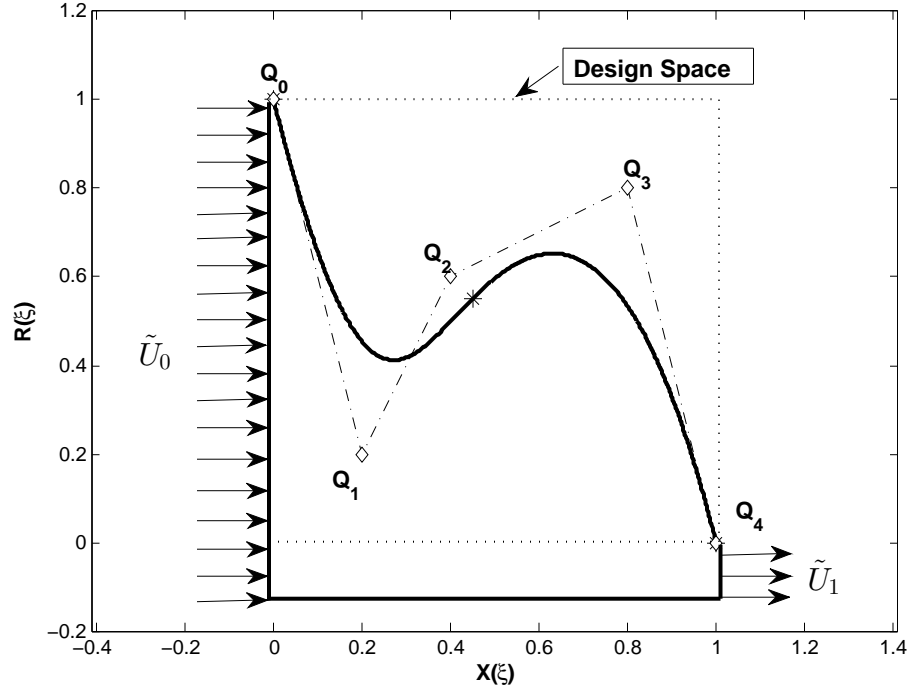


Figure 5.1: A normalized NURBS-based horn profile in the design space.  $\{Q_0, \dots, Q_4\}$  are the normalized control points.

optimization iteration to find the optimum horn profile:

$$\underset{Q_i, w_i}{\text{minimize}} \left| \frac{T_0}{T_1} \right| \text{ s.t. } \begin{cases} 0 \leq X_i \leq 1 & i = 1, \dots, n-1 \\ 0 \leq R_i \leq 1 & i = 1, \dots, n-1 \\ 0 \leq w_i \leq w_{\text{ub}} & i = 0, \dots, n \\ X'(\zeta) > 0 & 0 \leq \zeta \leq 1 \\ R'(\zeta) < 0 & 0 \leq \zeta \leq 1, \end{cases}$$

where  $w_{\text{ub}}$  is an arbitrary upper bound for the weights. Update the current values of  $Q_i^{\text{cur}}$  and  $w_i^{\text{cur}}$ :

$$\begin{aligned} Q_i^{\text{cur}} &= Q_i^* \\ w_i^{\text{cur}} &= w_i^*. \end{aligned}$$

4. Second stage single-variable optimization: calculating the optimum horn profile, (5.14) is once again solved at each optimization iteration to find the cor-

responding resonant  $\lambda^*$ ,

$$\underset{\lambda}{\text{minimize}} \left| \frac{1}{T_1 - T_0} \right|.$$

Note that, the subtraction operator in this equation ensures that  $T(1)$  and  $T(0)$  have opposite signs; i.e., the system is at its first mode of vibration. Update the value of  $\lambda^{\text{cur}}$ :

$$\lambda^{\text{cur}} = \lambda^*$$

5. Stopping criteria: If  $\mathbf{Q}_i^{\text{cur}}$ ,  $w_i^{\text{cur}}$  and  $\lambda^{\text{cur}}$  have not been changed from their previous values, terminate the process; otherwise go to Step 3.

## 5.4 Analyses

### 5.4.1 Optimization Results

In this section, the optimum horn profiles that are obtained using the proposed approach are presented. Starting from a Bezier curve, it will be shown that a slightly higher amplification can be obtained compared to [10]. Switching to rational Bezier curves, the optimum amplification factor improves further. As B-spline profiles come into play, higher amplification will be achieved at the expense of higher strain values. Finally, it will be shown that a NURBS curve converges safely to a stepped horn with an amplification factor close to that of a stepped horn.

The Sequential Quadratic Programming (SQP) algorithm is utilized to perform the two-stage optimization process in Matlab. As the gradient vectors and Hessian matrices of the objective functions are almost impossible to calculate, Matlab uses finite difference to estimate them. Nonconvexity of the objective functions will also cause the problem to have local minima. Therefore, in each case, various initial values will be used to find several local minima. The optimization results of each profile are tabulated in Table 5.1.

#### 5.4.1.1 Bezier profile

Four normalized control points  $\{\mathbf{Q}_0, \mathbf{Q}_1, \mathbf{Q}_2, \mathbf{Q}_3\}$  are used to construct a 3-degree Bezier profile horn. Considering  $\frac{S_0}{S_l} = 16$ , the optimization process is repeated for different initial values of  $\mathbf{Q}_1$  and  $\mathbf{Q}_2$  ( $\mathbf{Q}_0 = \{0, 1\}$  and  $\mathbf{Q}_3 = \{1, 0\}$  are fixed). The amplification factor of the obtained optimized profiles ranges from 10.88 to 11.55 (Table 5.1) which is greater than 10.5, as reported in [10]. As mentioned earlier, the main limitation of Wang's work [10] is the choice of a fixed working frequency and a fixed length, which makes their result suboptimal.

#### 5.4.1.2 Rational Bezier profile

In addition to the normalized control points, their corresponding weights  $w_i$  can also be considered among the design variables. The resulting profile is now called a rational Bezier curve. The main advantage of rational Bezier curves over Bezier curves is their ability to exactly approximate conic sections. A 3-degree rational Bezier curve is formed using four normalized control points. Considering all of the unknown parameters  $\{\mathbf{Q}_1, \mathbf{Q}_2, w_0, w_1, w_2, w_3\}$  as the design variables, several local minima are sought using different initial values. The obtained amplification factors range from 10.21 to 11.05 which are less than the amplification range of the Bezier curves obtained earlier. In order to make the optimization procedure more robust, the values of  $\{\mathbf{Q}_1, \mathbf{Q}_2\}$  were kept constant at the optimum results obtained earlier and the weights were considered as the only design parameters. Under this assumption, the new amplification factor reached to the value of 12.12. A summary of the results obtained at this stage is reported in Table 5.1. In addition, Fig. 5.2 shows an example of an optimum rational Bezier profile obtained using the optimization procedure.

#### 5.4.1.3 B-spline profile

In order to have a 3-degree B-spline curve, at least 5 control points are required. Choosing a constant knot vector  $\Xi = \{0, 0, 0, 0, 0.5, 1, 1, 1, 1\}$ , three normalized control points, i.e.,  $\{\mathbf{Q}_1, \mathbf{Q}_2, \mathbf{Q}_3\}$  need to be adjusted using the optimization procedure. Various local minima are obtained for the optimization problem where the amplifica-

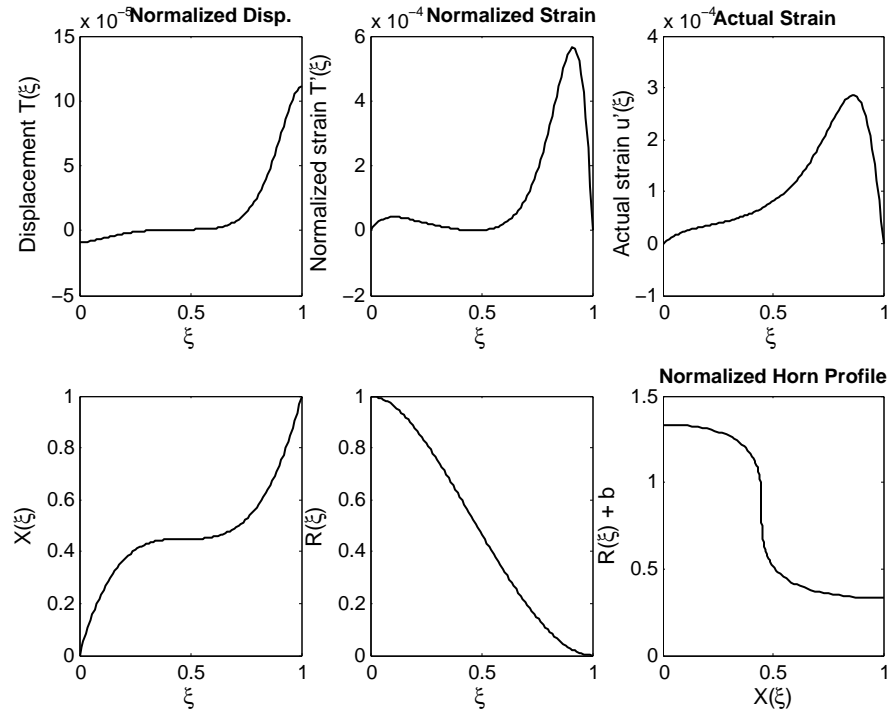


Figure 5.2: An optimized rational Bezier horn profile (bottom-right) along with its associated curves, i.e., displacement distribution (top-left), strain (top-right) and  $X$  and  $R$  components (bottom-left, bottom-centre).



tion factor varies between 11.48 to 13.55. Table 5.1 summarizes the results obtained using the B-spline profile.

#### 5.4.1.4 NURBS profile

Including control point weights  $\{w_0, w_1, w_2, w_3, w_4\}$  into the 3-degree B-spline curve leads to a NURBS curve. Similar to the rational Bezier curves, two optimization trials are sought here: 1. optimization of all unknown parameters and 2. optimization of the weights solely. As is shown in Figure 5.3, the resulting optimized profile in both cases looks much like a stepped horn with an amplification factor close to 16. This, in fact, is true, as the upper bound of the amplification factor of a horn is  $\frac{S_0}{S_l}$  and can be achieved using a stepped horn [4].

### 5.4.2 Finite Element Verification

Obtaining the optimized normalized profiles, the corresponding control points are calculated using (5.11), considering horn size specification in [10]:

$$l = 93 \text{ mm} = \text{length of the horn}$$

$$\frac{S_0}{S_l} = \left(\frac{r_0}{r_l}\right)^2 = \left(\frac{10 \text{ mm}}{2.5 \text{ mm}}\right)^2 = 16.$$

The Solidworks API is then used to construct the associated curve of each profile by directly manipulating the control points, weights and knot vector. The resulting horn profiles are then analyzed within Abaqus. Stainless Steel (SS 41) is chosen for the horn material properties as in [10]. In addition, Rayleigh structural damping ( $\alpha = 0, \beta = 10^{-7}$ ) is also considered to make the responses bounded. 2-D axisymmetric modal analysis is then performed to find the first longitudinal natural frequency and the frequency response function of each profile by considering a sinusoidal forcing function at the base. The amplification factor,  $M$ , and resonance frequency,  $f$ , of each case is then compared to the corresponding values obtained by our method. As can be seen from Table 5.1, very good agreement is obtained among the results from both methods.

The last column in Table 5.1 indicates the ratio between  $\|u_l\|$ , the vibration

Table 5.1: Comparison of the amplification factor,  $M$ , and resonance frequency,  $f$ , of various spline-based horn profiles, obtained from the proposed approach and finite element method

Profile ID	$f_{\text{optimum}}$ (Hz)	$M_{\text{optimum}}$	$f_{\text{FEM}}$ (Hz)	$M_{\text{FEM}}$	$\frac{\ u_l\ }{\varepsilon_{\max}}$ (m)
Bezier #1	30230	10.8759	30580	10.5622	0.0350
Bezier #2	31607	11.47	31233	11.025	0.0362
Bezier #3	30989	11.5471	31386	11.0854	0.0362
Bezier #4	30997	11.5497	31389	11.0874	0.0362
Rational Bezier #1	30347	10.4661	30862	10.3171	0.0371
Rational Bezier #2	33694	10.2121	33854	9.8145	0.0312
Rational Bezier #3	30380	11.0493	30823	10.6688	0.0363
Rational Bezier #4	29637	12.1180	29940	11.6280	0.0370
Rational Bezier #5	27606	11.9716	27932	11.4951	0.0387
B-spline #1	29022	13.55	29189	13.2295	0.0325
B-spline #2	30834	13.0007	31056	12.5359	0.0326
B-spline #3	29816	12.5646	30155	12.1637	0.0329
B-spline #4	31735	11.7430	32031	11.2992	0.0344
B-spline #5	26618	11.4787	26954	11.0565	0.0395
NURBS #1	27361	15.9771	27312	15.5074	0.0267
NURBS #2	28148	15.8663	27002	15.0127	0.0253
Stepped	-	-	26658	15.6324	0.0230

amplitude of the horn at the output, and  $\varepsilon_{\max}$ , the maximum strain observed along the bar. The higher this ratio, the larger the vibration amplitude generated at the output per unit maximum strain along the bar. As long as the system works in the linear regime and the horn has negligible influence on the actuator, this condition holds. This ratio is especially useful when a horn works close to its fatigue strength. This number together with the amplification factor,  $M$ , are in fact, figures of merit for a designed resonator. Since the two metrics are somewhat contradictory, further study is required to consider both metrics in a multi-objective optimization problem and obtain pareto-optimal solutions.

This proves our conjecture that employing spline-based profiles can improve the displacement amplification of ultrasonic horns. The immediate outcome of this finding is that ultrasonic knives can be further miniaturized, as a lower ratio of  $\frac{S_0}{S_l}$  is required to attain the required vibration displacement at the blade tip. In addition, the proposed method introduces a new systematic approach for designing an ultrasonic horn profile. The only design parameter that is required is  $\frac{S_0}{S_l}$  and the method finds the optimum profile and its normalized working frequency. The result can then be adapted for any length or working frequency.

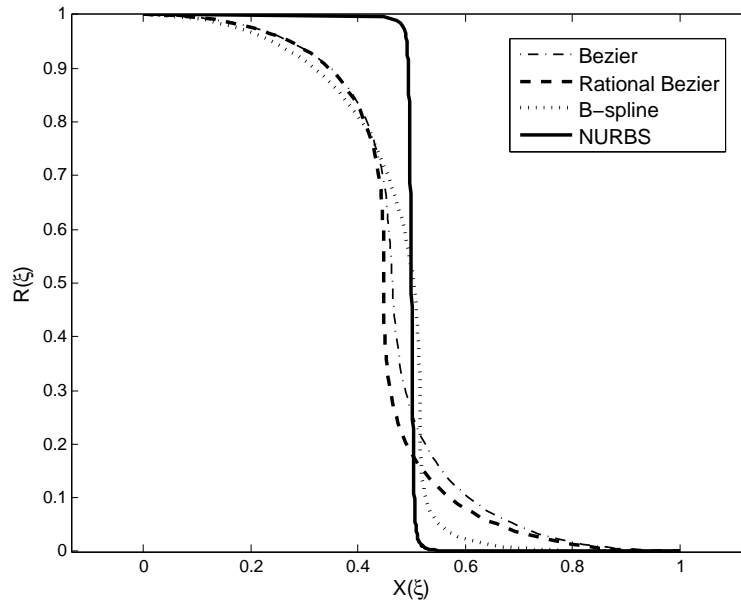


Figure 5.3: Comparison of the optimal curves obtained using the proposed method.

## 5.5 Conclusions

A new analytical-numerical method has been proposed to systematically design a high amplification ultrasonic horn profile. The 1-D wave equation was first normalized in the design space, where the  $x$  and  $r$ -components of the horn profile were assumed to be independent and parametric. Due to the generality of NURBS curves in defining complex geometries and their compact representation, NURBS basis functions were employed to explicitly define the horn profile. A two-stage optimization method was then employed to find the optimum profile that results in the highest displacement amplification ratio. The obtained amplification factor and natural frequencies were verified via finite element analysis.

As the optimization problem of a horn design is nonconvex, there could be many local minima where the algorithm may become trapped. Proper initialization of the design parameters is, therefore, important. It is expected that by employing a global optimization approach such as simulated annealing or a genetic algorithm, a global optimum can be found. It is, however, important to note that there is no unique representation of a certain geometry using NURBS curves. This means that NURBS-based structural optimization problems can have multiple global minima.

## References

- [1] B. J. O'Daly, E. Morris, G. P. Gavin, J. M. O'Byrne, and G. B. McGuinness, "High-power low-frequency ultrasound: A review of tissue dissection and ablation in medicine and surgery," *Journal of Materials Processing Technology*, vol. 200, no. 1, pp. 38–58, 2008.
- [2] L. Merkulov, "Design of ultrasonic concentrators," *Soviet Physics Acoustics*, vol. 3, pp. 246–255, 1957.
- [3] L. Merkulov and A. Kharitonov, "Theory and analysis of sectional concentrators," *Soviet Physics Acoustics*, vol. 5, pp. 183–190, 1959.
- [4] V. K. Astashev, K. Khusnutdinova, and V. Babitsky, *Ultrasonic processes and machines: dynamics, control and applications*. Springer, 2007.
- [5] E. Eisner, "The design of resonant vibrators," *Physical Acoustics: Principles and Methods*, vol. 1, pp. 353–368, 1964.
- [6] P. W. Christensen and A. Klarbring, *An introduction to structural optimization*. Springer, 2008, vol. 153.
- [7] J. A. Cottrell, T. J. Hughes, and Y. Bazilevs, *Isogeometric analysis: toward integration of CAD and FEA*. John Wiley & Sons, 2009.
- [8] W. A. Wall, M. A. Frenzel, and C. Cyron, "Isogeometric structural shape optimization," *Computer Methods in Applied Mechanics and Engineering*, vol. 197, no. 33, pp. 2976–2988, 2008.
- [9] X. Qian, "Full analytical sensitivities in NURBS based isogeometric shape optimization," *Computer Methods in Applied Mechanics and Engineering*, vol. 199, no. 29, pp. 2059–2071, 2010.

- [10] D.-A. Wang, W.-Y. Chuang, K. Hsu, and H.-T. Pham, “Design of a bézier-profile horn for high displacement amplification,” *Ultrasonics*, vol. 51, no. 2, pp. 148–156, 2011.
- [11] L. Piegl and W. Tiller, *The NURBS book*. New York, NY, USA: Springer-Verlag New York, Inc., 1997.

# Chapter 6

## Articulating Minimally Invasive Ultrasonic Tool for Robotics-Assisted Surgery

### 6.1 Introduction

While ultrasonically activated scalpels have demonstrated superior characteristics over electro-cautery devices in coagulation and cutting of soft tissue with more precision and speed, less cutting force, less smoke and reduced collateral damage, several drawbacks such as large size, less flexibility, high power consumption, and high transmission loss have rendered them unattractive for advanced internal body operation, particularly in Robotics-Assisted Minimally Invasive Surgery (RAMIS). In order to address this issue, several researchers [1,2] have tried flexible ultrasonic devices using superelastic Nitinol. Insufficient vibration amplitude, poor fatigue life, high damping capacity and hence, excessive heat generation are among the drawbacks of employing superelastic Nitinol as the waveguide. Ogura *et al.* [3,4] developed a compact MIS ultrasonic scalpel that can be articulated within the patient's body. By moving the vibration source of the transducer to the distal end of the laparoscopic instrument, they were able to orient the ultrasonic scalpel within the desired range. Recently, Timm *et al.* have filed a patent [5] on a RAMIS articulating ultrasonic scalpel. To the best of authors' knowledge, this product is not yet available on the market. A

---

This chapter contains material submitted for publication in Iman Khalaji, Michael D. Naish and Rajni V. Patel, "Articulating Minimally Invasive Ultrasonic Tool for Robotics-Assisted Surgery," submitted to *IEEE International Conference on Robotics and Automation (ICRA)*, 2015.

novel design of an articulating ultrasonic scalpel is designed and developed in this study. The main difference between this work and [3–5] is the novel articulating wrist that decouples all DOFs. In addition, none of this prior work gives any specific details on ultrasonic scalpel optimization.

## 6.2 Related Work

### 6.2.1 Ultrasonically Activated Scalpel

Traditionally, an ultrasonically activated device consists of a vibration generator (often a Langevin piezoceramic) sandwiched between a back mass and a front mass section. Since piezoceramic transducers can only generate a few microns of vibration amplitude (typically 0.1% of their length), the device is tuned to resonate at a certain ultrasonic frequency. Therefore, its overall length must be a half-wavelength or a multiple of the half-wavelength at the driving frequency. A vibration amplifier (horn) is also usually employed as part of the front mass to amplify the delivered vibration amplitude.

Designing a piezoelectric transducer is generally a complicated task, since its overall performance is dependent on many factors, such as dimensions and material properties of various parts, the number of piezoelectric elements, the mode and frequency of driving the system, etc. Depending on the application, multiple objective functions can be defined that are usually contradictory. In [6, 7], a constrained multi-objective optimization problem to optimize a Langevin transducer is formulated and then solved by evolutionary algorithms. Nevertheless, the obtained results are all case dependent, bounded by the assumptions that have been made.

In the first part of this work, the design of a Langevin transducer with a stepped horn profile is presented. In order to minimize the size of the device, the design space has been limited to one half-wavelength in the overall length. Mason equivalent circuit network theory [8] is used to formulate the problem in its general form and determine the interaction between various design parameters. Using two objective functions, i.e., the delivered vibration amplitude and the input power, a Pareto front curve is



obtained and the most optimum solution is sought considering the design constraints. Finally, finite element analysis (FEA) is employed to evaluate the performance of the designed transducer.

## 6.2.2 Articulating Robotics-Assisted Surgical Tool

One benefit of having a robotics-assisted surgical system is to have an articulating surgical tool that can mimic scaled tremor-free motion of a surgeon's hand inside a patient's body. While many articulating wrist mechanisms have been either patented or published, only a few of them have been FDA cleared and commercialized. Examples of such patents, which form the basis for the Intuitive Surgical EndoWrist<sup>®</sup> instruments, include [9–11]. The pitch and yaw DOFs in these cases, however, are coupled and such coupling should be taken into account during robotic manipulation.

Another example of a robotic wrist with decoupled motion transmission is [12], which is being used as the end effector in the RAVEN's surgical instrument (Applied Dexterity, Inc., Seattle, WA). In the second part of this work, the design of a novel 2-DOF surgical end effector (1-DOF pitch, 1-DOF grip) with decoupled motions is presented and analyzed. The proposed design allows the transmission of motion, force and/or torque at various wrist orientations with no coupling, reduced cable pretensioning and hence less friction.

## 6.3 Materials and Methods

### 6.3.1 Ultrasonically Activated Scalpel

As schematically shown in Fig. 6.1, a Langevin ultrasonic transducer can be broken down into three general sections; namely, a high-acoustic-impedance back-mass section, a piezoelectric section, and a low-acoustic-impedance front mass section. Piezoelectric elements are sandwiched between the front and back sections to provide enough pre-compression on the piezoceramic elements and to avoid tensioning them during vibration excitation. Usually an even number of piezoelectric rings, electrically connected in parallel, are used with polling direction along the thickness. A

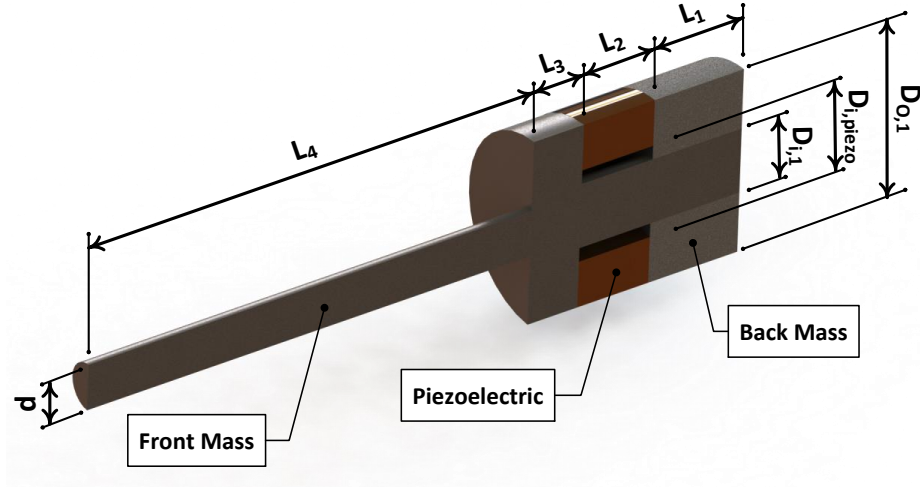


Figure 6.1: Schematic illustration of a Langevin transducer.

sinusoidal voltage or current source is then employed to drive the resulting actuator at a predetermined longitudinal resonance frequency.

#### 6.3.1.1 Equivalent Circuit Network Modelling

Analytical solutions to the 1-dimensional wave equation in piezoelectric transducers are usually difficult to derive. Using transmission line theory, Mason [8] proposed equivalent circuits to model the electrical as well as the mechanical properties of piezoelectric materials in a composite structure. Fig. 6.2 shows the equivalent Mason circuit network model of a half-wavelength piezoelectric transducer with a stepped horn as shown in Fig. 6.1. The transducer is composed of four sections in which Sections 3 and 4 (horn) are titanium cylindrical rods, and Sections 1 and 2 are composite sections made of titanium and steel, and titanium and piezoceramic materials, respectively. Since the mechanical impedance of the piezoelectric stack and steel back mass are roughly one order of magnitude higher than the mechanical impedance of the titanium segment in Sections 1 and 2, it is safe to assume a constant strain at any cross section within Sections 1 and 2. This means acoustic elements in Mason equivalent circuit should be added in series for each Section 1 and 2 [13].

As explained in 4.3,  $\tilde{Z}_f$  and  $\tilde{Z}_b$  in Fig. 6.2 are the complex impedances of the front and back loads being applied to the transducer during its operation. Depending

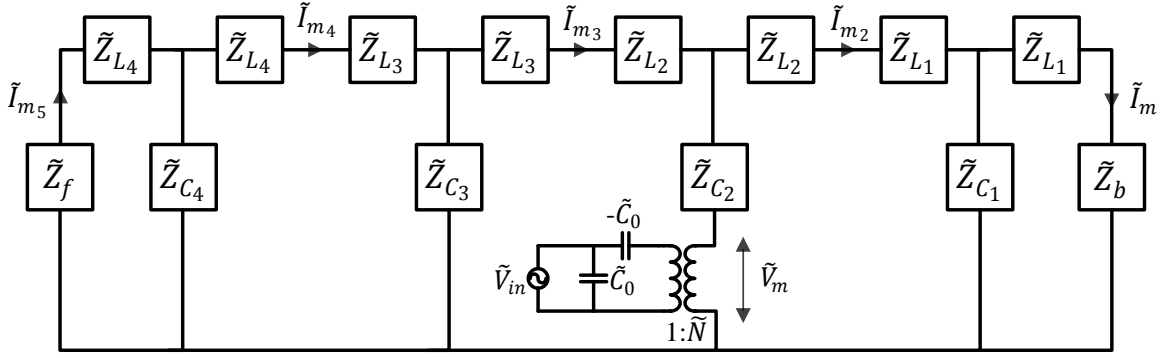


Figure 6.2: Equivalent circuit of a Langevin piezoelectric transducer.

on the application of the transducer, they can be obtained experimentally or through FEA and analytical methods [14]. Moreover, the complex inductive and capacitive impedances, as well as the transformer parameters are given by 4.2–4.17.

Driving the explicit mathematical expressions of the above equations is a tedious task. However, using a symbolic computation engine, such as Maple<sup>TM</sup> (Maple-soft, Waterloo, Canada), one can simplify the above equations and observe the interaction of the design variables on the transducer output performance. Assuming  $\tilde{g}(\alpha, \beta, \xi_1, \xi_2, \xi_3, \xi_4)$  and  $\tilde{f}(\alpha, \beta, \xi_1, \xi_2, \xi_3, \xi_4)$  as complex multivariable functions, the abstract form of the transducer tip velocity, total impedance, input power and input current can be expressed respectively as:

$$\tilde{v}_5 = \tilde{I}_{m5} = \tilde{g}(\alpha, \beta, \xi_1, \xi_2, \xi_3, \xi_4) \omega n_{0\text{Pi}} \tilde{V}_{\text{in}} \quad (6.1)$$

$$\tilde{Z}_{\text{tot}} = \tilde{f}(\alpha, \beta, \xi_1, \xi_2, \xi_3, \xi_4) \frac{1}{\omega^2 n_{0\text{Pi}}^2} \frac{1}{S_{\text{tr}}} \quad (6.2)$$

$$\tilde{P}_{\text{in}} = \frac{\tilde{V}_{\text{in}}^2}{\tilde{Z}_{\text{tot}}} = \frac{1}{\tilde{f}(\alpha, \beta, \xi_1, \xi_2, \xi_3, \xi_4)} \omega^2 n_{0\text{Pi}}^2 S_{\text{tr}} \tilde{V}_{\text{in}}^2 \quad (6.3)$$

$$\tilde{I}_{\text{in}} = \frac{1}{\tilde{f}(\alpha, \beta, \xi_1, \xi_2, \xi_3, \xi_4)} \omega^2 n_{0\text{Pi}}^2 S_{\text{tr}} \tilde{V}_{\text{in}}. \quad (6.4)$$

Note that by factoring out the excitation frequency,  $\omega$ , in (6.1), the vibration amplitude at the tip of the transducer can be easily derived as:

$$\tilde{u}_5 = \frac{\tilde{v}_5}{\omega} = \tilde{g}(\alpha, \beta, \xi_1, \xi_2, \xi_3, \xi_4) n_{0\text{Pi}} \tilde{V}_{\text{in}}. \quad (6.5)$$

Hence, it can be understood from the above equation that the delivered vibration amplitude of the piezoelectric transducer,  $\tilde{u}_5$ , is independent of its total cross section,  $S_{tr}$ , and the excitation frequency,  $\omega$ .

### 6.3.1.2 Optimization of the Langevin Piezoelectric Transducer

The optimal design of a Langevin piezoelectric actuator is usually quite cumbersome, due to the large number of variables that affect several performance criteria of the transducer. Fu *et al.* [6, 7] proposed a multi-objective optimization approach using genetic algorithms to find a set of Pareto-optimal solutions. While the obtained results are quite promising, they do not fully express the interaction of the design variables. They are also case dependent, since most constraints placed on the design variables (such as working frequency, voltage, actuator cross section) make the design space quite limited.

**Problem statement:** The optimization of a piezoelectric transducer with a stepped horn is formulated as a constrained multivariable multi-objective problem as shown below:

**Objective functions:** A number of performance criteria can be defined for a piezoelectric transducer. Similar to [6, 7], the inverse of vibration amplitude at the tip of the transducer (6.5) and the required input power (6.3) to drive the system, are considered as objective functions to be minimized.

**Design variables:**  $\xi_1, \xi_2, \xi_3$  and  $\xi_4$  are the primary design variables that determine the geometrical features of the transducer, provided that the working frequency is pre-determined (4.6). The driving voltage,  $\tilde{V}_{in}$ , the number of piezoceramic rings,  $n_{0Pi}$ , total cross section of the transducer,  $S_{tr}$ , the driving frequency,  $\omega$ , and cross sectional ratios,  $\alpha$  and  $\beta$ , are the secondary set of variables that directly affect the objective functions. As will be discussed later, the secondary design variables are predetermined due to structural, geometrical or power source constraints. Therefore, only the primary design variables, i.e.,  $\{\xi_1, \xi_2, \xi_3, \xi_4\}$ , will be considered for the multi-objective optimization problem.

In contrast with [6], material choices for various sections, i.e., back mass, piezo-

electric rings and front mass, are not considered as the design parameters in this work. In fact, material choices are preselected for each section. Should any new material be utilized for a section, another set of Pareto-optimal solutions has to be sought. By comparing various Pareto-optimal curves, the designer would be able to distinguish which material to choose for a particular level of input power and/or vibration amplitude.

**Design constraints:** Considering the practical design requirements, such as total length, size, fatigue limit of the selected materials, input power source, etc., several constraints associated with the search region of the design variables are introduced as discussed below:

- As explained earlier, the vibration amplitude at the output is independent of the total cross section of the transducer. Hence, it may seem logical to make a small transducer that requires only a small amount of power. The resulting device will, however, be more suited for micro-surgery [15, 16] rather than macro-surgery, due to the low rigidity of the cutting blade. Thus, the required lateral stiffness of the front mass combined with its fatigue limit, in addition to the desired amplification ratio of the stepped horn will determine the smallest allowable diameter of the transducer.
- Once the transducer outer diameter is determined, cross sectional ratios  $\alpha$  and  $\beta$  will be chosen based on the available piezoceramic ring size and the standard thread size for the back mass and the front mass connection.
- Considering Section 4 of the front mass within the ultrasonic transducer as an impedance matching interface between the source of energy (high acoustic impedance piezoelectric elements) and the load (low acoustic impedance soft tissue), the maximum transmission of energy will be achieved with one-quarter wavelength for Section 4, i.e.,  $\xi_4 = \frac{\pi}{2}$  [17]. In the case of operating the ultrasonic transducer in air, i.e.,  $\tilde{Z}_f = 0$ , this leads to a node at the interface of Section 3 and Section 4, i.e.,  $\tilde{v}_4 = \tilde{I}_{m_4} = 0$  and maximum load transfer between the two sections.
- It is required for the transducer to have the smallest possible length. Therefore,

the actuator must resonate at its first longitudinal frequency and its total length must be a half wavelength of the driving frequency. Hence,

$$g_4(\xi_1, \xi_2, \xi_3) = \xi_1 + \xi_2 + \xi_3 - \frac{\pi}{2} \leq 0, \quad (6.6)$$

where a quarter wavelength is assumed for Section 4. Additionally, each section must have a minimum length to make the final solution realizable. Therefore,

$$\begin{aligned} g_1(\xi_1, \xi_2, \xi_3) &= \xi_{1_{\min}} - \xi_1 \leq 0 \\ g_2(\xi_1, \xi_2, \xi_3) &= \xi_{2_{\min}} - \xi_2 \leq 0 \\ g_3(\xi_1, \xi_2, \xi_3) &= \xi_{3_{\min}} - \xi_3 \leq 0. \end{aligned} \quad (6.7)$$

- Assuming small structural damping of the transducer components, the total impedance of the system,  $\tilde{Z}_{\text{tot}}$ , becomes minimum (maximum) at resonance (anti-resonance), and therefore  $\text{Im}(\tilde{Z}_{\text{tot}}) = 0$ . This together with (6.2) leads to:

$$h_1(\xi_1, \xi_2, \xi_3) = \text{Im} \left( \tilde{f}(\alpha^*, \beta^*, \xi_1, \xi_2, \xi_3, \frac{\pi}{2}) \right) = 0, \quad (6.8)$$

where  $\alpha^*$ ,  $\beta^*$  and  $\frac{\pi}{2}$  are the previously described values selected for  $\alpha$ ,  $\beta$  and  $\xi_4$ .

**Optimization problem formulation:** The two-objective optimization problem can therefore be expressed as:

$$\begin{aligned} &\underset{\Xi}{\text{minimize}} && \mathbf{F}(\Xi) \\ &\text{subject to} && g_i(\Xi) \leq 0, \quad i = 1, \dots, 4 \\ &&& h_1(\Xi) = 0 \end{aligned} \quad (6.9)$$

where  $\Xi = [\xi_1, \xi_2, \xi_3]$  is the design variable vector,  $\mathbf{F}(\Xi) = [\frac{1}{|\tilde{u}_5|}, |\tilde{P}_{\text{in}}|]$  is the objective functions vector, and  $h_1(\Xi)$  and  $g_i(\Xi)$  are the constraint functions defined in (6.6)–(6.8).

**Optimization implementation:** Solving the optimization problem can be performed through two scenarios. In the first scenario, Pareto-based multi-objective

evolutionary algorithms are employed to find multiple Pareto-optimal solutions in a single run, thanks to their population-based approach. In the second scenario, either the available power source, or the required vibration amplitude at the tip of the transducer is given. Therefore, the optimization problem will be simplified into a single objective minimization problem

In this work, the optimization problem is solved through the first scenario to demonstrate the Pareto front curve. Assuming 40  $\mu\text{m}$  of vibration amplitude, the problem is then solved through the second scenario to find a miniaturized ultrasonic transducer design with the lowest input power.

### 6.3.1.3 Finite Element Analysis

While the equivalent circuit network modeling simplifies the electro-mechanical structure of an ultrasonic transducer in the form of lumped-mass parameters, there are several fundamental assumptions that make the obtained results slightly different from reality. First and foremost, the assumption of plane acoustic wave propagation that is a key condition in 1-D wave equation is no longer valid at an abrupt cross-sectional change and its vicinity such as a stepped horn. Secondly, the effect of pre-compression applied on piezoelectric rings and nonlinear mechanical losses due to the contact effect between various segments of a piezoelectric transducer cannot be correctly modeled using the equivalent circuit analogy.

In this work, ABAQUS FE software package (SIMULIA, Dassault Systemes, RI) is used to assess the performance of the designed transducer. The actual transducer design is, however, slightly modified from a pure step horn, to accommodate the supporting O-rings shown in Fig. 6.4. In order to extract all vibration modes and evaluate mode separation, a 3-D model of the piezoelectric transducer is created using 20-node quadratic brick, reduced integration elements. For the piezoelectric section, similar elements with additional charge DOF are utilized to correctly simulate its electro-mechanical effect. The Rayleigh damping model is assumed for the internal structural losses of the transducer.

Considering a general contact problem and 30 MPa pre-compression on the piezoelectric transducers [18], the *frequency analysis* followed by the *steady-state dy-*

*namic analysis* of the transducer is performed. The response of the actuator is then extracted in the form of mode shapes, the frequency response function, consumed current, and impedance curve.

## 6.3.2 Articulating Robotics-Assisted Surgical Tool

### 6.3.2.1 Articulating Wrist

Fig. 6.3 shows the CAD model of the proposed 1-DOF articulating wrist. In this design, two pulleys that are offset laterally and axially, are connected by two straight rods. Supported by two single-shear pins at their bases, the proposed design is a variant of a double-parallelogram mechanism. By actuating either of the pulleys through pulling cables, the top portion of the mechanism, which is supported by the two links, will be oriented around the remote axis of motion of the mechanism. By passing the electrical wires and/or pulling cables of the next joint through this axis, there will be no tensioning along the cables/wires, and therefore, no coupling will be observed among the DOFs.

Giving  $\pm 60^\circ$  pitch motion, the parallelogram structure of the proposed mechanism is particularly useful for enhanced stiffness of the wrist against large out-of-plane torque loads due to elongated tool lengths, i.e., a 5–10 cm long surgical tool that will be attached to the articulating portion of the wrist. In order to make the design compatible with the current standard practice, the outer diameter of the wrist was kept at 12 mm. In addition, the designed surgical wrist is compatible with da Vinci<sup>®</sup> tools at the proximal end and similar pulling cables can be employed to actuate all DOFs.

### 6.3.2.2 Gripping Jaw

The CAD model of the ultrasonic scalpel, its protective sheath and the 1-DOF gripping jaw ( $0\text{--}45^\circ$  grip) is shown in Fig. 6.4. The sheath cover was designed to accommodate various lengths of ultrasonic scalpels. A pair of pulling cables enters through the proximal end of the sheath and then exits from its distal end to actuate the gripping jaw. The electrical wires, connected to the copper electrodes of the ultra-



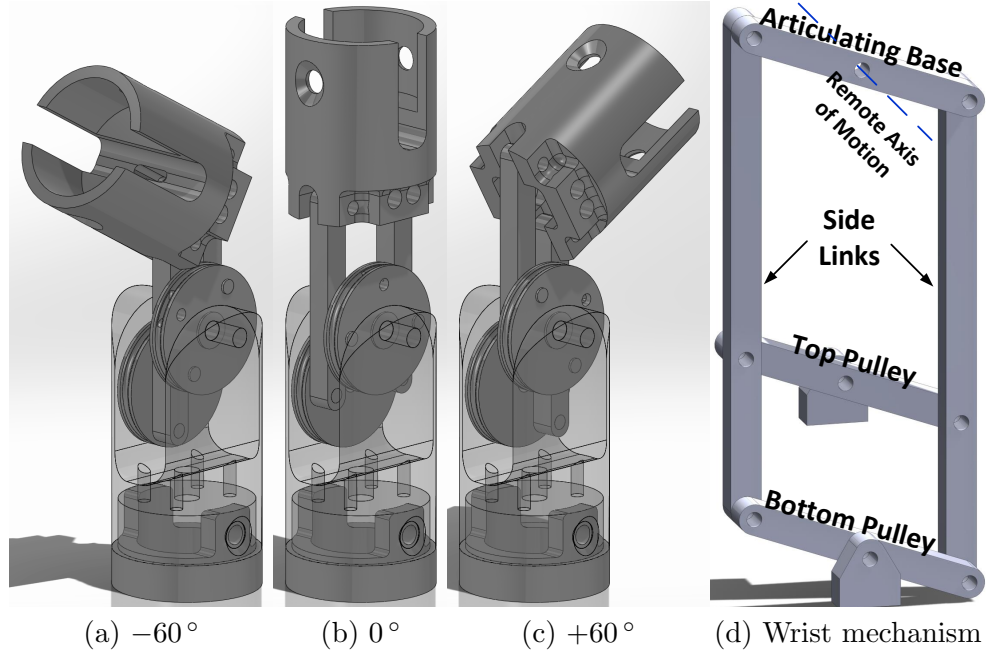


Figure 6.3: CAD model of the 1-DOF articulating wrist.

sonic scalpel, also pass through the proximal end of the sheath cover. As explained earlier, both pairs of cables and wires first run through the remote axis of rotation of the articulating wrist and then inside the surgical tool shaft to reach the base of the RAMIS tool. Although the outer diameter of the sheath cover was originally designed to be 12 mm to fit an ultrasonic scalpel of 8 mm diameter (Chapter 4), a long waiting period for ordering and receiving the proper piezoceramic rings, as well as much easier access to 10 mm piezoelectric sizes forced the design to be slightly altered. Hence, the outer diameter size of the sheath cover was increased to 14 mm.

## 6.4 Results and Discussion

### 6.4.1 Ultrasonic Scalpel

#### 6.4.1.1 Pareto Front

Due to changes in the size of the piezoelectric rings, and hence new  $\alpha$  and  $\beta$  values, the results obtained in Chapter 4 could not be used here. Therefore, the optimization

problem is solved again in this section considering the new piezoelectric ring size and material properties, that were obtained through tensile tests. Using the material properties in Table 6.1, as well as the constraints imposed on the primary and the secondary design variables in Table 6.2, the optimization problem (6.9) is formulated. Note that while satisfying (6.6) in order to keep the piezoelectric resonator at half-wavelength is a necessary condition, it is not sufficient. In fact, as will be discussed later, the necessary and sufficient condition for a resonator to be half-wavelength is a complex nonlinear function of the design parameters, contrary to the linear inequality expressed in (6.6). Therefore, in solving the optimization problem, the inequality constraint (6.6) is relaxed, i.e.,  $\xi_3 \leq 3\pi$ , to have not only half-wavelength resonators, but also a few other resonators with lengths longer than a half-wavelength in the design space.

The optimization problem is then solved through a controlled elitist genetic algorithm (a variant of NSGA-II\*). Starting from a population size of 300, an evenly distributed set of points on the Pareto front is obtained after about 150 generations. Fig. 6.5 shows the obtained Pareto front in the objective space overlayed on approximately 700,000 data points generated by an exhaustive search. As can be observed, the genetic algorithm has successfully captured the Pareto front associated with the design space for most part of the figure. For small power values, however, the algorithm is trapped into a local minimum and could not converge to the Pareto front correctly. The problem could have been fixed, if new starting points had been used throughout the run.

Although the obtained Pareto front is obtained for specific secondary design parameters, i.e.,  $V_{in}$ ,  $n_{0Pi}$ ,  $S_{tr}$  and  $\omega$ , it can be adjusted according to (6.3) and (6.5), should new values be used for the parameters. On the other hand, if any new set of materials,  $\alpha$ ,  $\beta$ ,  $\xi_{1min}$ ,  $\xi_{2min}$  or  $\xi_{3min}$  is intended to be used, the optimization problem has to be solved again using the genetic algorithm to obtain a new Pareto front curve.

---

\* Non-dominated sorting genetic algorithm [19]

Table 6.1: Material properties of the various sections of the piezoelectric actuator.

Property	Units	Symbol	APC 841	Titanium Ti-6Al-4V*	Steel Alloy*	Copper Alloy
Relative dielectric constant	1	$K^T$	1375	—	—	—
Dielectric loss	%	$\tan(\delta)$	0.40	—	—	—
Curie point	°C	$T_c$	320	—	—	—
Electromechanical coupling factor	%	$k_p$	0.6	—	—	—
		$k_{33}$	0.68	—	—	—
		$k_{31}$	0.33	—	—	—
		$k_{15}$	0.67	—	—	—
Piezoelectric charge constant	$10^{-12}$ m/V	$d_{33}$	300	—	—	—
		$-d_{31}$	109	—	—	—
		$d_{15}$	450	—	—	—
Piezoelectric voltage constant	$10^{-3}$ Vm/N	$g_{33}$	25.5	—	—	—
		$-g_{31}$	10.5	—	—	—
		$g_{15}$	35	—	—	—
		$Y_{11}^E$	7.6	10.403	17.824	11.50
Young's modulus	$10^{10}$ N/m <sup>2</sup>	$Y_{33}^E$	6.3	10.403	17.824	11.50
Density	$10^3$ Kg/m <sup>3</sup>	$\rho$	7.6	4.418	7.723	8.90
Poisson's ratio	1	$\nu$	0.34	0.342	0.3	0.31
Mechanical quality factor	1	$Q_m$	1400	877.2	2325.6	3030.3

\* Tensile tests are performed on three dog-bone samples of each Titanium and Steel materials using Instron 8804 machine (Instron®, Norwood, Massachusetts, USA). The average Young's moduli are reported herein.

#### 6.4.1.2 Case study

Using the obtained Pareto front, a piezoelectric actuator with tip vibration amplitude of  $40\ \mu\text{m}$  and resonance frequency of 50 kHz is designed. The required performance of such actuator is shown in Fig. 6.5 by the red dashed line. Fig. 6.6 shows the performance of the designed optimal actuator in terms of its tip vibration amplitude, total impedance, input power and input current. As can be observed, the actuator can deliver the required vibration amplitude at a 50 kHz resonance frequency. The required power source to drive this system is only 6.9 W, at a slightly high current value of 690.3 mA and input voltage of 5 V.

In order to assess the performance of the designed actuator, a finite element model of the system is developed using the ABAQUS FE software package. To make the 3-D model more realistic, 0.4 mm thick copper electrodes with the material properties listed in Table 6.2 are inserted between each piezoelectric ring. In Table 6.3, the first several mode shapes and their corresponding resonance frequencies obtained from the FE analysis, are compared with the results obtained from equivalent circuit theory. A slight difference can be observed between the first and the second longitudinal resonance frequencies obtained from the two methods. It is also clear that there is a reasonable mode separation among various frequencies, particularly between the first longitudinal mode, and the second and the third lateral modes.

In order to better investigate the neighboring mode interactions, the frequency range between the second and the third lateral mode shapes are considered for the steady-state dynamic analysis. An input voltage of 40 V is then swept within the chosen frequency range and the steady-state response of the system is acquired. Fig. 6.7 shows the obtained vibration amplitude, total impedance, input power and input current of the transducer within the specified frequency range. Although 5 V of voltage input is considered for the equivalent circuit model, it would be insufficient to generate  $40\ \mu\text{m}$  of tip vibration amplitude in FE model. This could be due to the fact that the FE model takes into account the non-linear contact problem, as well as 3-D wave propagation within the actuator. Therefore, 40 V of voltage input is utilized to excite the transducer model in FE and achieve  $40\ \mu\text{m}$  of vibration amplitude.

Table 6.2: Design parameter constraints.

Design Parameter	Units	Chosen Value	Lower Bound	Upper Bound
$\xi_1$	1	—	$3 \times 10^{-3} \times \omega / c_S$	$\pi/2$
$\xi_2$	1	—	$8 \times 10^{-4} \times \omega / c_{Pi}$	$\pi/2$
$\xi_3$	1	—	$3 \times 10^{-3} \times \omega / c_{Ti}$	$3\pi$
$\xi_4$	1	$\pi/2$	—	—
$V_{in}$	V	10	—	—
$n_{0Pi}$	1	4	—	—
$S_{tr}$	mm <sup>2</sup>	$\frac{10^2 \times \pi}{4}$	—	—
$\omega$	Hz	50,000	—	—
$\alpha$	1	$\frac{10^2 - 5^2}{10^2}$	—	—
$\beta$	1	$\frac{10^2 - 3.5^2}{10^2}$	—	—

Overall, the equivalent circuit model can be used to optimize the design of a piezoelectric actuator. Nevertheless, due to several assumptions that have been made in developing such model, the ultimate performance of the actuator has to be confirmed by means of finite element analysis. Moreover, the effect of adopting a certain horn profile (such as the stepped horn as analyzed in this work) on stress distribution within the transducer, can only be investigated through finite element analysis. Figure 6.8 shows results of extensive analysis conducted on the optimally designed actuator for both the *pre-stressing* step and *steady state dynamic analysis* step. As can be seen, while the modified stepped horn profile gives rise to the output vibration amplitude, high stress values are generated along the transducer due to the stress concentration effect of the stepped horn. Considering the fatigue strength of around 510 MPa for Ti-6Al-4V, the fatigue safety factor of the designed stepped horn is 1.44. Further study is required to investigate the use of other types of horn profiles in a piezoelectric actuator to achieve a higher fatigue safety factor.

Table 6.3: Mode shapes and their associated frequencies by finite element and equivalent circuit methods.

Mode Shape	Frequency (Hz)	Frequency (Hz)
	by Finite Element Method	by Equivalent Circuit Method
1 <sup>st</sup> lateral	13931	—
1 <sup>st</sup> torsional	30177	—
2 <sup>nd</sup> lateral	36278	—
1 <sup>st</sup> longitudinal	48610	50000
3 <sup>rd</sup> lateral	62867	—
4 <sup>th</sup> lateral	70795	—
2 <sup>nd</sup> torsional	79205	—
3 <sup>rd</sup> torsional	90649	—
2 <sup>nd</sup> longitudinal	96947	81915

#### 6.4.1.3 Prototyping

Using a combination of lathe, milling, wire EDM and high-speed EDM turning, the optimum ultrasonic scalpel was fabricated and assembled. Fig. 6.9 shows the impedance curve of the fabricated actuator obtained using a Solartron 1260 impedance analyzer (AMETEK Solartron Analytical, Inc., Farnborough, UK). As can be seen from the figure, the resonance frequency of the transducer is 49,132 Hz which varies slightly from the analytical results (50,000 Hz) and FE analysis (48,610 Hz).

#### 6.4.2 Articulating Ultrasonic Scalpel

All components of the designed articulating wrist were fabricated by lathe, milling, micro-milling and metal laser sintering and post-processed by wire EDM. Fig. 6.10 shows the tool components assembled together on a standard da Vinci<sup>®</sup> surgical instrument. The open-source da Vinci Research Kit [20] was used to tele-operatively drive the developed tool by a Classic da Vinci<sup>®</sup> surgical system. For this purpose, the kinematics of the PSM (Patient Side Manipulator) were updated by obtaining the DH parameters of the new tool (Fig. 6.11 and Table 6.4), and changing the

coupling matrix<sup>†</sup> through experiments. For this purpose, each joint was moved from one extreme to the other and the encoder counts on the pitch and yaw motors were recorded. MATLAB was then utilized to perform curve fitting on each set of encoder data to compute the appropriate expression for joint coupling. Based on the da Vinci<sup>®</sup> disk arrangement (Fig. 6.13), Table 6.5 shows the coupling matrix that was obtained through this procedure. Note that the developed tool has three active DOFs (compared to the 4-DOF da Vinci<sup>®</sup> standard tools), and therefore, has a slightly different coupling matrix.

Table 6.4: DH parameters of the new developed tool.

Frame	Joint name	$a_{i-1}$	$\alpha_{i-1}$	$d_i$	$\theta_i$
1	Outer yaw	0	$\frac{\pi}{2}$	0	$q_1 + \frac{\pi}{2}$
2	Outer pitch	0	$-\frac{\pi}{2}$	0	$q_2 - \frac{\pi}{2}$
3	Insertion	0	$\frac{\pi}{2}$	$q_3 - L_{RCM}$	0
4	Outer roll	0	0	$L_{Tool}$	$q_4$
5	Wrist pitch	0	$-\frac{\pi}{2}$	0	$q_5 - \frac{\pi}{2}$
6	Wrist yaw	$L_{Pitch2Yaw}$	$-\frac{\pi}{2}$	0	$q_6 - \frac{\pi}{2}$
7	End effector	0	$-\frac{\pi}{2}$	$L_{Yaw2Ctrlpnt}$	0

$L_{RCM} = 0.4318$  m,  $L_{Tool} = 0.4393$  m,  $L_{Pitch2Yaw} = 0.04435$  m,  
 $L_{Yaw2Ctrlpnt} = 0.01807$  m,  $q_1$  to  $q_6$  are the joint variables.

Table 6.5: Coupling matrix of the new developed tool.

	Disk 1	Disk 2	Disk 4
Roll	-1.56323325	0.0	0.0
Pitch	0.0	1.01857984	0.0
Yaw	0.0	0.0	1.21772597

<sup>†</sup> The mapping matrix between the actuator space and the joint space at PSM side.

## 6.5 Conclusions and Future Work

A robotics-assisted articulating ultrasonic surgical scalpel has been designed and constructed. First, the systematic optimal design of a miniaturized ultrasonic scalpel with stepped horn profile was described. For this purpose, an equivalent circuit model of a Langevin transducer was employed to establish a constrained multi-objective optimization problem. Using a genetic algorithm, Pareto optimal solutions of this optimization problem were sought and the optimal design of one case study was demonstrated. Finite element analysis was then utilized to evaluate the performance of the optimal design. Moreover, a novel surgical wrist compatible with the da Vinci<sup>®</sup> surgical system with decoupled two DOFs (pitch and grip) was developed. By integrating the fabricated ultrasonic scalpel with the articulating da Vinci<sup>®</sup> tool, a new robotics-assisted ultrasonic knife with higher maneuverability and flexibility was developed. The Classic da Vinci<sup>®</sup> surgical system controlled using dVRK (da Vinci<sup>®</sup> Research Kit) was then employed to drive the developed tool. Implementation of a phase-locked loop power control system to keep the ultrasonic scalpel at resonance, performance validation of the instrument in terms of vibration response and temperature rise during soft tissue cutting, as well as moving toward further miniaturization of the articulating wrist, are several aspects that will be addressed in the future.



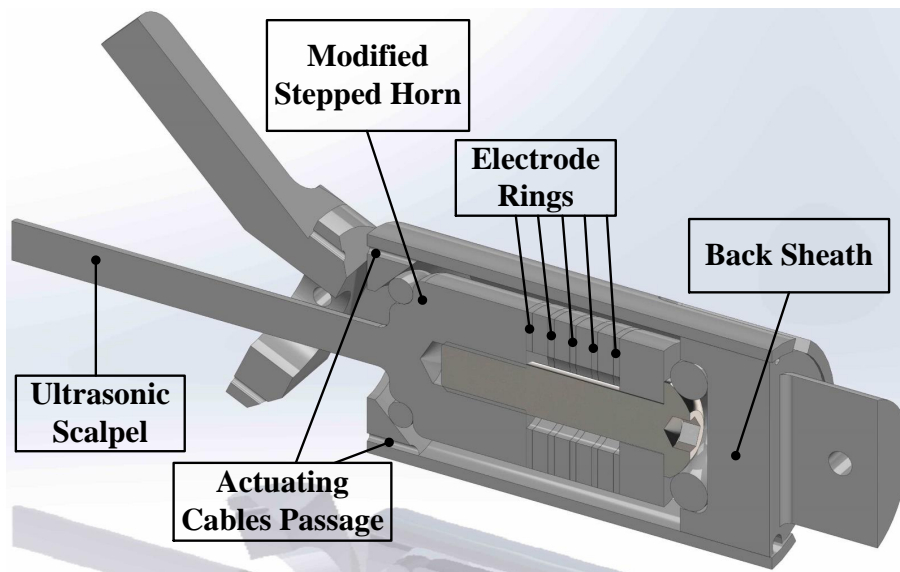
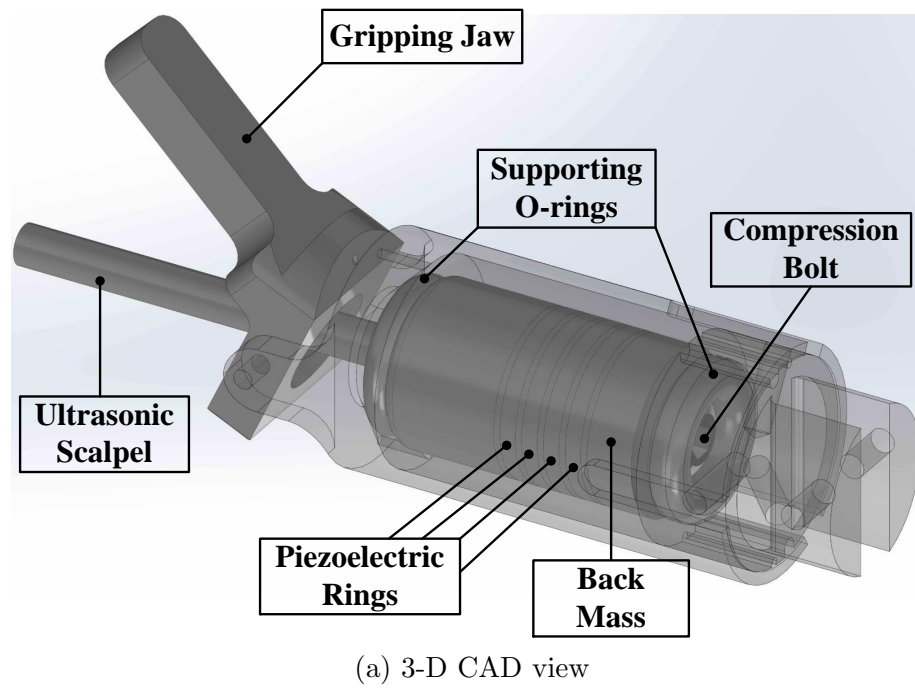


Figure 6.4: CAD model of the ultrasonic scalpel, its sheath cover and the gripping jaw.

### Pareto Optimal Solutions for a Uniformly Distributed $\{\xi_1, \xi_2\}$

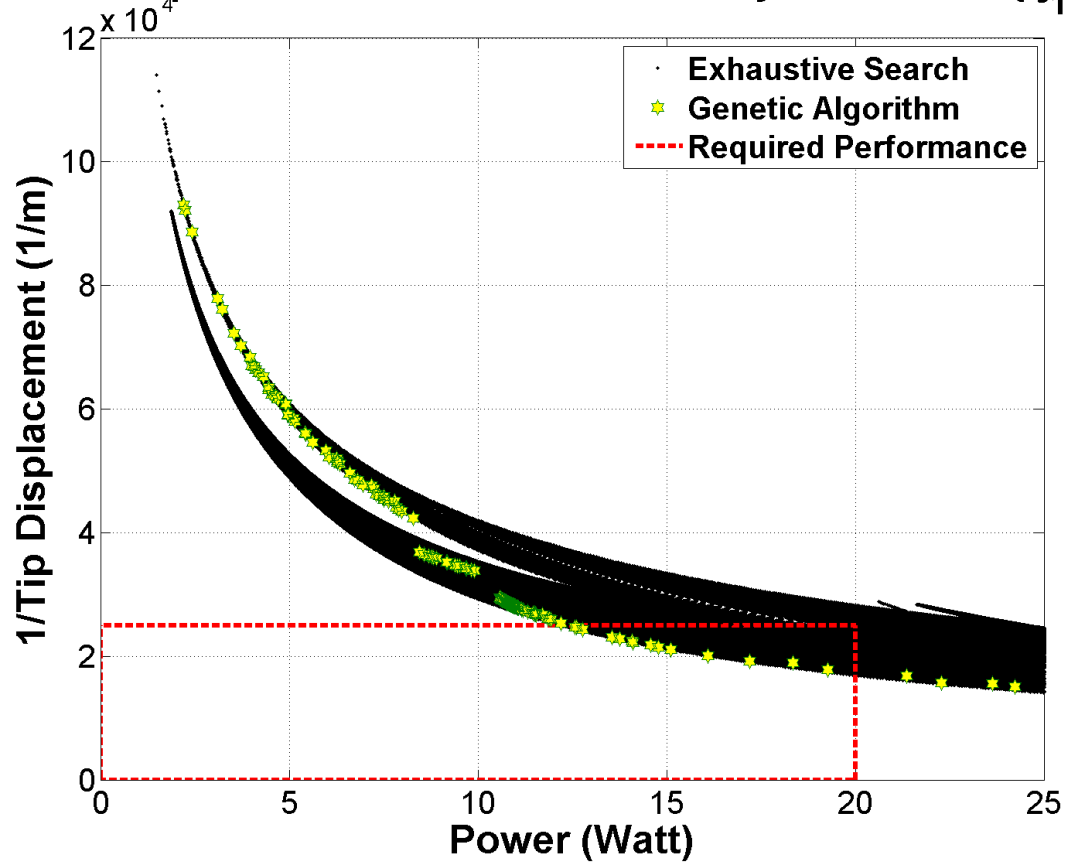


Figure 6.5: Pareto front curve obtained through Genetic algorithm, overlayed on around 300,000 solutions which are obtained by exhaustive search at the objective space.

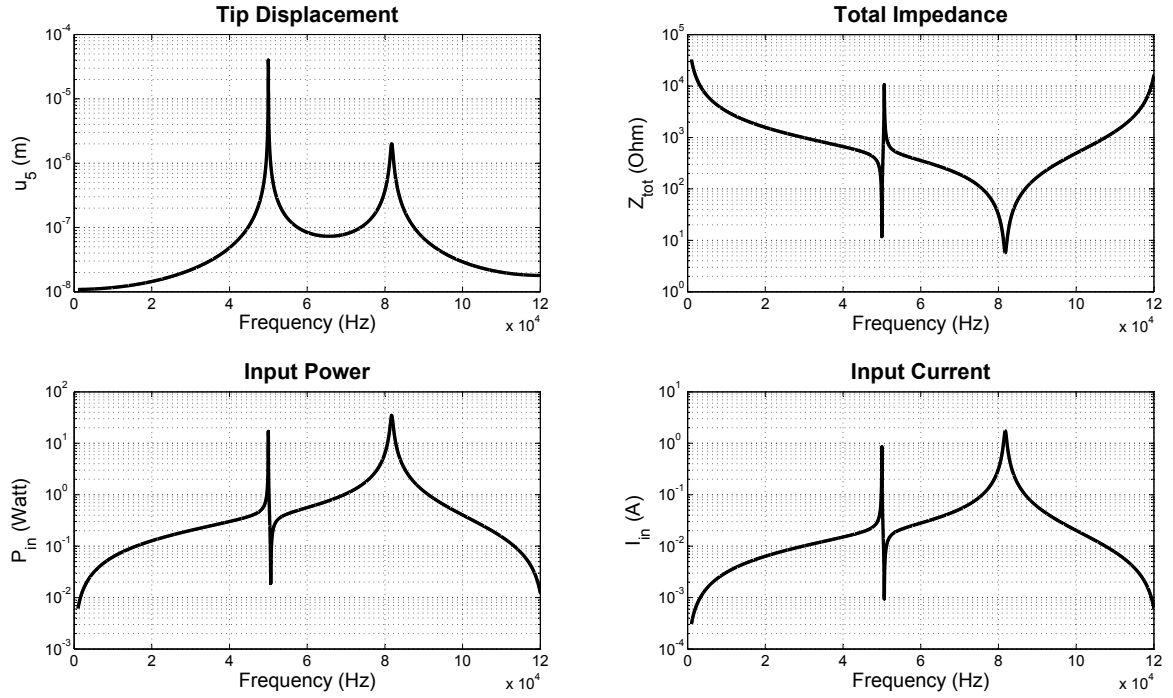


Figure 6.6: Performance measures of the designed optimal actuator obtained by equivalent circuit.

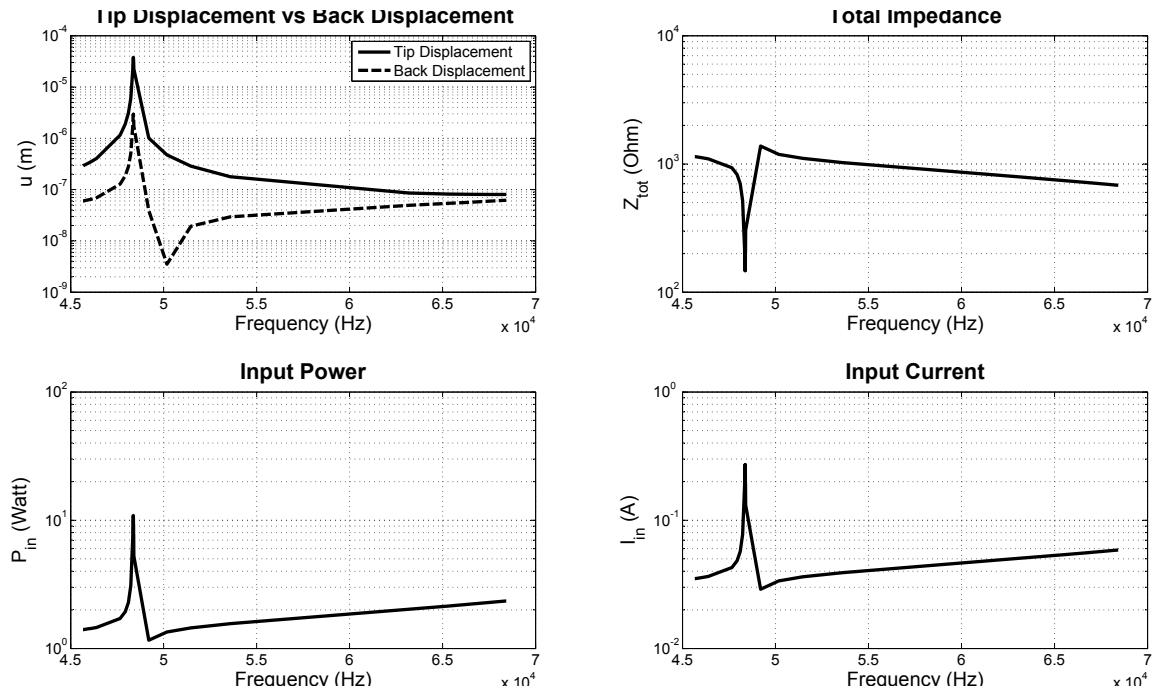


Figure 6.7: Performance criteria of the optimal designed actuator obtained by FEA.

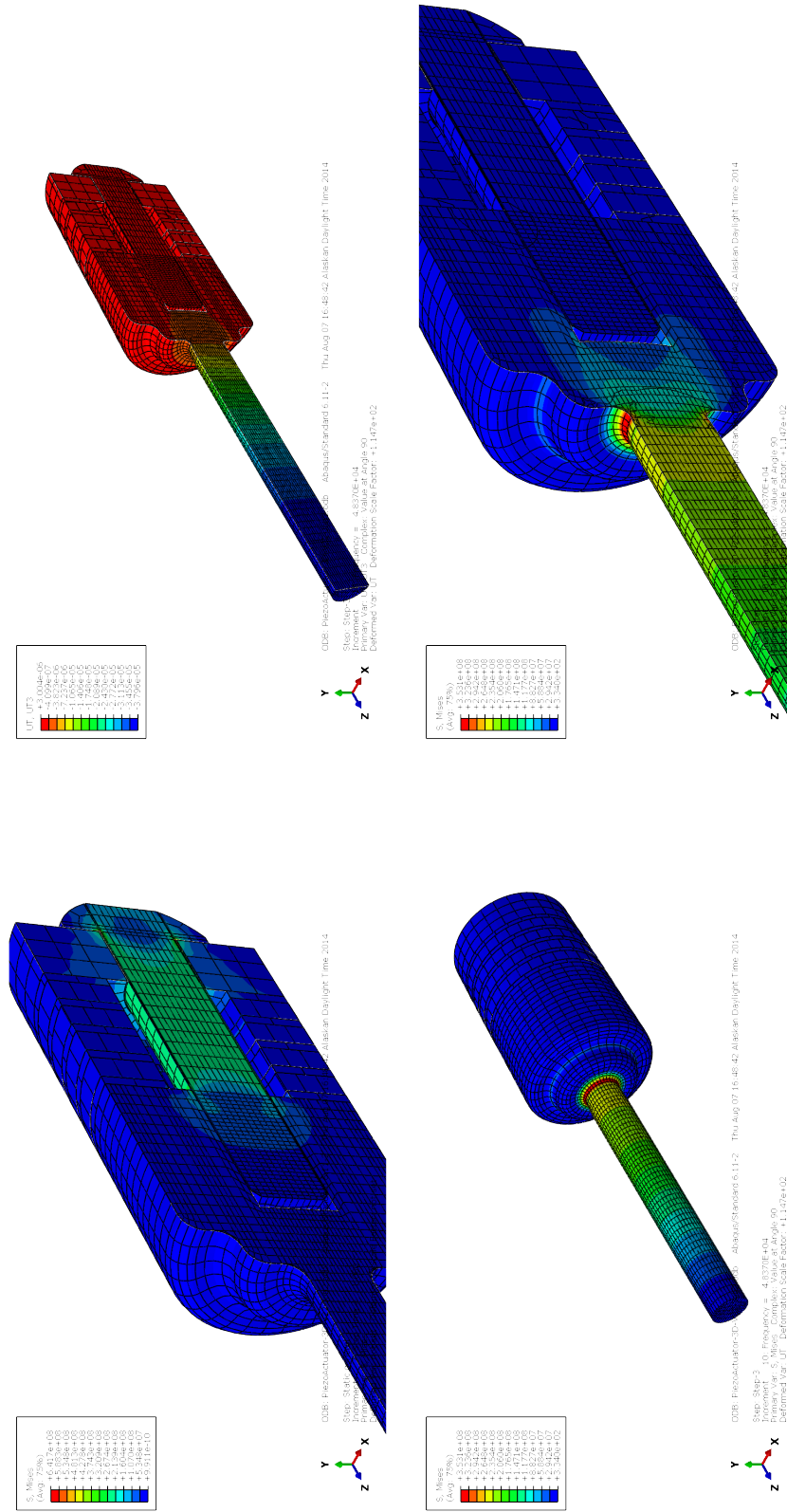


Figure 6.8: FE analysis of the optimally designed actuator: (top-left) pre-stressing step, (top-right) vibration amplitude along the transducer at resonance, (bottom-left) von Mises stress distribution within the transducer at resonance, (bottom-right) a closer view of the stress concentration effect at the step section.

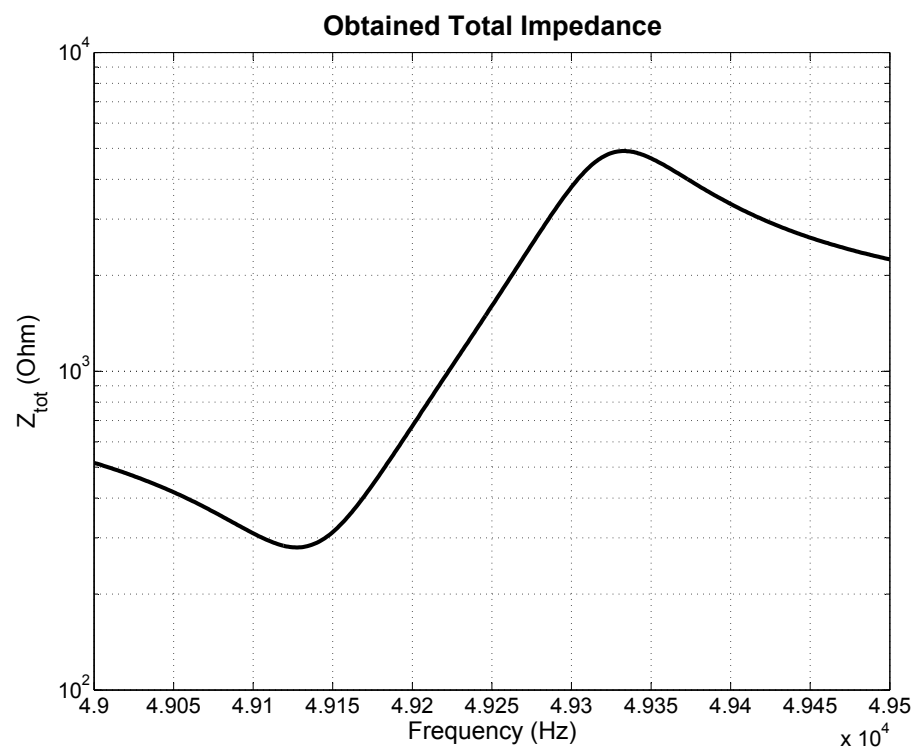


Figure 6.9: Measured impedance of the ultrasonic scalpel.

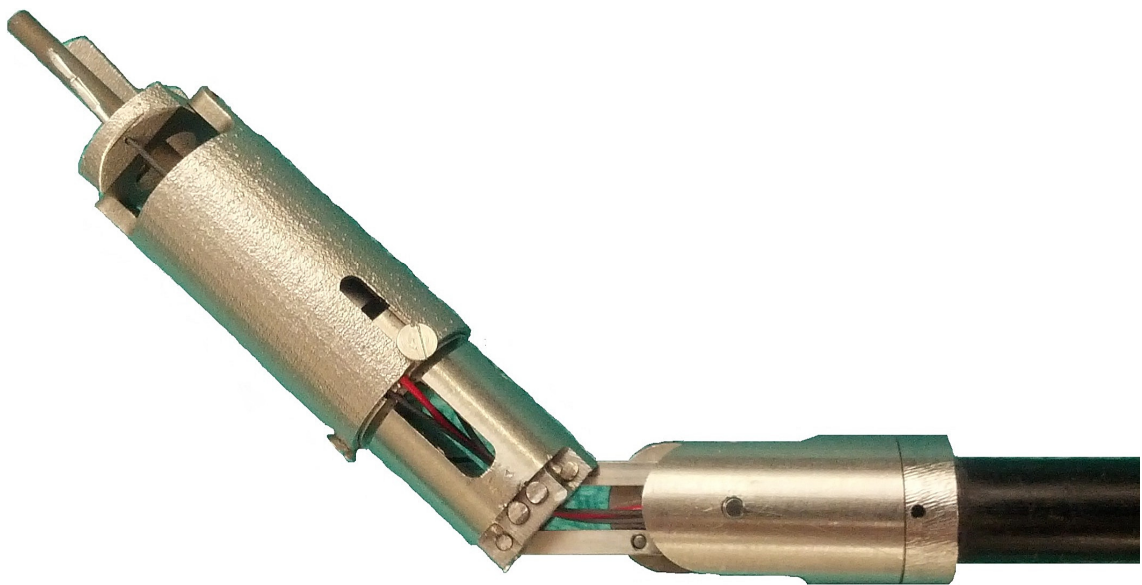
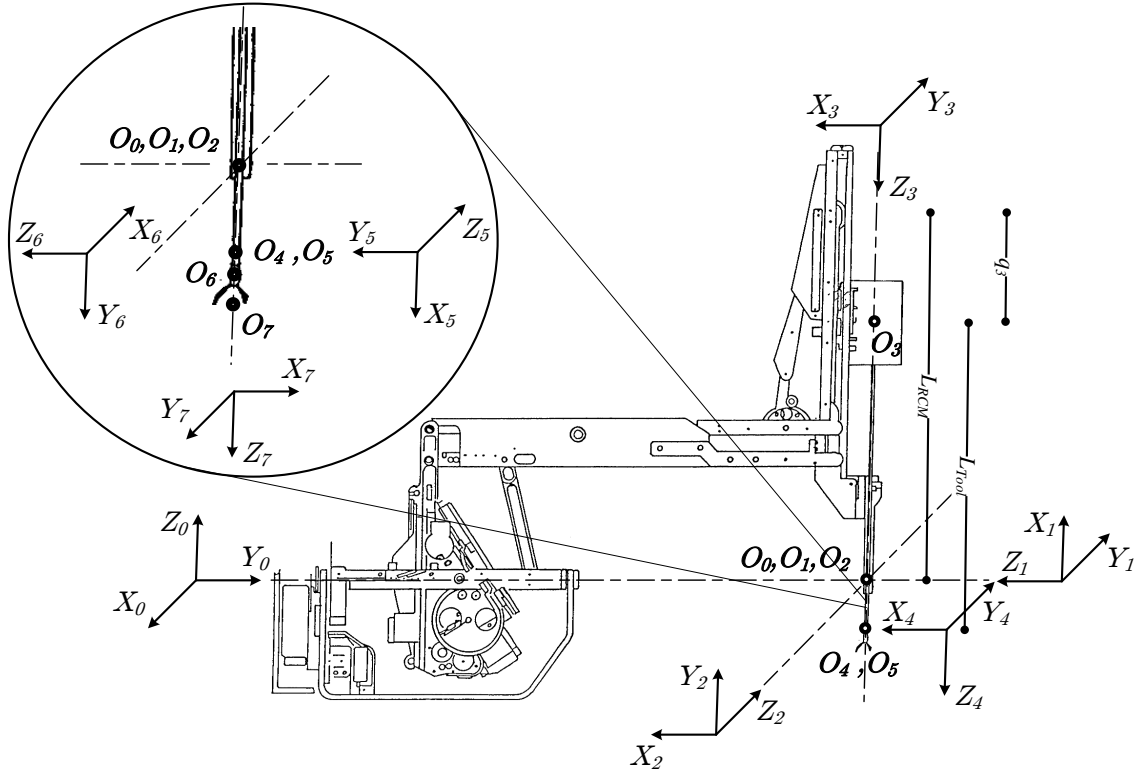
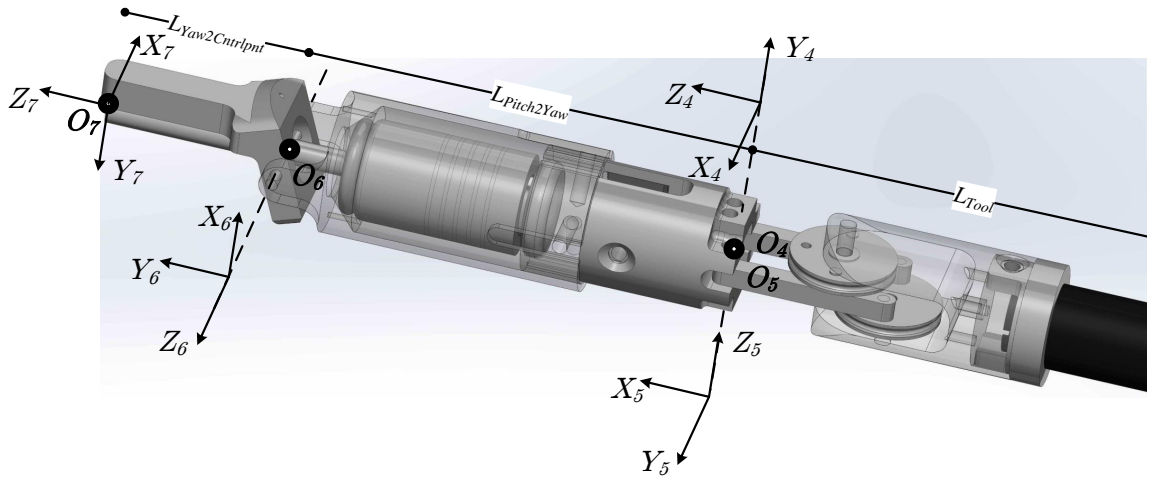


Figure 6.10: The developed articulating ultrasonic scalpel.



(a) Complete DH frame assignment on the PSM



(b) DH frame assignment on the instrument

Figure 6.11: Kinematics of the developed instrument.

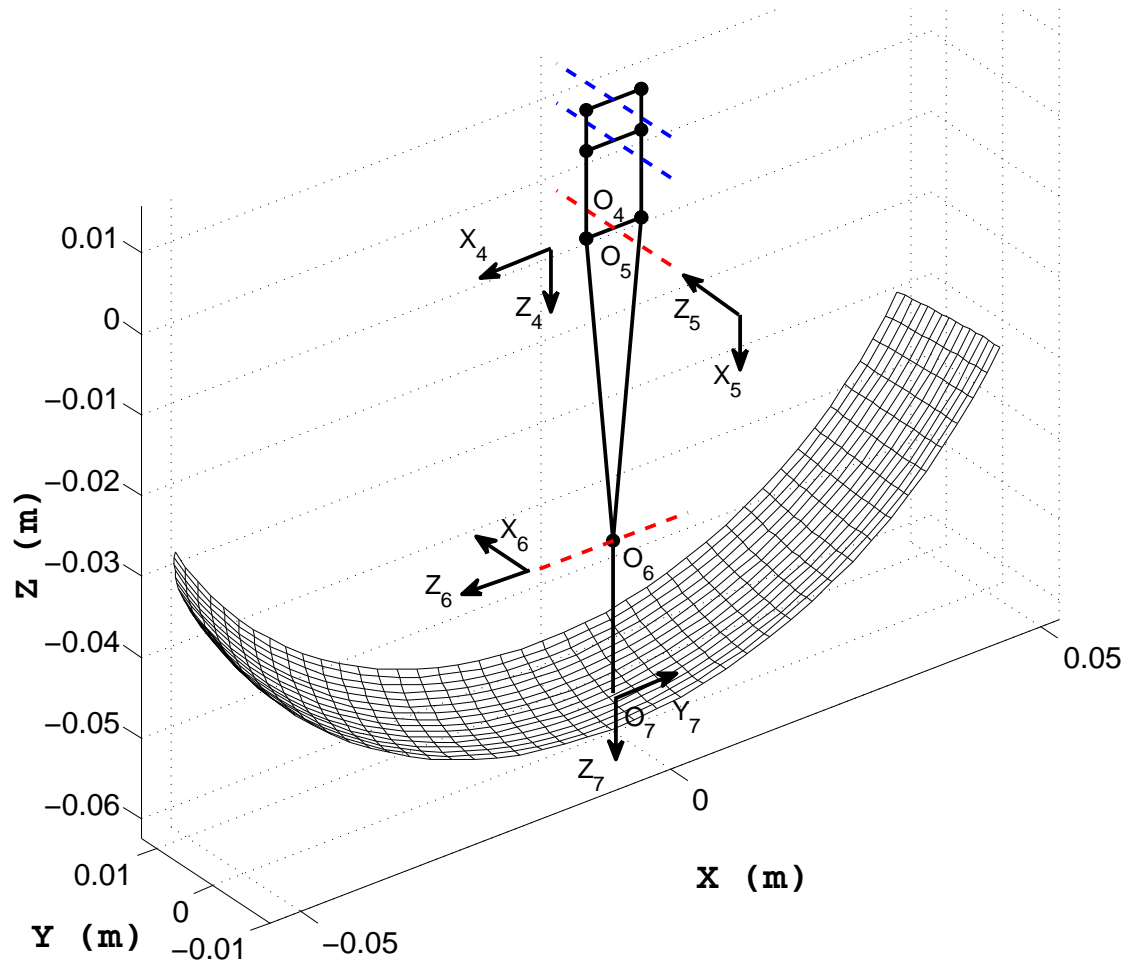


Figure 6.12: Workspace of the developed wrist.

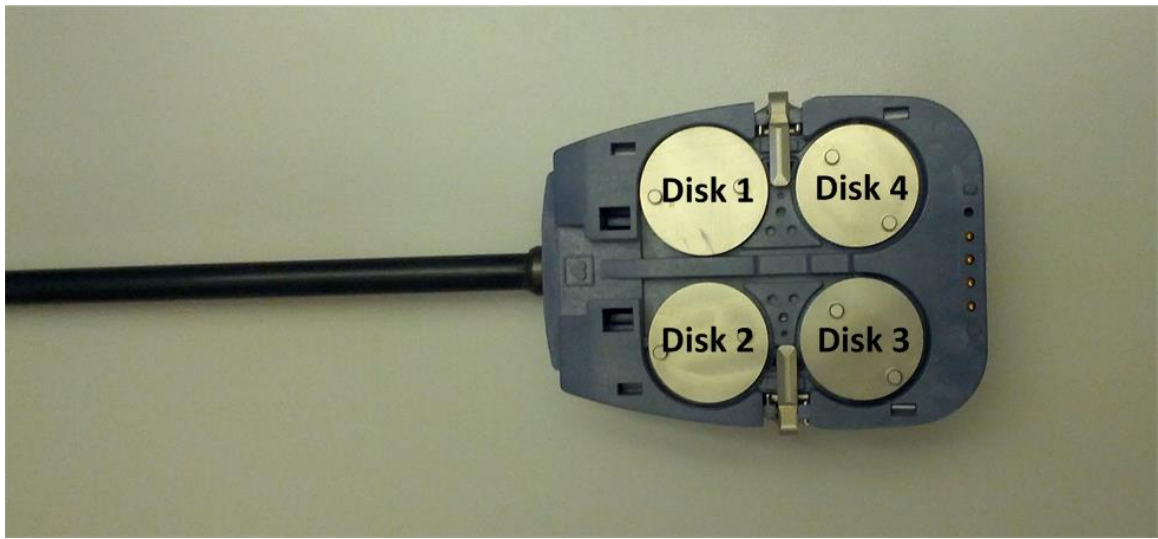


Figure 6.13: Disk numbering of a da Vinci<sup>®</sup> tool.



## References

- [1] R. Wakako and M. Hashimoto, “Development of ultrasonically activated bending scalpel for endoscopic surgery,” in *IEEE/RSJ International Conference on Intelligent Robots and Systems (IROS)*, vol. 2, 2002, pp. 1415–1420.
- [2] M. Hashimoto, K. Bandoh, and R. Wakako, “Development of ultrasonically activated bending scalpel using a link mechanism,” in *IEEE/RSJ International Conference on Intelligent Robots and Systems (IROS)*, 2005, pp. 1742–1747.
- [3] G. Ogura, R. Nakamura, Y. Muragaki, M. Hashizume, and H. Iseki, “Development of an articulating ultrasonically activated device for laparoscopic surgery,” *Surgical Endoscopy*, vol. 23, no. 9, pp. 2138–2142, 2009.
- [4] K. Isono and G. Ogura, “Ultrasonic surgical apparatus,” Dec. 9 2004, US Patent App. 11/008,773.
- [5] R. W. Timm, T. G. Dietz, and G. W. Knight, “Ultrasonic surgical instruments with distally positioned transducers,” Jun. 29 2012, US Patent App. 13/538,601.
- [6] B. Fu, T. Hemsell, and J. Wallaschek, “Piezoelectric transducer design via multiobjective optimization,” *Ultrasonics*, vol. 44, pp. e747–e752, 2006.
- [7] B. Fu, “Piezoelectric actuator design via multiobjective optimization methods,” Ph.D. dissertation, University of Paderborn, 2005.
- [8] W. P. Mason, *Electromechanical transducers and wave filters*. D. Van Nostrand Co., 1948.
- [9] A. J. Madhani and J. K. Salisbury, “Articulated surgical instrument for performing minimally invasive surgery with enhanced dexterity and sensitivity,” Aug. 11 1998, US Patent 5,792,135.

- [10] D. Wallace, D. Rosa, and F. Moll, “Surgical instrument with extended reach for use in minimally invasive surgery,” Nov. 6 2001, US Patent 6,312,435.
- [11] T. Cooper, D. Wallace, S. Chang, S. Anderson, D. Williams, and S. Manzo, “Surgical tool having positively positionable tendon-actuated multi-disk wrist joint,” Nov. 16 2004, US Patent 6,817,974.
- [12] M. R. Moreyra, “Wrist with decoupled motion transmission,” Nov. 29 2005, US Patent 6,969,385.
- [13] S. Sherrit, B. P. Dolgin, Y. Bar-Cohen, D. Pal, J. Kroh, and T. Peterson, “Modeling of horns for sonic/ultrasonic applications,” in *IEEE Ultrasonics Symposium*, vol. 1, 1999, pp. 647–651.
- [14] T. Li, Y. Chen, and J. Ma, “Development of a miniaturized piezoelectric ultrasonic transducer,” *IEEE Transactions on Ultrasonics, Ferroelectrics and Frequency Control*, vol. 56, no. 3, pp. 649–659, 2009.
- [15] Y. Shen, M. Nakajima, S. Kojima, M. Homma, Y. Ode, and T. Fukuda, “Characterization of oscillating nano knife for single cell cutting by nanorobotic manipulation system inside ESEM,” in *IEEE International Conference on Robotics and Automation (ICRA)*, 2011, pp. 4133–4138.
- [16] L. Chen, C. Ru, W. Rong, Y. Liu, and L. Sun, “Design, modeling and control of a piezoelectric ultrasonic microdissection technique for the molecular analysis of tissue,” *Smart Materials and Structures*, vol. 19, no. 2, p. 025003, 2010.
- [17] P. D. Edmonds and F. Dunn, “0. introduction: Physical description of ultrasonic fields,” in *Ultrasonics*, ser. Methods in Experimental Physics, P. D. Edmonds, Ed. Academic Press, 1981, vol. 19, pp. 1–28.
- [18] H. D. Al-Budairi, “Design and analysis of ultrasonic horns operating in longitudinal and torsional vibration,” Ph.D. dissertation, University of Glasgow, 2012.
- [19] K. Deb, *Multi-objective optimization using evolutionary algorithms*. John Wiley & Sons, 2001, vol. 16.

- [20] P. Kazanzides, Z. Chen, A. Deguet, G. S. Fischer, R. H. Taylor, and S. P. DiMaio, “An open-source research kit for the da vinci<sup>®</sup> surgical system,” in *IEEE International Conference on Robotics and Automation (ICRA)*, 2014, pp. 6434–6439.

## Chapter 7

# Concluding Remarks and Future Work

Concluding remarks have been made at the end of each chapter related to the contributions of this thesis. In this chapter, overall concluding remarks and suggestions for future work are given.

In this thesis, the application of mechanical vibration in robotics-assisted surgical intervention is explored for three different challenges associated with lung cancer diagnosis and treatment. In the first part of the thesis (Chapter 2), the problem of motion compensation during robotics-assisted needle insertion into the soft tissue was addressed using an oscillatory-based impedance controller. In the second part of the thesis (Chapter 3), a novel vibration-assisted technique for needle insertion into soft tissue was proposed to reduce the frictional force effects between the moving needle and the soft tissue. In the third part of the thesis (Chapters 4, 5 and 6), an ultrasonically activated scalpel was designed and developed to be used for internal body applications. A novel 2-DOF robotic wrist was then developed to maneuver the ultrasonic scalpel using the Classic da Vinci<sup>®</sup> surgical system and the da Vinci<sup>®</sup> Research Kit (dVRK).

## 7.1 Remarks

Concluding remarks for the research described in each of the three parts of the thesis are included here.

### 7.1.1 Motion Compensation

A mechatronic solution was proposed for undesirable modulated motion of soft tissue during needle insertion into the lung. The proposed platform, which consists of an

autonomous macro robot for motion compensation, and a tele-operated micro robot for needle insertion, gives the user (e.g., the surgeon) the possibility of delivering the therapy or taking biopsy samples from the moving soft tissue with minimum tissue deformation by tracking the soft tissue motion. An impedance-based control strategy based-on a multi-DOF vibratory system was implemented for the macro robot. The feasibility of the proposed approach was shown using an experimental setup consisting of two PA10-7C Mitsubishi manipulators that were used for 1) manipulating the macro part based on the output of the impedance control strategy; and 2) mimicking the 1-D tissue motion behavior while holding the tissue. The implemented tele-operated (master–slave) architecture, potentially addresses the problem of X-ray exposure for the clinician, i.e., the clinician can perform lung biopsy away from the immediate vicinity of the scanner. Although the results showed an experimental tracking error of about  $\pm 3.5$  mm, it was shown that this error was within the expected error range of the system due to the conservative design of the control parameters. It was concluded that by employing higher performance pressure sensors, more accurate soft tissue identification and fine-tuning of the control parameters, the system performance can be improved. Application to other organs where there is a respiratory motion effect such as the liver, could also be considered.

### 7.1.2 Vibration-Assisted Needle Insertion

Friction is a significant force component in needle–tissue interaction during percutaneous interventions. In order to reduce such frictional effects, a vibration-assisted needle insertion technique was proposed. To better understand the impact of amplitude and frequency variation of a vibratory insertion profile on translational friction, an analytical solution was presented. An experimental setup that consists of a pair of amplified piezoelectric actuators, attached to an 18 GA brachytherapy needle, was developed. The experimental results illustrate that within a certain range of amplitudes and frequencies, the theoretical model holds true. As observed, the total friction force drops as the frequency of the vibration increases relative to the insertion velocity. By minimizing frictional effects, soft tissue deformation is reduced.

Thus, vibration-assisted needle insertion is expected to improve targeting accuracy. However, in order to generalize the proposed technique, a wider range of vibration frequencies and amplitudes needs to be examined.

### 7.1.3 Ultrasonically Activated Scalpel for Internal Body Applications

When it comes to minimally invasive surgical dissection of soft tissue, there are a few modalities that enable hemostatic cutting and/or coagulation. MIS suturing and stapling, high frequency monopolar and bipolar electrocautery, high-power low-frequency mechanical vibration, and laser surgery are among the popular modes of energy-based methods for resection or transection of soft tissue. Among all of these modalities, ultrasonically activated scalpels have demonstrated superior characteristics. However, several drawbacks such as large size, long and rigid shape, high power consumption, and high transmission loss have rendered them unattractive for advanced internal body operations, particularly in Robotics-Assisted Minimally Invasive Surgery (RAMIS). Thus, the aim of the last part of this thesis was to address this issue by optimizing an ultrasonic scalpel for use within the body.

First, the systematic optimal design of a miniaturized ultrasonic scalpel with stepped horn profile was described. For this purpose, an equivalent circuit model of a Langevin transducer was employed to establish a constrained multi-objective optimization problem. Using a genetic algorithm, Pareto optimal solutions of this optimization problem were sought and the optimal design of one case study was demonstrated. Finite element analysis was then utilized to evaluate the performance of the optimal design. Good agreement was observed among the results obtained by the two methods. It was shown that using an equivalent circuit model, optimization of Langevin piezoelectric actuators can be performed in non-dimensional space, i.e., any length, any working frequency, any transducer cross section or any number of piezoelectric rings can be adopted within the obtained results. The performance of the optimal design, however, must be evaluated by means of finite element analysis, due to the inherent limitations of the equivalent circuit theory.

While a stepped horn profile exhibits the highest amplification ratio and shortest length among all other horn profiles, high stress concentrations limit their practical use. To address this problem, a new analytical-numerical method was proposed to systematically design a high amplification ultrasonic horn profile. Due to the generality of NURBS curves in defining complex geometries and their compact representation, an optimization problem was formulated and solved based on NURBS basis functions to explicitly define the horn profile. The obtained amplification factor and natural frequencies were verified via finite element analysis.

Lastly, a robotics-assisted articulating ultrasonic surgical scalpel was designed and constructed. Using the obtained material properties and new piezoelectric sizes, another set of optimal solutions were obtained for the optimization problem of a Langevin transducer. A novel surgical wrist compatible with the da Vinci<sup>®</sup> surgical system with decoupled two DOF (pitch and grip) was also developed. By integrating the fabricated ultrasonic scalpel with the articulating da Vinci<sup>®</sup> tool, a new robotics-assisted ultrasonic knife with higher maneuverability and flexibility was developed. The Classic da Vinci<sup>®</sup> surgical system controlled using dVRK (da Vinci<sup>®</sup> research kit) was then employed to drive the developed tool.

## 7.2 Future Research

While the application of mechanical vibration in surgery is not limited to the scope of this thesis, there are several possible directions associated with each topic of this work that can be explored by other researchers in future.

### 7.2.1 Motion Compensation

- One possible area of future research is extending the proposed approach to compensate for the 3-D motion of soft tissue considering the remote-center-of-motion (RCM) constraint of the surgical robot. For this purpose, all three dimensions of the force components need to be measured at the tip of the macro robot. Initial efforts have already been made to build and incorporate

multiple TakkTile pressure sensors [1] to measure both normal and shear force components, as well as the yaw and pitch moments (Fig. 7.1). Employing such high-performance pressure sensors with moderate spatial resolution (3–5 mm), and excellent sensitivity ( $< 0.01$  N), linearity ( $< 1\%$ ), and bandwidth ( $> 100$  Hz), will most likely eliminate the problem of tracking inaccuracy observed using FSR pressure sensors.

- Designing the impedance controller based on the mechanical properties of the soft tissue under exploration can be extended to other robotics-assisted surgical interventions where motion compensation is a must. Cardiovascular surgery (such as valvular heart disease repair, coronary artery bypass grafting, and congenital heart defect surgery), as well as lung or liver surgeries (such as tumor biopsy and thermal ablation therapy) are several examples where robotics-assisted cardiac and respiratory motion compensation makes the procedure less challenging.
- Employing more miniaturized pressure sensors and designing a whole new surgical instrument to be incorporated with the da Vinci<sup>®</sup> surgical system will pave the way for the introduction of new instruments into the operating rooms and hence, the market.

### 7.2.2 Vibration-Assisted Needle Insertion

- One possible future extension includes investigating other types of *ex-vivo* soft tissue samples, e.g., liver, lung and bone. It is anticipated that the proposed vibration-assisted needle insertion technique will be particularly useful in bone biopsy where the dominant resistive force factor is Coulomb friction.
- It is expected that by measuring the vibration amplitude and frequency during needle insertion into the soft tissue, better accuracy and consistency will be achieved. For this purpose, a micron-sensitive capacitive vibration sensor [2] has been fabricated (Fig. 7.2) to better control the frequency and vibration amplitude of the vibrating needle in a closed-loop control architecture.
- The effect of the vibrating needle on the pre-puncture force and the cutting force



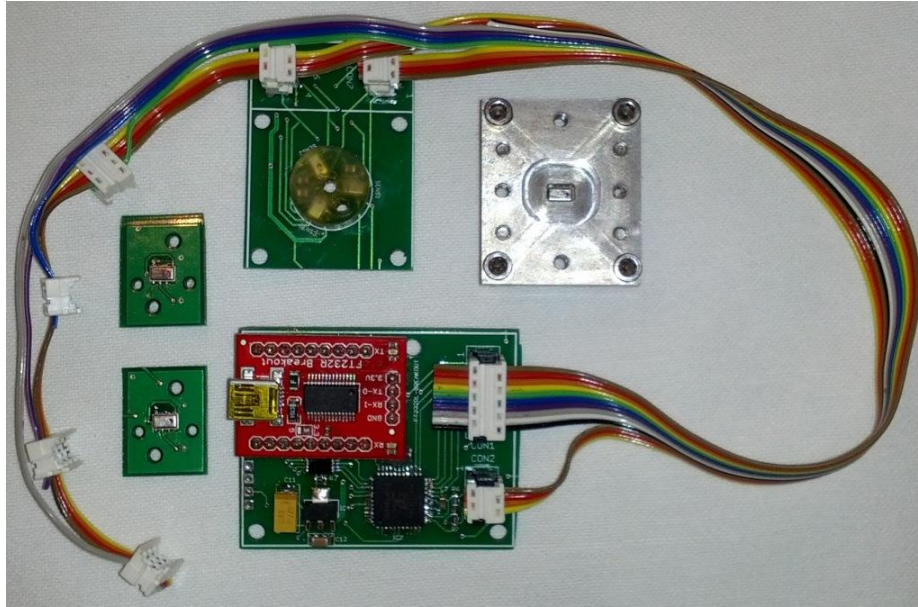


Figure 7.1: Prototypes of TakkTile sensors made as single units (bare sensors), or in an array unit (filled with rubber).

can also be investigated extensively. The possible outcomes, together with the obtained results of this thesis will be a solid starting point for investigating the effect of this novel technique for enhancing the tumor targeting and needle steering.

- Color Doppler detection of the needle tip is one of the recommended approaches to visualize the needle tip under ultrasound guidance [3]. For this purpose, various researchers have tried different techniques, such as inducing minute vibrations on the needle shaft by attaching an external device (The ColorMark device, EchoCath Inc, Princeton, NJ), oscillating an air column, manual motion of the needle, or vibration induced by rotation of a bent stylet within the needle [4, 5]. The needle vibration setup developed as part of this thesis offers an attractive alternative for color Doppler based needle tip tracking under ultrasound guidance.
- Due to the compact design of the current vibrating needle setup, another future direction could be incorporating a vibration-assisted needle into the surgical needle insertion robots that have been developed in CSTAR, such as Hadavand's

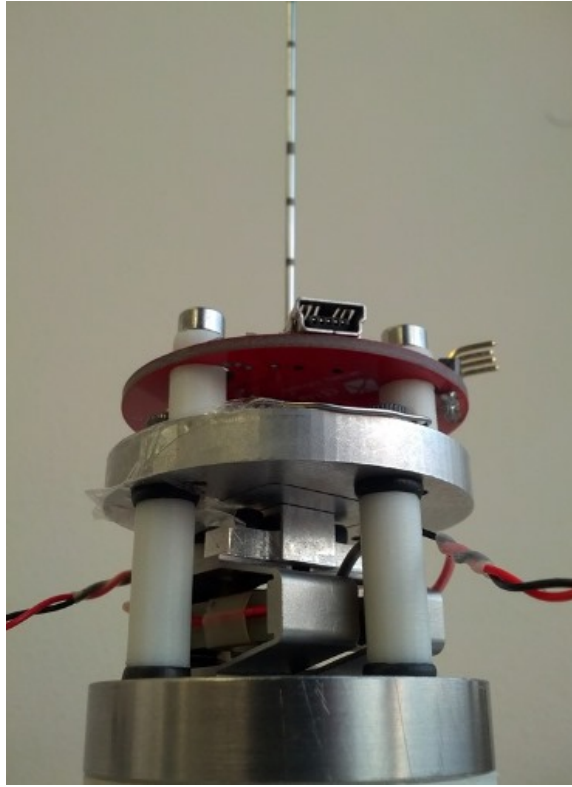


Figure 7.2: Piezoelectric actuator unit with micron-sensitive vibration sensor.

patient-mounted robot for thoracic and abdominal interventions [6], as well as Bassan's needle insertion robot for interventions targeting the prostate [7].

### 7.2.3 Ultrasonically Activated Scalpel for Internal Body Applications

- The performance of the ultrasonic scalpel can be improved by implementing a phase-locked loop power control system to keep the ultrasonic scalpel at resonance. Note that the developed ultrasonic scalpel in its current form works in an open-loop manner, and as soon as it makes contact with the environment, the impedance of the whole system changes, which in turn causes the resonance frequency to shift. Therefore, a proper closed-loop control architecture (in terms of a phase-locked loop control strategy between the voltage and the current, or a feedback signal from a vibration amplitude sensor) is required to maintain the

scalpel in resonance. Lack of such feedback loop makes the scalpel to go out of resonance, as soon as it makes contact with a high impedance environment.

- Performance validation of the instrument in terms of the vibration response and temperature rise could be another future direction for this project. In addition, it is necessary to perform a thorough experimental modal analysis of the device using a 3-D laser Doppler vibrometer.
- Further miniaturization of the articulating wrist, as well as employing other horn profiles (e.g., NURBS-based profile in Chapter 5) are what expected to improve the fatigue life of the ultrasonic scalpel and make it more acceptable within the medical community.

## References

- [1] Y. Tenzer, L. P. Jentoft, and R. D. Howe, “Inexpensive and easily customized tactile array sensors using MEMS barometers chips,” *Under Review, Accessed Oct. 2012*.
- [2] L. K. Baxter, *Capacitive Sensors: Design and Applications*. IEEE Press, 1997.
- [3] K. J. Chin, A. Perlas, V. W. Chan, and R. Brull, “Needle visualization in ultrasound-guided regional anesthesia: challenges and solutions,” *Regional Anesthesia and Pain Medicine*, vol. 33, no. 6, pp. 532–544, 2008.
- [4] A. Harmat, R. N. Rohling, and S. E. Salcudean, “Needle tip localization using stylet vibration,” *Ultrasound in Medicine & Biology*, vol. 32, no. 9, pp. 1339–1348, 2006.
- [5] D. Souzdalnitski, I. Lerman, and T. M. Halaszynski, “How to improve needle visibility,” in *Atlas of Ultrasound-Guided Procedures in Interventional Pain Management*. Springer, 2011, pp. 35–75.
- [6] M. Hadavand, M. D. Naish, and R. V. Patel, “A parallel remote center of motion mechanism for needle-based medical interventions,” in *IEEE RAS & EMBS International Conference on Biomedical Robotics and Biomechatronics*, 2014, pp. 1–6.
- [7] H. S. Bassan, R. V. Patel, and M. Moallem, “A novel manipulator for percutaneous needle insertion: Design and experimentation,” *IEEE/ASME Transactions on Mechatronics*, vol. 14, no. 6, pp. 746–761, 2009.

## Appendices

## Appendix A

Using the Kirchhoff's voltage law (KVL), the current values passing through each branch in Fig. 4.2 can be obtained by solving the following set of linear equations:

$$\begin{bmatrix} a & -C_1 & 0 & 0 & 0 \\ -C_1 & b & -C_2 & 0 & 0 \\ 0 & -C_2 & c & -C_3 & 0 \\ 0 & 0 & -C_3 & d & -C_4 \\ 0 & 0 & 0 & -C_4 & e \end{bmatrix} \begin{Bmatrix} \tilde{I}_{m_1} \\ \tilde{I}_{m_2} \\ \tilde{I}_{m_3} \\ \tilde{I}_{m_4} \\ \tilde{I}_{m_5} \end{Bmatrix} = \begin{Bmatrix} 0 \\ \tilde{V}_m \\ -\tilde{V}_m \\ 0 \\ 0 \end{Bmatrix}, \quad (\text{A.1})$$

where

$$\begin{aligned} a &= \tilde{Z}_b + \tilde{Z}_{L_1} + \tilde{Z}_{C_1} \\ b &= \tilde{Z}_{C_1} + \tilde{Z}_{L_1} + \tilde{Z}_{L_2} + \tilde{Z}_{C_2} \\ c &= \tilde{Z}_{C_2} + \tilde{Z}_{L_2} + \tilde{Z}_{L_3} + \tilde{Z}_{C_3} \\ d &= \tilde{Z}_{C_3} + \tilde{Z}_{L_3} + \tilde{Z}_{L_4} + \tilde{Z}_{C_4} \\ e &= \tilde{Z}_{C_4} + \tilde{Z}_{L_4} + \tilde{Z}_f \\ C_1 &= \tilde{Z}_{C_1} \\ C_2 &= \tilde{Z}_{C_2} \\ C_3 &= \tilde{Z}_{C_3} \\ C_4 &= \tilde{Z}_{C_4} \\ \tilde{V}_m &= \tilde{N} \frac{\tilde{Z}_{C_0}}{\tilde{Z}_{tot}} \tilde{V}_{in}. \end{aligned}$$

Solving for unknown values of  $\tilde{I}_{m_1}$  to  $\tilde{I}_{m_5}$ , they can be calculated as:

$$\begin{aligned} \tilde{I}_{m_1} &= \frac{1}{K} C_1 (edc - eC_3^2 - C_4^2 c - C_2 ed + C_2 C_4^2) \tilde{V}_m \\ \tilde{I}_{m_2} &= \frac{1}{K} a (edc - eC_3^2 - C_4^2 c - C_2 ed + C_2 C_4^2) \tilde{V}_m \\ \tilde{I}_{m_3} &= \frac{-1}{K} (-ed + C_4^2) (-ba + C_1^2 + C_2 a) \tilde{V}_m \\ \tilde{I}_{m_4} &= \frac{1}{K} e C_3 (-ba + C_1^2 + C_2 a) \tilde{V}_m \\ \tilde{I}_{m_5} &= \frac{1}{K} C_4 C_3 (-ba + C_1^2 + C_2 a) \tilde{V}_m \end{aligned} \quad (\text{A.2})$$

where the common denominator  $K$  is given by:

$$K = abcde - cdeC_1^2 - adeC_2^2 - abeC_3^2 \\ - abcC_4^2 + eC_1^2C_3^2 + cC_1^2C_4^2 + aC_2^2C_4^2.$$

## Appendix B

According to (5.8), the equation of 1-dimensional longitudinal wave propagation within a tapered rod with length  $l$  and cross-section  $S_x = S(x)$  is:

$$\tilde{E} \left[ \tilde{u}_x'' + \frac{S_x'}{S_x} \tilde{u}_x' \right] + \rho \omega^2 \tilde{u}_x = 0, \quad (\text{B.1})$$

where  $\rho$  is the density of the material,  $\tilde{E}$  is the complex Young's modulus (5.6),  $\tilde{u}_x = \tilde{u}(x)$  is the complex amplitude (5.5), and  $\omega$  is the frequency of the harmonic vibration. Now, consider an arrangement where one of the bar's ends is free (no strain) and the other end is subjected to a harmonic force  $F(t) = F_0 e^{j\omega t}$ . Therefore, the Neumann boundary conditions are:

$$\tilde{u}_x'|_{x=x_n} = 0, \tilde{E} S_0 \tilde{u}_x'|_{x=x_0} = -F_0. \quad (\text{B.2})$$

Equation (B.1) together with (B.2) determines the governing differential equation of the vibration within a rod.

Without loss of generality, let's assume that the rod has an axisymmetric profile whose  $x$  and  $r$ -components of the profile are functions of a normalized variable, i.e.,  $\zeta$ :

$$\begin{aligned} x &= x(\zeta) \\ r &= r(\zeta), \end{aligned} \quad (\text{B.3})$$

where  $0 \leq \zeta \leq 1$ . A normalized form of (B.3) can be stated as:

$$\begin{aligned} X_\zeta &= X(\zeta) = \frac{x(\zeta) - x_0}{x_n - x_0} \\ R_\zeta &= R(\zeta) = \frac{r(\zeta) - r_n}{r_0 - r_n}, \end{aligned} \quad (\text{B.4})$$

where  $\mathbf{P}_0 = \{x_0, r_0\}$  and  $\mathbf{P}_l = \{x_n, r_n\}$  are the starting point and the ending point of the profile, respectively. Note that in deriving (B.4) it was assumed that the



cross-sectional ratio  $\frac{S_0}{S_n} > 1$  is specified and therefore:

$$\begin{aligned} 0 &= X(0) \leq X(\zeta) \leq X(1) = 1 \\ 1 &= R(0) \geq R(\zeta) \geq R(1) = 0. \end{aligned}$$

In order to describe the vibration in the normalized heterogeneous rod, (B.3) may be rewritten using the substitutions,

$$l = x_n - x_0 = \text{length of the rod} \quad (\text{B.5a})$$

$$\tilde{U}_\zeta = \tilde{U}(\zeta) = \frac{\tilde{u}(x(\zeta))}{l} \quad (\text{B.5b})$$

$$b = \frac{r_n}{r_0 - r_n} \quad (\text{B.5c})$$

$$\lambda = j\omega l \sqrt{\frac{\rho}{\tilde{E}}} = \frac{j\omega l}{c\sqrt{1 + j\psi/2\pi}}, \quad (\text{B.5d})$$

where  $c$  is the wave speed within the waveguide. The procedure is as follows.

Using (B.3), (B.4) and (B.5a),  $x'_\zeta$  and  $x''_\zeta$  can be obtained as:

$$x'_\zeta = \frac{dx}{d\zeta} = l \frac{dX}{d\zeta} = lX'_\zeta \quad (\text{B.6a})$$

$$x''_\zeta = \frac{d^2x}{d\zeta^2} = l \frac{d^2X}{d\zeta^2} = lX''_\zeta. \quad (\text{B.6b})$$

Similarly,  $r'_\zeta$  can be derived as

$$r'_\zeta = \frac{dr}{d\zeta} = (r_0 - r_n) \frac{dR}{d\zeta} = (r_0 - r_n)R'_\zeta. \quad (\text{B.7})$$

For an axisymmetric horn profile, the cross section can be obtained as:

$$S(\zeta) = \pi r_\zeta^2. \quad (\text{B.8})$$

Therefore,

$$S'_\zeta = \frac{dS}{d\zeta} = 2\pi r_\zeta \frac{dr}{d\zeta} = 2\pi r_\zeta r'_\zeta. \quad (\text{B.9})$$

Combining (B.6a), (B.7) and (B.9), one can obtain

$$S'_x = \frac{dS}{dx} = \frac{\frac{dS}{d\zeta}}{\frac{dx}{d\zeta}} = \frac{2\pi r_\zeta r'_\zeta}{x'_\zeta} = \frac{2\pi r_\zeta (r_0 - r_n) R'_\zeta}{l X'_\zeta}. \quad (\text{B.10})$$

Using (B.8), (B.10) and (B.4):

$$\frac{S'_x}{S_x} = \frac{2\pi r_\zeta (r_0 - r_n) R'_\zeta}{\pi r_\zeta^2 l X'_\zeta} = \frac{2(r_0 - r_n)}{r_\zeta l} \frac{R'_\zeta}{X'_\zeta} = \frac{2(r_0 - r_n)}{(r_0 - r_n) R_\zeta + r_n} \frac{1}{l} \frac{R'_\zeta}{X'_\zeta}. \quad (\text{B.11})$$

Substituting (B.5c) into (B.11), the latter can be further simplified as:

$$\frac{S'_x}{S_x} = \frac{2}{R_\zeta + b} \frac{1}{l} \frac{R'_\zeta}{X'_\zeta}. \quad (\text{B.12})$$

(B.5b) can be used to obtain  $\tilde{u}'_x$  and  $\tilde{u}''_x$  in terms of the normalized functions  $\tilde{U}_\zeta$ ,  $\tilde{X}_\zeta$  and  $\tilde{R}_\zeta$  and their derivatives, as follows:

$$\tilde{U}'_\zeta = \frac{d\tilde{U}}{d\zeta} = \frac{1}{l} \frac{d}{d\zeta} \tilde{u}(x(\zeta)) = \frac{1}{l} \frac{d\tilde{u}}{dx} \frac{dx}{d\zeta} = \frac{d\tilde{u}}{dx} \frac{dX}{d\zeta} = \tilde{u}'_x X'_\zeta, \quad (\text{B.13})$$

where (B.6a) has been used to simplify the result. Therefore,

$$\tilde{u}'_x = \frac{\tilde{U}'_\zeta}{X'_\zeta}. \quad (\text{B.14})$$

On the other hand,

$$\begin{aligned} \tilde{U}''_\zeta &= \frac{d}{d\zeta} \left( \frac{d\tilde{u}}{dx} \frac{dX}{d\zeta} \right) = \frac{d}{d\zeta} \left( \frac{d\tilde{u}}{dx} \right) \frac{dX}{d\zeta} + \frac{d\tilde{u}}{dx} \frac{d^2 X}{d\zeta^2} \\ &= \frac{d^2 \tilde{u}}{dx^2} \frac{dx}{d\zeta} \frac{dX}{d\zeta} + \frac{d\tilde{u}}{dx} \frac{d^2 X}{d\zeta^2} = \tilde{u}''_{xx} X'_\zeta + \tilde{u}'_{xx} X''_\zeta, \end{aligned} \quad (\text{B.15})$$

where “Chain rule” has been used to find  $\frac{d}{d\zeta} \left( \frac{d\tilde{u}}{dx} \right)$ . Using (B.6a) and (B.14), (B.15)

can be further simplified as:

$$\tilde{U}_\zeta'' = \tilde{u}_x''(lX'_\zeta)X'_\zeta + \frac{\tilde{U}_\zeta'}{X'_\zeta}X''_\zeta = l\tilde{u}_x''(X'_\zeta)^2 + \frac{X''_\zeta}{X'_\zeta}\tilde{U}_\zeta'. \quad (\text{B.16})$$

Therefore,

$$\tilde{u}_x'' = \frac{\tilde{U}_\zeta'' - \frac{X''_\zeta}{X'_\zeta}\tilde{U}_\zeta'}{l(X'_\zeta)^2}. \quad (\text{B.17})$$

Finally by substituting (B.5b), (B.12), (B.14) and (B.17) in the vibration equation (B.1), it can be restated in the non-dimensional space as:

$$\tilde{u}_x'' + \frac{S'_x}{S_x}\tilde{u}_x' + \frac{\rho\omega^2}{\tilde{E}}\tilde{u}_x = \frac{\tilde{U}_\zeta'' - \frac{X''_\zeta}{X'_\zeta}\tilde{U}_\zeta'}{l(X'_\zeta)^2} + \frac{2}{R_\zeta + b} \frac{1}{l} \frac{R'_\zeta}{X'_\zeta} \frac{\tilde{U}_\zeta'}{X'_\zeta} + \frac{\rho\omega^2}{\tilde{E}}l\tilde{U}_\zeta = 0. \quad (\text{B.18})$$

Assuming that  $X'_\zeta$  is non-zero for all  $0 \leq \zeta \leq 1$ , the 1-dimensional vibration equation within an axisymmetric horn profile can then be reformulated in the non-dimensional space as:

$$\tilde{U}_\zeta'' + \tilde{U}_\zeta' \left( \frac{2R'_\zeta}{R_\zeta + b} - \frac{X''_\zeta}{X'_\zeta} \right) - \lambda^2(X'_\zeta)^2\tilde{U}_\zeta = 0, \quad (\text{B.19})$$

where  $\lambda$  is defined in (B.5d).

The boundary conditions can also be reformulated in the non-dimensional space by substituting (B.14) in (B.2), as:

$$\begin{aligned} \tilde{u}_x'|_{x=x_n} &= \frac{\tilde{U}_\zeta'}{X'_\zeta}|_{\zeta=1} = 0 \\ \tilde{E}S_0\tilde{u}_x'|_{x=x_0} &= \tilde{E}S_0\frac{\tilde{U}_\zeta'}{X'_\zeta}|_{\zeta=0} = -F_0. \end{aligned} \quad (\text{B.20})$$

Once again, assuming that  $X'_\zeta$  is non-zero, the boundary conditions for the normalized

vibration equation will be:

$$\begin{aligned}\tilde{U}'_{\zeta}|_{\zeta=1} &= 0 \\ \tilde{U}'_{\zeta}|_{\zeta=0} &= -\frac{F_0}{\tilde{E}S_0}X'_{\zeta}|_{\zeta=0} = -\tilde{\varepsilon}_0 X'_{\zeta}|_{\zeta=0},\end{aligned}\tag{B.21}$$

where  $\tilde{\varepsilon}_0 = \tilde{\varepsilon}(0)$  is the complex strain caused by  $F_0$  at the input.

# Curriculum Vitae

## Iman Khalaji

---

### Education

- |  |                     |
|--|---------------------|
| <b>Ph.D. in Mechanical Engineering</b><br><i>University of Western Ontario, London, Ontario, Canada</i>  | Jan 2010–Dec 2014   |
| <b>M.Sc. in Mechanical Engineering</b><br><i>Iran University of Science and Technology, Tehran, Iran</i> | Sept 2003–Jan 2006  |
| <b>B.Sc. in Mechanical Engineering</b><br><i>Isfahan University of Technology, Isfahan, Iran</i>         | Sept 1999–Sept 2003 |

### Experience

- |  |           |
|--|-----------|
| <b>Research Associate Engineer (PhD candidate)</b><br><i>Canadian Surgical Technologies and Advanced Robotics (CSTAR),<br/>London, Ontario, Canada</i>   | 2010–2014 |
| <ul style="list-style-type: none"><li>• Designed and developed a robotics–assisted articulating ultrasonic surgical scalpel.</li><li>• Designed, developed and experimentally validated a high-frequency vibration–assisted surgical needle insertion device.</li><li>• Designed, developed and implemented a semi-autonomous robotic platform to compensate for undesirable modulated motion of soft tissue during needle insertion in the lung.</li><li>• Designed a new robotics-assisted surgical grasping instrument with disposable palpation sensor for the purpose of determining soft tissue properties via telerobotic tissue palpation.</li><li>• Conducted thorough finite element analyses (including kinematics, dynamics and stress analysis) for conceptual designs of two small-scale medical robots.</li></ul> |           |
| <b>Research Assistant Engineer</b><br><i>Electrical and Computer Engineering Dept., University of Western Ontario, London, Ontario, Canada</i>   | 2007–2009 |
| <ul style="list-style-type: none"><li>• Developed and validated a real-time finite element model (statistical finite element model or SFEM) for soft tissue deformation.</li><li>• Implemented a real-time elastography (strain imaging) technique for prostate cancer diagnosis.</li></ul>  |           |

**Research Assistant** 2003–2006  
*Fatigue and Fracture Lab, Iran University of Science and Technology, Tehran, Iran*

- Implemented a low-cycle fatigue model to predict the fatigue life of various metallic materials under multi-axial loading.

**Instructor and Graduate Teaching Assistant** 2007–2013  
*Faculty of Engineering, University of Western Ontario, London, Ontario, Canada*

## **Skills**

- Robotics and mechanism design
- Structural, vibrational, electromechanical, and finite element analysis
- Computer aided design and manufacturing (e.g., SolidWorks, AC CAM easy)
- Hands-on experience with various manufacturing processes such as milling, lathe, wire EDM, high-speed EDM turning, rapid prototyping, metal laser sintering, as well as assembly of small components
- MATLAB/Simulink programming, object-oriented programming (Python, C++), API-based programming (SolidWorks API, ABAQUS scripting)

## **Honors and Awards**

- Nominated for Graduate Student Teaching Award 2012–2013
- Graduate Thesis Research Award, UWO (\$1500) 2012–2013
- Ontario Graduate Scholarship (OGS) (\$15,000 per annum) 2012–2013
- Queen Elizabeth II Graduate Scholarship in Science and Technology (QEII-GSST) (\$15,000 per annum) 2011–2012
- NSERC CREATE program in Computer-Assisted Medical Interventions (CAMI), University of Western Ontario (\$10,500 per annum) 2010–2012
- Graduate Thesis Research Award, University of Western Ontario (\$754) 2008–2009
- Best Presentation Award in Graduate Symposium, Electrical and Computer Engineering Dept., University of Western Ontario (\$150) 2008–2009
- NIH/NIBIB EMBC08 Conference Support Award (\$250 USD) 2008–2009

## Publications and Contributions

### ***Peer-Reviewed Journal Papers: Published/Accepted/In Press/Submitted***

1. S.R. Mousavi , **I. Khalaji**, A. Sadeghi Naini, K. Raahemifar, A. Samani, “Statistical finite element method for real-time tissue mechanics analysis”, *Computer Methods in Biomechanics and Biomedical Engineering*, Vol. 15, No. 6, pp. 595–608, 2012.
2. H. Jahed, A. Varvani-Farahani, M. Noban, **I. Khalaji**, “An energy-based fatigue life assessment model for various metallic materials under proportional and non-proportional loading conditions”, *International Journal of Fatigue*, Vol. 29, No. 4, pp. 647–655, 2007.

### ***Peer-Reviewed Papers in Conference Proceedings***

3. **I. Khalaji**, M.D. Naish, R.V. Patel, “Articulating minimally invasive ultrasonic tool for robotics–assisted surgery”, Submitted to *IEEE International Conference on Robotics and Automation (ICRA)*, 2015.
4. **I. Khalaji**, M. Hadavand, A. Asadian, R.V. Patel, and M.D. Naish. “Analysis of needle-tissue friction during vibration–assisted needle insertion”, In *IEEE/RSJ International Conference on Intelligent Robots and Systems (IROS)*, pp. 4099–4104, 2013.
5. S.F. Atashzar\*, **I. Khalaji\***, M. Shahbazi\*, A. Talasaz, R.V. Patel, and M.D. Naish. “Robot-assisted lung motion compensation during needle insertion”, In *IEEE International Conference on Robotics and Automation (ICRA)*, pp. 1682–1687, 2013. (\* Equal contribution among the first three authors).
6. **I. Khalaji**, R.V. Patel, M.D. Naish, “Systematic design of an ultrasonic horn profile for high displacement amplification”, In *4th IEEE RAS & EMBS International Conference (BioRob)*, pp. 913–918, 2012.
7. **I. Khalaji**, K. Rahemifar, A. Samani, “Accelerated statistical shape model-based technique for tissue deformation estimation”, *Progress in Biomedical Optics and Imaging – Proceedings of SPIE*. 7261, Article number 72610U, 2009.
8. **I. Khalaji**, K. Rahemifar, A. Samani, (2009) “Statistical finite element analysis”, *30th Annual International Conference of the IEEE Engineering in Medicine and Biology Society (EMBS)*, Article number 4650478, pp. 5577–5580, 2008.
9. H. Jahed, A. Varvani-Farahani, M. Noban, **I. Khalaji**, “An energy-based fatigue life model for proportional and non-proportional loading conditions”, *9th International Fatigue Conference*, Atlanta, Georgia, USA, 2006.

10. **I. Khalaji**, H. Jahed, A. Varvani-Farahani, M. Noban, “Out-of-phase loading life prediction using energy-fatigue life relation”, *14th Annual (International) Mechanical Engineering Conference*, Isfahan, Iran, 2006.

#### ***Peer-Reviewed Abstracts***

11. **I. Khalaji**, K. Rahemifar, A. Samani, “Elastic modulus reconstruction using a novel fast finite element model,” *7th International Conference on the Ultrasonic Measurement and Imaging of Tissue Elasticity*, Austin, Texas, USA, p. 102, 2008.

#### ***Poster Presentations***

12. **I. Khalaji**, R.V. Patel, M.D. Naish, “Towards miniaturization of ultrasonically activated scalpels”, London Health Research Day, London, Ontario, Canada, March 2012.
13. **I. Khalaji**, A. Samani, “Real-time prostate deformable model - preliminary application in prostate ultrasound elastography for tumour detection”, CIHR Team Grant and OICR Imaging Pipeline Platform / One millimeter Cancer Challenge Workshop, Imaging Applications in Prostate Cancer, London, Ontario, November 2009.
14. **I. Khalaji**, H. Karimi, A. Samani, “Tissue elasticity imaging using accelerated finite element technique”, WORLDdiscoveries Research Showcase, University of Western Ontario, London, Ontario, January 2009.